FRESNEL LENS SOLAR COLLECTOR DEVELOPMENT CONSIDERING LOCAL CONDITIONS

A THESIS SUBMITTED TO
THE GRADUATE SCHOOL OF NATURAL AND APPLIED SCIENCES
OF
MIDDLE EAST TECHNICAL UNIVERSITY

BY

DENİZ DEĞİRMENCİ

IN PARTIAL FULFILLMENT OF THE REQUIREMENTS
FOR
THE DEGREE OF MASTER OF SCIENCE
IN
MECHANICAL ENGINEERING

SEPTEMBER 2022

Approval of the thesis:

FRESNEL LENS SOLAR COLLECTOR DEVELOPMENT CONSIDERING LOCAL CONDITIONS

submitted by **DENİZ DEĞİRMENCİ** in partial fulfillment of the requirements for the degree of **Master of Science in Mechanical Engineering Department, Middle East Technical University** by,

Prof. Dr. Halil Kalıpçılar
Dean, Graduate School of **Natural and Applied Sciences** _____

Prof. Dr. M. A. Sahir Arıkan
Head of Department, **Mechanical Engineering** _____

Prof. Dr. İlker Tarı
Supervisor, **Mechanical Engineering, METU** _____

Examining Committee Members:

Assoc. Prof. Dr. Özgür Bayer
Mechanical Engineering, METU _____

Prof. Dr. İlker Tarı
Mechanical Engineering, METU _____

Prof. Dr. Derek K. Baker
Mechanical Engineering, METU _____

Assist. Prof. Dr. Özgür Selimoğlu
Energy Engineering, Ankara University _____

Assist. Prof. Dr. Mehdi Mehrtash
Energy Systems Engineering, Atılım University _____

Date: 02.09.2022

I hereby declare that all information in this document has been obtained and presented in accordance with academic rules and ethical conduct. I also declare that, as required by these rules and conduct, I have fully cited and referenced all material and results that are not original to this work.

Name, Surname: DENİZ DEĞİRMENCİ

Signature :

ABSTRACT

FRESNEL LENS SOLAR COLLECTOR DEVELOPMENT CONSIDERING LOCAL CONDITIONS

DENİZ DEĞİRMENCİ,
M.S., Department of Mechanical Engineering
Supervisor: Prof. Dr. İlker Tarı

September 2022, 83 pages

In this thesis, the development of Fresnel lens solar collectors is investigated considering local conditions. The Fresnel lens solar collector focuses the sun's rays on a receiver located at the focal line using the principle of refraction. This collector system can reach relatively high temperatures that can be used in industrial processes. To analyze the lens, a ray tracing code and an auxiliary lens design code has been developed that work with a wavelength-dependent spectrum and takes the refraction, reflection, absorption, and extinction coefficients of transparent materials into account. For obtaining the efficiency of the designed collector, the heat loss from the system, and the time-dependent variation of the operating temperatures reached during the day, a thermal model of the collector receiver and an annual performance model, which uses the actual TMY data, were developed. Combining these two models, operating temperature values obtained during the day and collector performance data are obtained and presented.

Keywords: Fresnel lens solar collector, Solar heat for industrial processes, Ray tracing, Heat flux distribution

ÖZ

YEREL KOŞULLARI GÖZ ÖNÜNDE BULUNDURARAK FRESNEL LENS GÜNEŞ KOLEKTÖRÜ GELİŞTİRME

DENİZ DEĞİRMENCİ,
Yüksek Lisans, Makina Mühendisliği Bölümü
Tez Yöneticisi: Prof. Dr. İlker Tarı

Eylül 2022 , 83 sayfa

Bu tezde, yerel koşullar göz önünde bulundurularak Fresnel lens güneş kolektörlerinin geliştirilmesi incelenmiştir. Fresnel lens güneş kolektörü, güneşten gelen ışınları kırılma prensibini kullanarak odak hattında bulunan bir alıcıya odaklamaktadır. Bu kolektör sistemi, endüstriyel işlemlerde kullanılabilecek göreceli olarak yüksek sıcaklıklara ulaşabilmektedir. Lensin incelenmesi için, dalga boyuna bağlı spektrumla çalışan ve ışığın kırılmasını, yansımasını ve soğurulmasını, saydam maddelerin sönüm katsayılarını ve dalga boyuna bağlı kırılma endekslerini dikkate alan bir ışın izleme kodu ve yardımcı bir lens tasarım kodu geliştirilmiştir. Tasarlanan kolektörün verimini, sistemden ısı kaybını ve gün içinde ulaşılan çalışma sıcaklıklarının zamana bağlı değişimini elde etmek için kolektör alıcısının termal modeli ve gerçek TMY verilerini kullanan yıllık performans modeli oluşturulmuştur. Bu iki model birleştirilerek, gün içinde elde edilen sıcaklık değerleri ve kolektör performans verileri elde edilmiştir ve sunulmuştur.

Anahtar Kelimeler: Fresnel lens güneş kolektörü, Endüstriyel işlemler için güneş enerjisi, Işın izleme, Isı akısı dağılımı

To my family and my beloved girlfriend

ACKNOWLEDGMENTS

I would like to express my sincere gratitude to Prof. Dr. İlker Tarı for his guidance, continuous support, and opportunities he offered throughout my study.

I would like to thank my colleague, but before that, my friend, Ertuğrul Çubuk, for his encouragement and friendship.

I would like to thank Mustafa Yalçın for his ideas, knowledge, and continuous help in the laboratory.

And I would like to thank my family and my girlfriend, Ece Kurnaz, for their support and encouragement throughout my study, also for helping me during my injury.

TABLE OF CONTENTS

LIST OF TABLES

TABLES

LIST OF FIGURES

FIGURES

NOMENCLATURE

ABBREVIATIONS

AM1.5	Air Mass 1.5
CAD	Computer-aided design
CAPEX	Capital expenditure
CCD	Charged-coupled device
CIEMAT	Centro de Investigaciones Energéticas, Medioambientales y Tecnológicas
CPVT	Concentrated photovoltaic thermal
CSP	Concentrated solar power
CST	Concentrated solar thermal
DNI	Direct normal irradiance
GHI	Global horizontal irradiance
GUI	Graphical user interface
HTF	Heat transfer fluid
IEA	International Energy Agency
IRENA	International Renewable Energy Agency
LCOE	Levelized cost of electricity
MENA	Middle East and North Africa
OPEX	Operational expenditure
PMMA	Polymethyl methacrylate
PV	Photovoltaics
SHIP	Solar heat for industrial processes

LIST OF SYMBOLS

α	Angle between the plane normal vector and the direction vector of the ray, rad.
α_{ge_o-a}	Thermal diffusivity of the air evaluated at the average temperature, m^2/s.
α_θ	Absorbtance at an angle.
α_n	Absorbtance at direct intersection.
β	Angle between the plane normal vector and the vector, from an arbitrary point on the plane to the starting point of the ray, rad.
β_s	Surface tilt angle, rad.
ΔT_{rt-f}	Temperature difference between the receiver tube and the heat transfer fluid, K.
δ	Declination angle, rad.
ϵ	Energy of a photon J.
ϵ_{ge_i}	Emissivity of the inside of the glass envelope.
ϵ_{ge_o}	Emissivity of the outside of the glass envelope.
ϵ_{rt_o}	Emissivity of the receiver tube.
η_{int}	Intersection efficiency.
$\overline{\eta_{int}}$	Mean intersection efficiency.
η_{opt}	Optical efficiency.
$\eta_{opt,0}$	Optical efficiency at zero-degree incidence angle.
$\overline{\eta_{opt}}$	Mean optical efficiency.
γ	Surface azimuth angle, rad.
γ_S	Solar azimuth angle, rad.
λ	Wavelength in dielectric medium, nm.
λ_0	Wavelength in free space, nm.
μ_f	Dynamic viscosity of the heat transfer fluid, Ns/m^2.
ν_{air}	Kinematic viscosity of the air evaluated at the ambient air temperature, m/s^2.
ν_{ge_o-a}	Kinematic viscosity of the air evaluated at the average temperature, m/s^2.

ω	Local standard meridian, $rad.$
ϕ_{rec}	Tangential angle of the receiver, $rad.$
ρ	Reflectance.
$\rho_{\parallel}$	Parallel component of the pellet reflectance.
$\rho_{\perp}$	Perpendicular component of the pellet reflectance.
σ	Stefan-Boltzmann constant, $W/(m^2K^4)$.
$\sigma_{\eta_{int}}$	Standard deviation of the intersection efficiencies.
$\sigma_{\eta_{opt}}$	Standard deviation of the optical efficiencies.
τ	Transmittance.
θ	Incidence angle, $rad.$
θ_s	Surface incidence angle, $rad.$
θ_z	Solar zenith angle, $rad.$
A_{rt-f}	Inner surface area of the receiver tube, m^2.
c	Speed of light in dielectric medium, m/s.
c_0	Speed of light in free space, m/s.
$C_{p_{oil}}$	Specific heat of the oil. $Jkg^{-1}K^{-1}$
D_{ge_i}	Inner diameter of the glass envelope, m.
D_{ge_o}	Outer diameter of the glass envelope, m.
d_{lens}	Thickness of the lens, m.
D_{rt_i}	Inner diameter of the receiver tube, m.
D_{rt_o}	Outer diameter of the receiver tube, m.
E	Equation of time, hr.
$E_{abs,\ rec}$	Percent of the energy absorbed by the receiver.
$E_{abs,\ tra}$	Percent of the energy absorbed by the transparent mediums.
E_{lost}	Percent of the energy lost to the environment.
f	Fanning friction factor.
f_{lens}	Focal length of the lens, m.
$f_{objective}$	Objective function for root finding, K.
G_{beam}	Solar irradiation, W/m^2.
g	Gravitational constant, m/s^2.

h	Planck's constant, m^2kg/s.
h_f	Convective heat transfer coefficient between the receiver tube and the heat transfer fluid, $W/(m^2K)$.
h_{ge_o-a}	Convective heat transfer coefficient between the glass envelope and the ambient air, $W/(m^2K)$.
I_b	Beam irradiation, W/m^2.
K	Incidence angle modifier.
k	Extinction coefficient, m^{-1}.
k_{air}	Thermal conductivity of the ambient air, $W/(mK)$.
k_f	Thermal conductivity of the heat transfer fluid, $W/(mK)$.
k_{ge}	Thermal conductivity of the glass envelope, $W/(mK)$.
k_{rt}	Thermal conductivity of the receiver tube, $W/(mK)$.
m_{oil}	Mass of the oil. kg
$\dot{m}_{oil}$	Mass flow rate of the oil. kg/s
LCR	Local concentration ratio.
$\dot{m}_f$	Mass flow rate for the heat transfer fluid, kg/s.
n	Refractive index.
$\mathrm{N}_{\text{abs, rec}}$	Percent of the rays absorbed by the receiver.
$\mathrm{N}_{\text{abs, tra}}$	Percent of the rays absorbed by the transparent mediums.
n_{day}	Day number.
n_{lens}	Refractive index of the lens material.
N_{loop}	Number of loops per hour.
N_{lost}	Percent of the rays lost to the environment.
NN	Number of rays emitted from the source plane.
$\overrightarrow{N_{plane}}$	Plane normal vector.
N_{ray}	Sample size.
$N_{repetition}$	Number of repetitions.
$\overrightarrow{N_{surf}}$	Surface normal vector.
$\overline{Nu}_D$	Nusselt number for cross flow over a cylindrical surface between the glass envelope and the ambient air.

$Nu_{D_{ge_o}}$	Nusselt number for free convection between the glass envelope and the ambient air.
$Nu_{D_{rt_i}}$	Nusselt number for internal flow.
$Nu_{laminar,D_{rt_i}}$	Nusselt number for laminar internal flow.
$Nu_{turbulent,D_{rt_i}}$	Nusselt number for turbulent internal flow.
P_h	Intersection point on the plane.
P_p	Arbitrary point on the plane.
$\overrightarrow{P_pP_s}$	Vector from a arbitrary point on the plane to the starting point of the direction vector of the ray.
Pr_{air}	Prandtl number of the air evaluated at the ambient air temperature.
Pr_f	Prandtl number of the heat transfer fluid.
Pr_{ge_o-a}	Prandtl number of the air evaluated at the average temperature.
Pr_s	Prandtl number of the air evaluated at the surface temperature.
$\overrightarrow{P_v}$	Vector from the origin to a vertex.
$q_{absorbed,ge}$	Absorbed solar irradiation by the glass envelope, W.
$q_{absorbed,rt}$	Absorbed solar irradiation by the receiver tube, W.
q_{cond,ge_i-ge_o}	Conductive heat transfer within the glass envelope, W.
q_{cond,rt_i-rt_o}	Conductive heat transfer within the receiver tube, W.
$q_{conv,f-rt_i}$	Convective heat transfer between the receiver tube and the heat transfer fluid, W.
q_{conv,ge_o-a}	Convective heat transfer between the glass envelope and the ambient air, W.
q_{conv,rt_o-ge_i}	Convective heat transfer between the receiver tube and the glass envelope, W.
q_{local}	Local heat flux, W.
q_{loss}	Receiver heat loss, W.
q_{rad,ge_o-s}	Radiative heat transfer between the glass envelope and the sky, W.
q_{rad,rt_o-ge_i}	Radiative heat transfer between the receiver tube and the glass envelope, W.

R_1	Radius of the first curvature of the lens, m.
R_2	Radius of the second curvature of the lens, m.
$Ra_{D_{ge_o}}$	Rayleigh number between the glass envelope and the ambient air.
Re_D	Reynold's number for cross flow over a cylindrical surface.
$Re_{D_{rt_i}}$	Reynold's number for internal flow.
r_{ref}	Radius of the reflective surface, m.
S_{dp}	Dot product of the plane normal vector and the direction vector of the ray.
T_a	Ambient air temperature, K.
T_f	Bulk temperature of the heat transfer fluid, K.
T_{ge_i}	Inner temperature of the glass envelope, K.
T_{ge_o}	Outer temperature of the glass envelope, K.
T_{inlet}	Inlet temperature of the working fluid, K.
T_{outlet}	Outlet temperature of the working fluid, K.
T_{rt_i}	Inner temperature of the receiver tube, K.
T_{rt_o}	Outer temperature of the receiver tube, K.
T_s	Surface temperature, K.
$t_{solarmidhour}$	Local middle of the hour in solar time, hr.
$t_{standard}$	Local time, hr.
$\overrightarrow{V_{cp}}$	Vector obtained from the cross product of the edge vector and the surface normal vector.
$\overrightarrow{V_e}$	Edge vector of the element.
$\overrightarrow{V_h}$	Vectors from the element vertices to the intersection point.
$\overrightarrow{V_{ray}}$	Direction vector of the ray.
V_{wind}	Wind velocity, m/s.
y_{shift}	Center shift of the reflective surface, m.

CHAPTER 1

INTRODUCTION

1.1 Motivation and Problem Definition

Global CO_2 and greenhouse gas emissions have increased exponentially in the current century due to the increasing energy consumption from population increase and technological development [1]. This increase resulted in a human-induced issue known as climate change. For reaching the peak of these gas emissions throughout the sectors and limit the increase in the global average temperature to 2 °C above pre-industrial levels, a universal response named *"The Paris Agreement"* is adopted [2]. The United Nations [3] reports that 192 countries and the European Union have joined this agreement.

The potential of solar energy, which can be used for generating electricity, heating homes and water, and power transportation, as a means of reducing reliance on fossil fuels and mitigating climate change is being discussed. While the upfront cost of solar energy technologies can be prohibitive, the long-term costs are much lower than those of fossil fuels making solar energy an attractive option for reducing emissions.

In the context of electricity generation, two technologies arise at the top. The first is photovoltaics (PV), which converts solar energy, in terms of global horizontal irradiance (GHI), into electricity at the atomic level [4], and if storage is concerned, it would require a battery system. Later one is the concentrated solar power (CSP) system which collects the solar energy, in terms of direct normal irradiance (DNI), through absorbers and transfers it to a working medium such as heat transfer oils, molten salt, and granular particles to be used in a power block or stored in a storage tank. Comparing two solar electricity systems, Fraunhofer [5] reports that PV

systems without battery systems have a levelized cost of electricity (LCOE) below 2.5Ccent/kWh, while CSP power plants with integrated thermal storage at full load hours up to 3600 hours are below 6 Ccent/kWh at locations with high solar resources, to be precise, DNI of 2000 kWh/(m^2a). However, as Gurung A. and Qiao Q. [6] state, integrated PV-battery systems, which are in the early stages of research and development, have three technical challenges, energy density, efficiency, and stability. Due to these challenges concerning the integrated PV-battery systems, CSP systems are the sensible choice for supplying electricity to the demand during night hours due to their simplicity and cost-effectiveness of energy storage solutions.

Countries that are rich in terms of solar resources, like countries in the Middle East-/North Africa (MENA) region, use this resource in their favor by investing in solar technologies and setting a roadmap to increase their renewable capacity to double in 5 years, from 15 GW in 2021 to 32 GW in 2026, according to International Energy Agency (IEA) [7].

Especially in light of the Russian invasion of Ukraine, the European Commission renewed its effort under *A European Green Deal* and is taking action to save energy, produce clean energy, and diversify energy supplies [8].

Another application area of the solar energy systems is heating, and as illustrated in Figure 1.1 prepared through Solar Payback Project [9] using several data sources, global heat demand can be branched as 32% for industrial, 31% for transport, 24% for residential, and 13% for other areas.

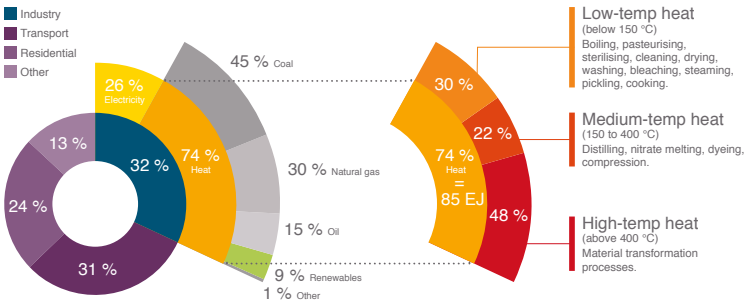

Figure 1.1: Global heat demand in the industry; total, final energy consumption, 2014, by Solar Payback Project [9].

Therefore, low-temperature heating applications which are below 150 °C have an as big impact as medium-temperature and high-temperature heating applications, considering residential usage in addition to industrial.

In Figure 1.2, the share of solar thermal heat consumption in total final energy consumption for selected countries, which are members of IEA, are given. Comparing the countries which are located at similar latitudes and have similar solar insolation, i.e., Greece, China, Turkey, Portugal, Spain, and Uzbekistan, the maturity and the acceptance of the solar technologies used in the heating applications in these countries can be deduced.

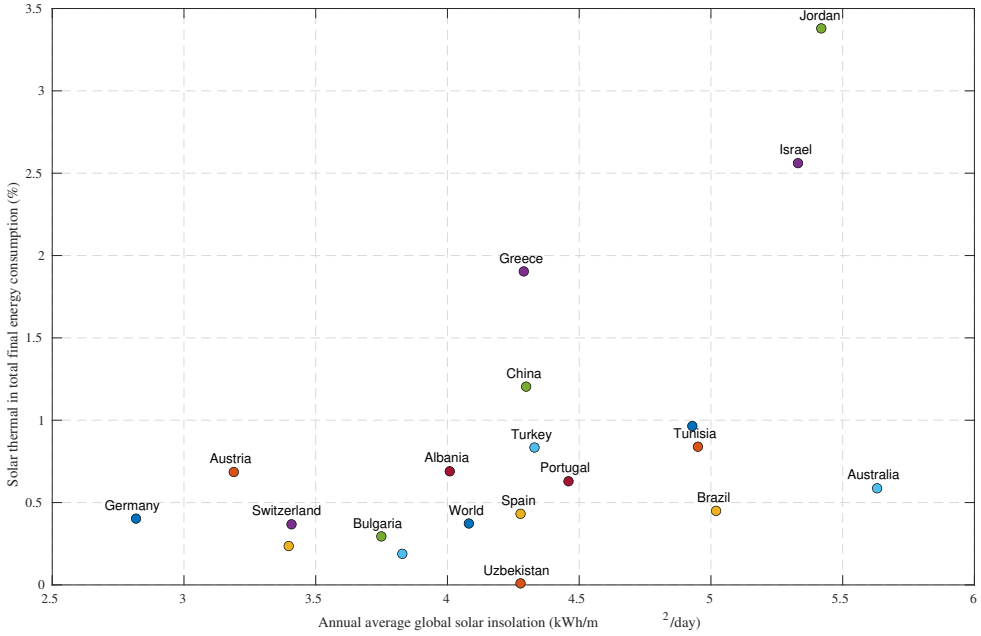

Figure 1.2: Share of solar thermal heat consumption in total final energy consumption, in selected countries and regions, 2019, by IEA [10].

As the largest energy end-use, heat accounts for half of global final energy consumption, and about 50% of the heat consumed in 2020 is consumed by industrial processes, and another 47% is consumed in buildings, according to IEA [11]. Utilizing the potential of solar thermal for a wide range of applications, both for domestic and industrial use would result in a significant decrease in emissions. Turkey Energy Outlook 2020 by Difiglio et al. [12] indicates the share of heat demands of the low-temperature and medium-temperature industrial processes by sectors, such as, in

2018, textile with 9%, food with 8%, and paper and non-ferrous manufacturing with each 2%, accounting for 21% in total, while sectors like iron-steel, cement, chemicals and petrochemicals, ceramics, and glass production, where high temperatures are needed, consume 61% in total.

As illustrated in Figure 1.3, 2019 data from IEA [13] shows that only shy of 11% of global heat consumption is supplied from renewable sources. Moreover, solar thermal accounts for 0.7% of the global heat supply, which corresponds to 6.4% of the renewable sources.

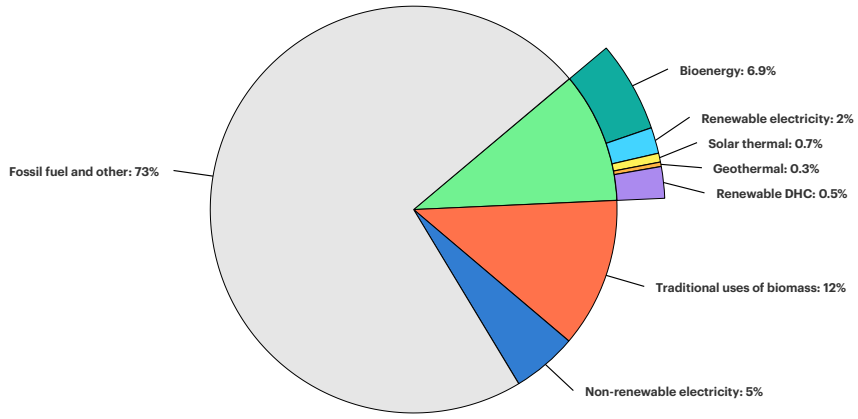

Figure 1.3: Share of renewable sources in global heat consumption, 2019, IEA [13].

To increase the share of the solar thermal, the reasons for not being selected as a viable option and the challenges in the deployment of these systems should be emphasized. To this end, perusing the current research and the research plans for the future are important. During a presentation in 2019, at the ODAK$_{TR}$ Seminar Series, Zarza E. from CIEMAT [14], stated that a significant research and development effort related to concentrated solar thermal (CST) systems is devoted to the following items.

- Cost (capital expenditure (CAPEX), operational expenditure (OPEX)) reduction,
- Efficiency increase,
- Better dispatchability,
- Better environmental sustainability.

Likewise, the European Commission's Strategic Energy Technology Plan progress report for 2021 [15] indicates that half of the key projects on CST focus on reducing the costs both for installation and maintenance.

As illustrated in the publication highlighting the renewable power generation costs in 2020, published by International Renewable Energy Agency (IRENA) [16], which compares the concentrating solar power plants' capacity, storage hours, and total installation costs, it can be concluded that the installation costs of the concentrating solar technologies are in a decline. For instance, in the same publication, a CSP plant with a parabolic trough collector field at a capacity of around 100 MW, and 0-4 hours of thermal storage costs around 9000 $/kW in 2015, while a similar-capacity CSP plant with a parabolic trough collector field with 8-10 hours of thermal storage in 2020 costs around half of the previous one.

Although the price of technologies has a decreasing trend due to the increasing number of technological advancements, their initial costs are still considered to be high. Furthermore, Kurup P. and Turchi C. [17] share their findings about the final costs of installation per meter squared of the widely used parabolic trough collectors for plant-scale installations which are 178$ for *Ultimate Trough* and 170$ for *SkyTrough*. These findings will be discussed in Section 1.4 in detail, however, to briefly mention, a significant portion of the cost of the parabolic trough collector systems is due to the support structures which hold these heavy collectors and rotate with them.

For residential use and most industrial applications that could utilize solar heat, these initial costs could be cumbersome. Besides, land needed for the systems such as central receiver system, parabolic trough collector, and linear-Fresnel collector may not be available. Low-cost and versatile systems can address these issues. The aim of this thesis is to explore a refraction-based concentrator system as the manufacturing costs of the lenses decrease and there is a motivation for the use of solar heat integration industrial processes, and to develop a collector system that addresses the sectors accounting for 21% of the industrial heat demand of Turkey, indicated in Turkey Energy Outlook 2020 by Difiglio et al. [12].

1.2 Concentrated Solar Thermal & Power Systems

The concentrated solar systems use mirrors and lenses to focus rays coming from the Sun to receiver surfaces to increase the temperature of the working medium to provide heat to processes and power cycles. In these applications, one of the main advantages of concentrating systems is that they can be coupled with integrated energy storage technologies to prolong the operation hours of these systems.

These concentrating solar thermal systems can be categorized into two, point-focus and line-focus concentrating systems. The point-focus concentrating systems can achieve higher concentration ratios compared to the line-focus concentrating systems due to the ratio of the collector aperture area to the receiver area. As explained in Duffie J. and Beckman W. [18], the maximum theoretical concentration ratio for a three-dimensional concentrator such as a paraboloid can be as high as 45000, while it is limited to 212 for a two-dimensional concentrator such as a cylindrical parabolic concentrator.

1.2.1 Point-Focus Concentrating Systems

Two common systems of the point-focus concentrating systems are given in Figure 1.4, the central receiver and the parabolic dish.

(a) (b)

Figure 1.4: Schematics of the point-focus concentrating systems, *(a) central receiver, (b) parabolic dish.*

1.2.1.1 Central Receiver

In central receiver systems, a field of mirrors tracks the Sun on two axes, independent of each other, to focus its rays on a receiver, mostly on a tower. The concentration ratio of the central receiver systems can be between 300 and 1500, resulting in indicative temperatures between 150 and 2000 °C, according to Kalogirou S. [19]. Besides, at high concentration ratios, system temperatures up to 1000 °C can be achieved according to Luzzi A. and Lovegrove K. [20]. Furthermore, as system temperature increases, the thermodynamic cycle efficiency also increases. Although the central receiver has a lower levelized cost of electricity due to higher cycle efficiency, the installation cost of this system is higher compared to the other collector systems.

Figure 1.5: Crescent Dunes central receiver system solar power plant, Worland J. and Raab J. [21].

1.2.1.2 Parabolic Dish

In parabolic dish systems, the mirrors are placed in a paraboloid structure, which tracks the Sun on two axes, to focus the rays on its receiver. The concentration ratio of the parabolic dish systems can be between 600 and 2000, resulting in indicative temperatures between 100 and 1500 °C, according to Kalogirou S. [19].

Figure 1.6: Maricopa solar power dish plant, EERE [22].

1.2.2 Line-Focus Concentrating Systems

The line-focus systems have lower initial and maintenance costs compared to the point-focus systems. However, their concentration ratios are also lower in comparison. The lower concentration ratios result in lower temperatures, starting from 150 °C to temperatures around 400-600 °C depending on the heat transfer fluid and the concentration ratio according to Breeze P. [23]. Known examples of these systems are parabolic trough collectors and linear-Fresnel collectors which use mirrors to focus the rays on the linear receivers. Due to lower temperatures and their cycle efficiencies of them in comparison, the line-focusing systems would have a higher levelized cost of electricity than the point-focus systems, as indicated by Dieckmann et al. [24].

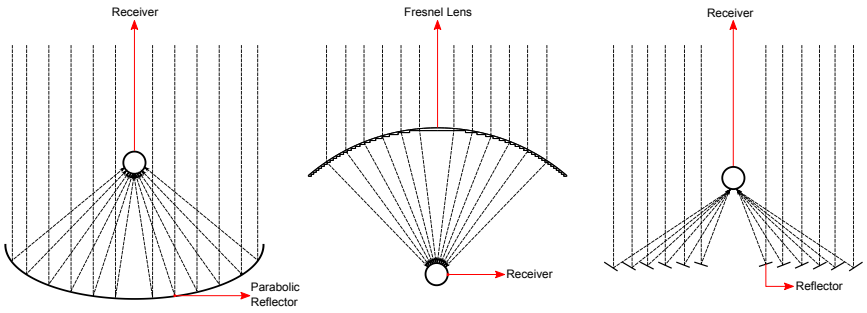

Figure 1.7: Schematics of the line-focus concentrating systems, *(a) parabolic trough collector, (b) Fresnel lens collector, (c) linear Fresnel collector.*

1.2.2.1 Parabolic Trough Collector

The parabolic trough collector systems consist of a cylindrical parabolic mirror with a receiver located at its focus, apart from the structural components. Due to its shape, the mirror and the receiver track the Sun on one axis, which creates complications regarding joints connecting the receiver to the rest of the collector system. In comparison with the point-focus systems, the concentration ratio of the parabolic trough collector systems is lower, resulting in a lower temperature range. The concentration ratio of the parabolic trough collector systems can be between 10 and 85, resulting in indicative temperatures between 60 and 400 °C, according to Kalogirou S. [19].

Figure 1.8: Parabolic trough collector field at the Ouarzazate Solar Power Station Project – Phase I, also known as Noor I [25].

1.2.2.2 Linear-Fresnel Collector

The linear-Fresnel collector system utilizes strips mirrors to track the Sun on one axis and to focus rays coming from the Sun to a stationary receiver. These strips of mirrors are individually adjusted for achieving the focus. In comparison with the parabolic trough collector system, the concentration ratio of the linear-Fresnel collector system is lower, resulting in a lower operating temperature range. The concentration ratio of the linear-Fresnel collector systems can be between 10 and 40, resulting in indicative temperatures between 60 and 250 °C, according to Kalogirou S. [19].

Figure 1.9: Linear Fresnel collector field at Puerto Errado 2 solar power plant [26].

1.2.2.3 Cylindrical Fresnel Lens Collector

The Fresnel lens collector systems use transparent materials to focus the rays coming from the Sun to the receiver, utilizing refraction instead of reflection. Compared to conventional lenses, which have large volumes and weights, Fresnel lenses are smaller in volume and lighter in weight. They are suitable for mass production at a low cost, with a presumed production method of injection molding. Commonly used materials for these lenses are polymethyl methacrylate (PMMA) and polycarbonate according to Ma et al. [27].

There are studies on similar topics using Fresnel lens solar collectors. Sample reading recommendations related to these topics include the desalination study by Wu et al. [28], studies on the use of the cavity receivers by Xie et al. [29] and [30], the review papers for coupling the Fresnel lens with CPTV, Sripadmanabhan Indira et al. [31], and wide-range review of the Fresnel lens solar collectors including chronologically ordered study references by Xie et al. [32].

Recent experimental studies by Ma et al. [27] and Ma et al. [33] on cylindrical Fresnel lens solar collectors provide numerical performance data. Ma et al. [27] indicate that their collector system reached operating temperatures around 250 °C at 1050 W/m^2 with a total aperture area of 2.6 m^2 and aperture width of 0.65 m at 83% optical

efficiency. Additionally, another experimental study related to cylindrical Fresnel lens solar collector focused on the thermal aspect of this kind of collector, by Ma et al. [33], reaches steady output temperatures of 125 °C, 150 °C, and 175 °C with collection efficiencies of 0.53, 0.48, and 0.44. The aperture width of this collector is 1.3 m, and the total installation area of the experimental setup is 20 m^2.

Figure 1.10: Experimental setup of a cylindrical Fresnel solar collector system, Ma et al. [34].

For the optical performance of the cylindrical Fresnel lens solar collector, Ma et al. [34] used the lens shown in Figure 1.10 and to focus the light on a lambert target and captured it with a charged-coupled device (CCD) camera, and obtained 81.6% real transmittance and a geometrical concentration ratio of 19.7. Moreover, in this experiment, under operating conditions of 0.2 and 0.5 MPa, collection efficiencies of 0.48 and 0.44, respectively. Additionally, an analysis made by Ma et al. [35] concludes that the geometric concentration ratios of 41.8 for PMMA at 28° and 29.2 for polycarbonate 20° for line-focusing Fresnel lens collectors are possible.

1.3 Solar Heat for Industrial Processes (SHIP) Applications

For the current industrial processes, the heating potential of the concentrating systems is gaining momentum. Market potential analysis performed by the European Solar Thermal Industry Federation [36] in 2006, 50% of the industrial processes would require heat up to 250 °C, including sectors such as food processing, chemical industry, textile industry, and others. Also, 74% of the global industrial energy demand, which accounts for 32% of the total global energy demand, is due to industrial heat, separates into three, 30% for processes requiring temperatures below 150 °C, 22% for processes requiring temperatures between 150 °C and 400 °C, and the rest of it is for processes requiring temperatures above 400 °C stated in the brochure by Solar Payback Project [9]. A more recent analysis regarding the industrial heat demand in Turkey by Difiglio et al. [12] states that sectors considered to require heat at low and medium temperatures account for 21% of the industrial heat demand.

Similar to electricity generation, there is a decrease in the installed costs in the SHIP applications. While the weighted-average installed costs of 11 SHIP projects were 1,679 USD/kW in 2017, the average installed cost of 15 plants is 531 USD/kW in 2020, resulting in a decrease of 68% as a result of support for larger deployments of these technologies according to Solrico [37].

Furthermore, solar collectors, especially the line-focusing collector systems whose operating temperatures can range from 150 °C to 400 °C could be used to supply the heat demand corresponding to low-temperature and medium-temperature heat processes.

1.4 Economics of the Current Systems

There is an effort for decreasing CAPEX and OPEX costs in solar energy technologies [14] for decreasing the cost of generating both electricity and heat. Current CSP systems, however, experience high CAPEX costs due to the structures and foundations.

Kurup P. and Turchi C.'s [17] findings about the final costs of installation per meter

squared of the widely used parabolic trough collectors for plant-scale installations which are 178$ for *Ultimate Trough* and 170$ for *SkyTrough*. For smaller installations, these costs tend to rise. In Tables 1.1 and 1.2, costs of CSP technologies in 2015 and cost estimations for 2025, published by Dieckmann et al. [24], are presented. These tables indicate that 23.5% and 28% decrease in CAPEX for these technologies, however, costs in 2015 show that construction costs for the parabolic trough collectors and the heliostat fields correspond to 38.1%, 29.4%, respectively, and the percentages of these costs do not decrease for predicted prices.

Table 1.1: Current and future specific CAPEX for parabolic trough field by component ($/m^2), published by Dieckmann et al. [24].

Parabolic trough solar field	**Costs 2015** [$/m^2]	**Cost variation** [%]	**Costs 2025** [$/m^2]
Site preparation	25	-20	20
Collector structure (incl. assembly)	66	-20	52
Pylons & foundations	22	-20	18
Drivers	7	-20	5
Mirrors	22	-15	19
Receivers	27	-30	19
Cabling	4.2	-10	3.7
HTF system (fluid)	21	-88	3
HTF system (excl. fluid)	38	0	38
Total	**231**	**-23.5**	**177**

HTF - Heat transfer fluid.

Table 1.2: Current and future specific CAPEX for the heliostat field by component ($/m^2), published by Dieckmann et al. [24].

Heliostat field	**Costs 2015** [$/m^2]	**Cost variation** [%]	**Costs 2025** [$/m^2]
Site preparation	11	-50	5.5
Mirrors	26	-35	16.9
Drivers	45	-25	33.8
Structure & foundation	42	-25	31.5
Controls	4	-20	3.2
Installation (wiring/foundation labor)	15	-20	12
Total	**143**	**-28**	**103**

1.5 Thesis Overview

The contents of this thesis are separated into three parts, the methodology and the theory for developed tools, optical and thermal analysis of the collector, and the investigation of the performance of the collector for the local conditions using actual typical meteorological year data.

In Chapter 2, the data related to the spectrum, the parameters, and the properties of the materials used in the simulation are obtained, the methodology related to the ray-tracing algorithm is explained, and the ray-tracing algorithm and the algorithm for designing the lens is presented. Then, the theory behind the convex lenses used for verifying the ray-tracing code is explained. For the last part of this section, the thermal model used for the heat loss calculation from the receiver is presented.

In Chapter 3, the results of the verification study, which is on the biconvex lenses, are presented. Then, the results of the parametric study on the optimal geometry are presented. The shape approximation and the sample size independence are studied, and the appropriate selection for both parameters is made. After that, the model parameters used in the ray-tracing simulations are given, and the results of the optical performance of the collector are presented. In Section 3.5, where the optical performance of the collector is discussed, the local concentration area is obtained, and the changes in the efficiency due to incidence angle around both transversal and longitudinal axes are given. In Section 3.6, the results of the thermal analysis are given along with verification of the model.

In Chapter 4, the methodology used for the seasonal and the annual performance analysis is presented, and the results of this analysis obtained for various providences are given. Additionally, by coupling the thermal analysis on the receiver and the annual model, temperature distribution for a day is obtained and presented.

The study is concluded in Chapter 5, and comments on the future work related to this study are made.

CHAPTER 2

THEORY AND METHODOLOGY

This chapter explains the methods used in the developed codes, as well as how the data required for the operation of these codes are obtained. Initially, the spectrum of rays emitted from the source plane that the code will use is specified, as well as how the random distribution of this spectrum is provided. After the initial explanation of reflection, refraction, and absorption of the rays as they interact with a lens, the following section delves into methods for calculating the intersection point of those waves. The methods used in the literature and the method used in this study are compared, and how the actual intersection point is distinguished is stated.

The algorithm for the developed ray tracing code is given, and it is stated which programming language the code is written in and which computer-aided design (CAD) software is being used to keep it organized and visualize it. Then, the methods for creating lenses that have been mentioned in the literature are stated, as well as the steps for creating the lens geometry that was used in this study, and the algorithm that was developed for that purpose is given. To ensure that the developed code functions correctly, software used in the industry is specified for comparison, explaining which parameters will be monitored.

The final section of the chapter explains how the one-dimensional thermal resistance analysis is performed on the receiver placed on the lens focal line, including the formulas to be used in the analysis.

2.1 Solar Irradiance and Probability Distribution of the Ray's Wavelength

Air mass coefficient quantifies the amount of light lost due to atmospheric absorption and scattering. The spectral distribution for the selected air mass coefficient, AM1.5 [38], presented in Figure 2.1, is used for generating probability distributions for the wavelength to be used as an input to the ray-tracing code and to account for the local conditions. To calculate the probability distributions, occurrences of the photons in bundles corresponding to the respective wavelengths are needed instead of the packed energy within those bundles. For that purpose, each one of the data points is adjusted according to their wavelengths using Equations 2.1 and 2.2, from Modest [39].

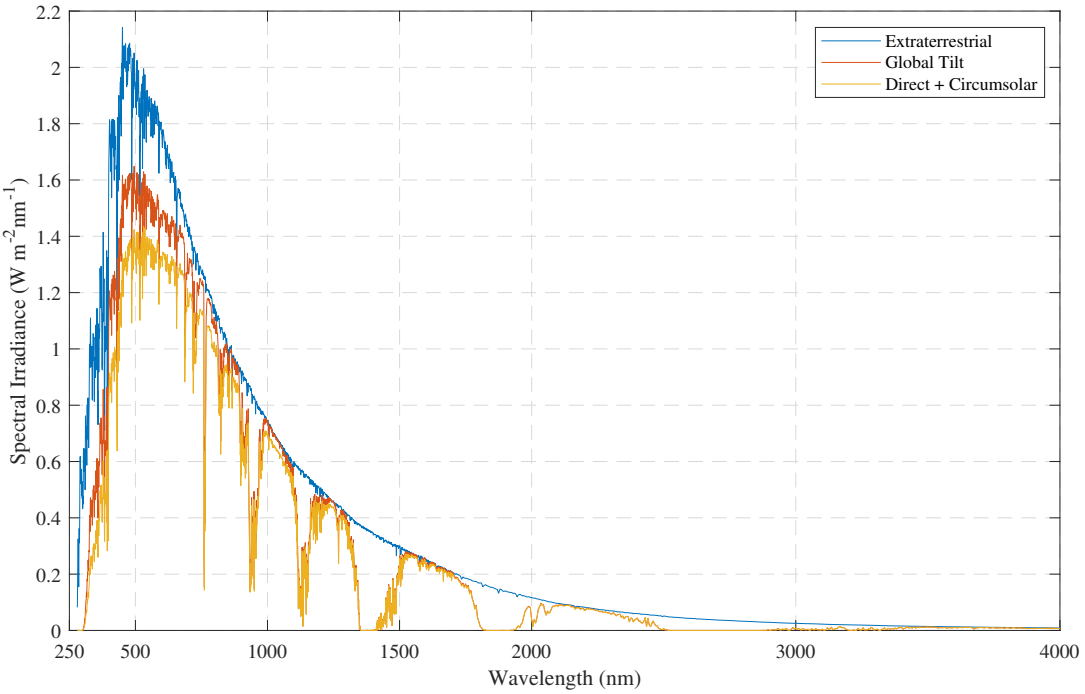

Figure 2.1: Spectral irradiance of the incoming rays for AM1.5, ASTM G173-03 Reference Spectra [38].

$$c = \frac{c_0}{n}, \qquad c_0 = 2.998 \times 10^8 \ \text{m/s} \tag{2.1}$$

$$\epsilon = \frac{h\, c_0}{\lambda\, n}, \qquad h = 6.626 \times 10^{-34} \text{Js} \tag{2.2}$$

The probability distribution and the cumulative probability of the distribution, indicating the occurrences of the photons, can be calculated for the spectrum between 400 nm and 4000 nm, considering the interval of the material properties. Thus, a random number generated between 0 and 1 can be assigned to a ray and can carry information related to its wavelength which is then calculated using the cumulative probability distribution. The probability distribution and the cumulative probability distribution calculated according to the direct and circumsolar irradiation data given in the reference spectra are presented in Figure 2.2.

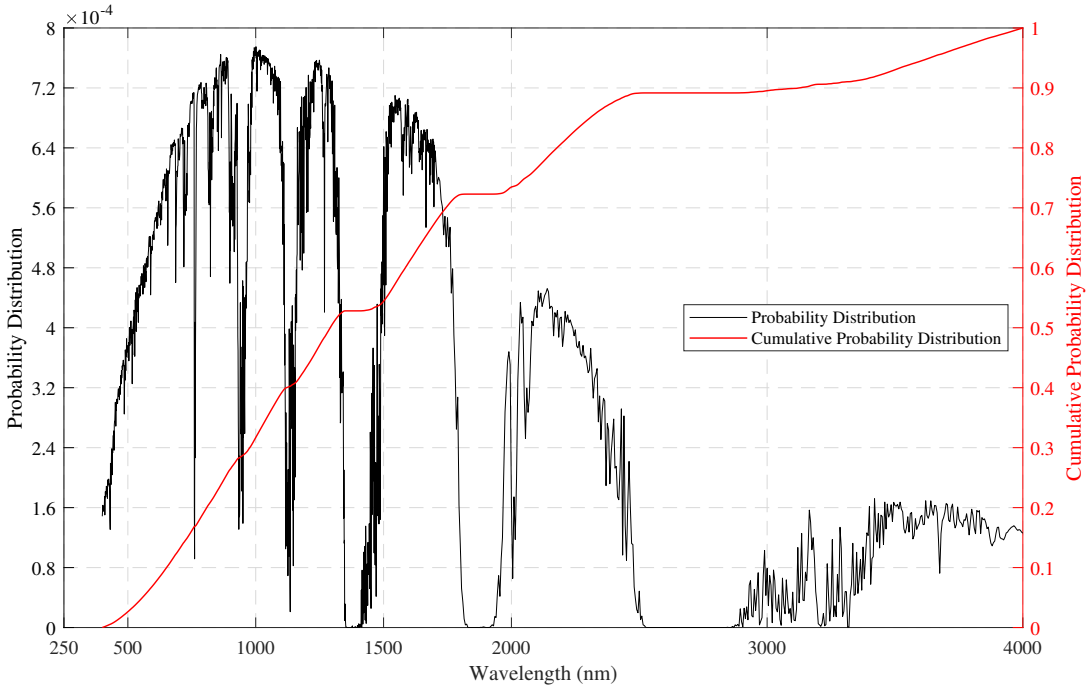

Figure 2.2: Probability distributions of the rays, calculated according to the direct and circumsolar spectral irradiance included in ASTM G173-03 Reference Spectra [38].

2.2 Events in Consideration Between the Rays and the Lens Medium

The determination of the events happening when the rays intersect with the lens surfaces and pass through its medium is another aspect of the tracing procedure. Furthermore, the reflection and the refraction are demonstrated in Figure 2.3. Refraction angle, θ_2, which corresponds to the angle between the surface normal and the direction vector in the new medium is found using the ray incidence angle, θ_1, the refractive index, n, and the extinction coefficient, k, of the material of the lens.

Modest [40] describes Snell's law, given as Equation 2.3, applied to the refractions between two dielectric mediums, and generalized Snell's law, given by Equations 2.4, 2.5, and 2.6, used for the refraction angle calculation between a dielectric medium and an absorbing medium. The difference between these two sets of equations is the inclusion of the extinction coefficient, which accounts for the losses in energy and the deviations in ray-tracing simulations. Furthermore, the losses arising from the absorption within the medium and the deviations should be taken into account. However, these equations that utilize the extinction coefficient may burden unnecessary computations to the simulations. Therefore, the extinction coefficient should be considered in calculations where it substantially affects the results.

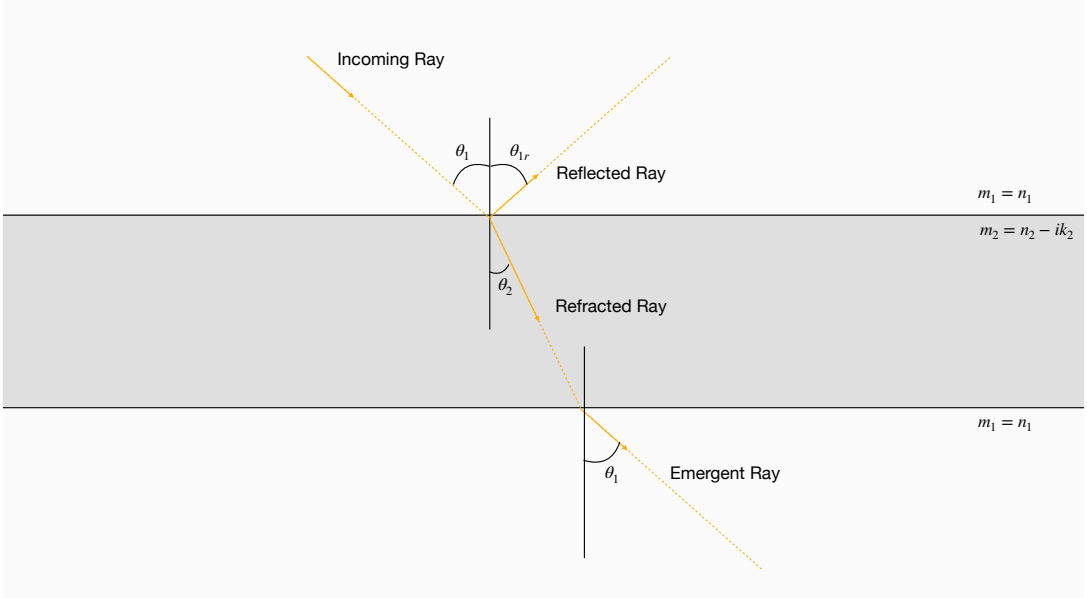

Figure 2.3: Events happening at the interface between two mediums.

$$n_2 \sin\theta_2 = n_1 \sin\theta_1 \tag{2.3}$$

$$p^2 = \frac{1}{2}\left(\sqrt{n_2^2 - k_2^2 - n_1^2\sin^2\theta_1 + 4n_2^2k_2^2} + (n_2^2 - k_2^2 - n_1^2\sin^2\theta_1)\right) \tag{2.4}$$

$$q^2 = \frac{1}{2}\left(\sqrt{n_2^2 - k_2^2 - n_1^2\sin^2\theta_1 + 4n_2^2k_2^2} - (n_2^2 - k_2^2 - n_1^2\sin^2\theta_1)\right) \tag{2.5}$$

$$p\tan\theta_2 = n_1 \sin\theta_1 \tag{2.6}$$

The differences observed between the results acquired using Equations 2.3 and 2.6 while calculating the refraction angle for polycarbonate seem negligible. A sample of results for different wavelengths and incidence angles, which illustrates the difference between using Equations 2.3 or 2.6, is given in Figure 2.4. Therefore, Equation 2.3 is preferred for the refraction angle calculation step of the ray tracing done during this work.

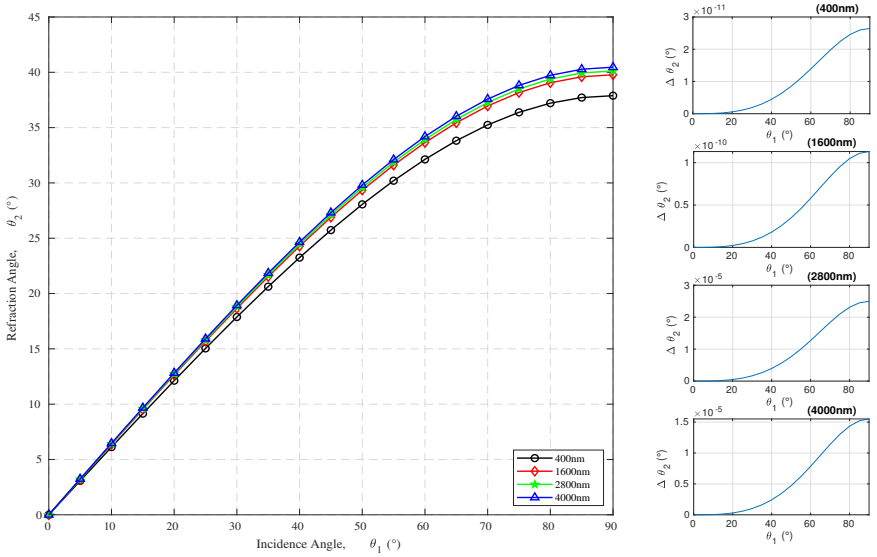

Figure 2.4: Sample of results for refraction angle calculation using different incidence angles and different wavelengths, *(left)* using Equation 2.3, and *(right)* the difference between the two equations.

Although the transmissivity of the medium is usually taken as an average value or an array of values dependent on the wavelength, the extinction coefficient should be considered due to varying and increasing optical loss within the medium depending on the length of the path of the ray. The refractive index and the extinction coefficient of the polycarbonate, reported by Zhang et al. [41] [42], and the change in the internal transmittance for different thicknesses, calculated using Equations 2.7 and 2.8, gathered from Modest [43], are plotted in Figure 2.5 between 400 and 4000 nm.

Similar to the polycarbonate, the refractive index and the extinction coefficient of the low-iron-borosilicate glass used for the receiver envelope, calculated using the data from Rubin M. [44], are given in Figure 2.5.

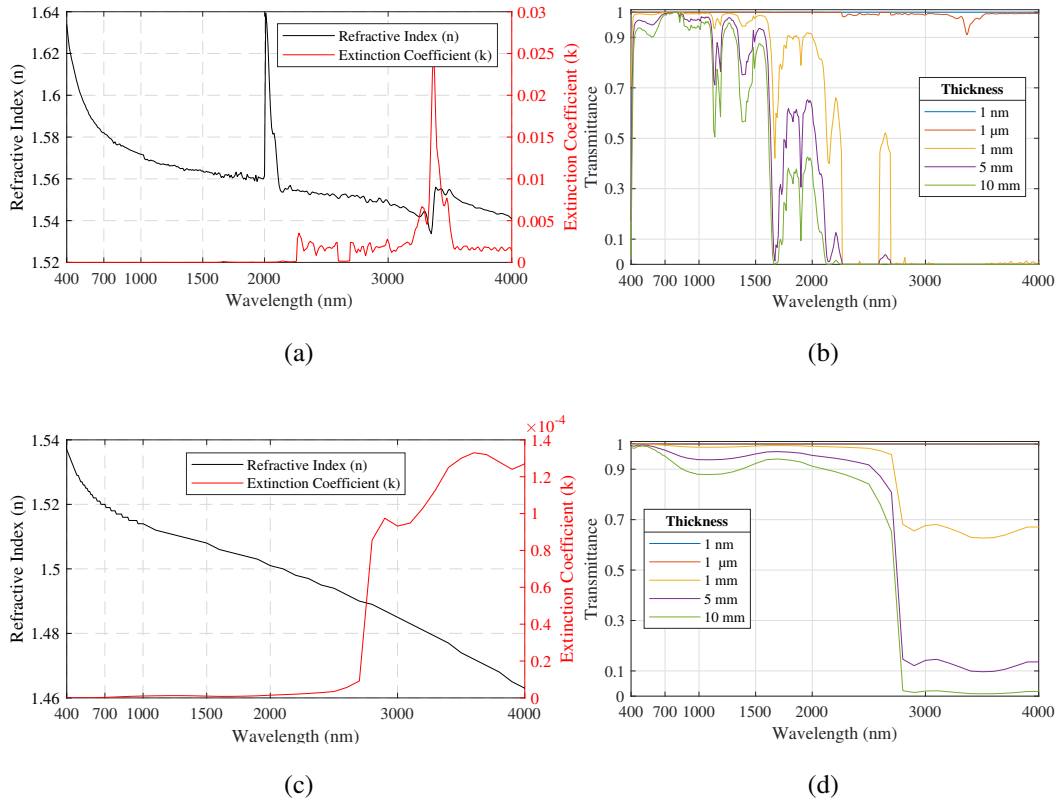

Figure 2.5: Terms of the complex refractive index of polycarbonate *(a)* and its internal transmittance for different thicknesses *(b)*, terms of the complex refractive index of low-iron borosilicate *(c)* and its internal transmittance for different thicknesses *(d)* and between 400 and 4000 nm.

$$\kappa = 4\pi\eta_0 k = \frac{4\pi k}{\lambda_0}, \quad \text{where} \quad \lambda_0 = \frac{1}{\eta_0} = \frac{c_0}{v} \tag{2.7}$$

$$\tau = e^{-\kappa s} = e^{-4\pi k s \,/\, \lambda_0} \tag{2.8}$$

Additional losses occur at the lens surfaces due to the reflectivity, notably dependent on the angle of incidence, θ_1. The parallel and perpendicular components of the reflectivity is calculated using Equations 2.9 & 2.12 and 2.10 & 2.13, respectively. The reflectivity of the interface of between the transparent mediums can be calculated using Equations 2.9 and 2.10, together with Equation 2.11. Furthermore, the reflectivity equation coupled with the generalized Snell's law, which accounts for the complex refractive index, Equations 2.12 and 2.13 can be used together with the first half of Equation 2.11.

$$\rho_{\parallel} = \left(\frac{n_1 \cos\theta_2 - n_2 \cos\theta_1}{n_1 \cos\theta_2 + n_2 \cos\theta_1} \right)^2 \tag{2.9}$$

$$\rho_{\perp} = \left(\frac{n_1 \cos\theta_1 - n_2 \cos\theta_2}{n_1 \cos\theta_1 + n_2 \cos\theta_2} \right)^2 \tag{2.10}$$

$$\rho = \frac{\rho_{\parallel} + \rho_{\perp}}{2} = \frac{1}{2} \left[\frac{\tan^2(\theta_1 - \theta_2)}{\tan^2(\theta_1 + \theta_2)} + \frac{\sin^2(\theta_1 - \theta_2)}{\sin^2(\theta_1 + \theta_2)} \right] \tag{2.11}$$

$$\rho_{\parallel} = \frac{(p - n_1 \sin\theta_1 \tan\theta_1)^2 + q^2}{(p + n_1 \sin\theta_1 \tan\theta_1)^2 + q^2} \rho_{\perp} \tag{2.12}$$

$$\rho_{\perp} = \frac{(n_1 \cos\theta_1 - p)^2 + q^2}{(n_1 \cos\theta_1 + p)^2 + q^2} \tag{2.13}$$

Similar to the previous step, where the refraction angle is calculated, differences between the results acquired by using these two sets of Fresnel relations are negligible. The sample of these results and their differences, at a maximum of around 1%, are illustrated in Figure 2.6. Therefore, Equations 2.9 and 2.10, which do not consider the extinction coefficient, are preferred for the reflectivity calculation step of this work.

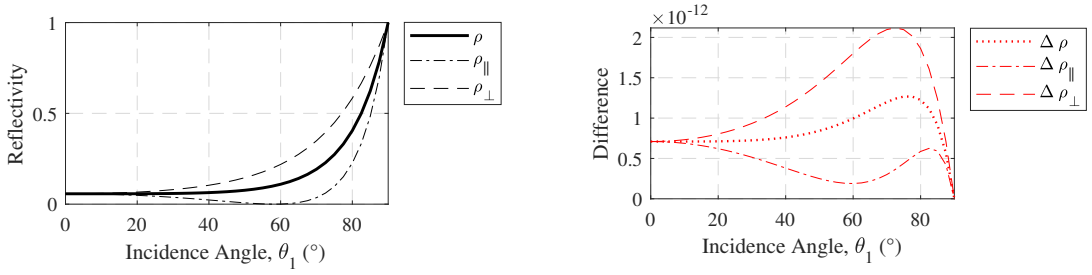

(a) 400nm

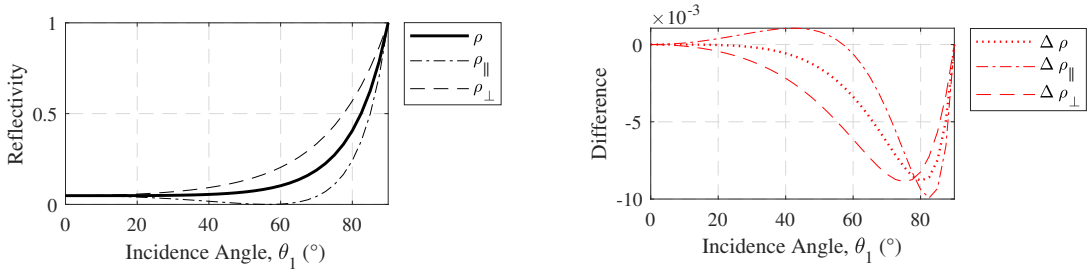

(b) 1600nm

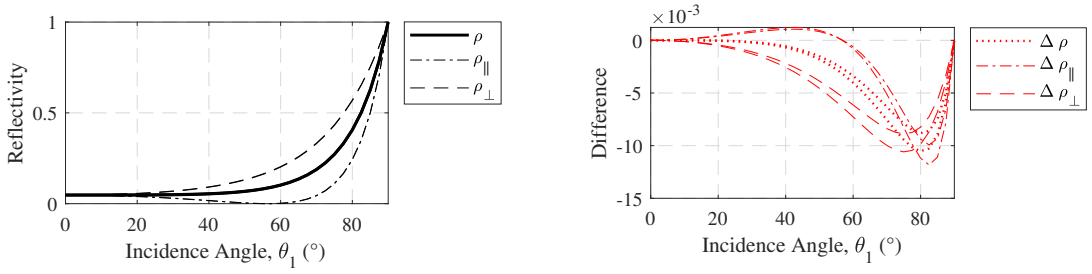

(c) 2800nm

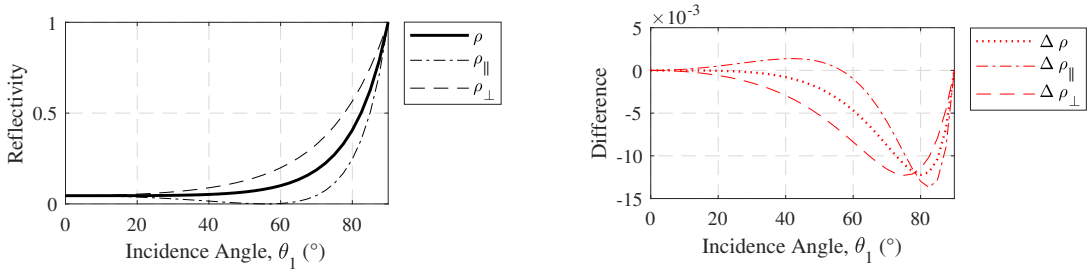

(d) 4000nm

Figure 2.6: Reflectivities of the polycarbonate and differences between two sets of equations, Equations 2.9 & 2.10 and 2.12 & 2.13, for the incidence angles between 0° and 90°. *(a) 400 nm, (b) 1600 nm, (c) 2800 nm, and (d) 4000 nm.*

2.3 Ray-Element Intersection

The probable intersection point is calculated on the plane where the element lies within, using Equations 2.14 to 2.17. The first equation is to determine whether there is an intersection and the second is to determine the probable intersection point. Considering the properties of the dot product rule, the second is simplified using Equations 2.16 and 2.17 is obtained.

$$S_{dp} = \overrightarrow{N_{plane}} \cdot \overrightarrow{V_{ray}} \tag{2.14}$$

$$P_h = \overrightarrow{P_pP_s} - \frac{\overrightarrow{N_{plane}} \cdot \overrightarrow{P_pP_s}}{\overrightarrow{N_{plane}} \cdot \overrightarrow{V_{ray}}} \overrightarrow{V_{ray}} + P_p \tag{2.15}$$

$$\frac{\overrightarrow{N_{plane}} \cdot \overrightarrow{P_pP_s}}{\overrightarrow{N_{plane}} \cdot \overrightarrow{V_{ray}}} = \frac{|\overrightarrow{N_{plane}}|\ |\overrightarrow{P_pP_s}|\ cos(\alpha)}{|\overrightarrow{N_{plane}}|\ |\overrightarrow{V_{ray}}|\ cos(\beta)} \tag{2.16}$$

$$P_h = \overrightarrow{P_pP_s} - \frac{|\overrightarrow{P_pP_s}|\ cos(\alpha)}{|\overrightarrow{V_{ray}}|\ cos(\beta)} \overrightarrow{V_{ray}} + P_p \tag{2.17}$$

Geometrical representation of the vector operations preferred in this work for ray-plane intersection calculation, the equations above with additional information related to angles between the vectors and their respective projections onto each other are demonstrated in Figure 2.7.

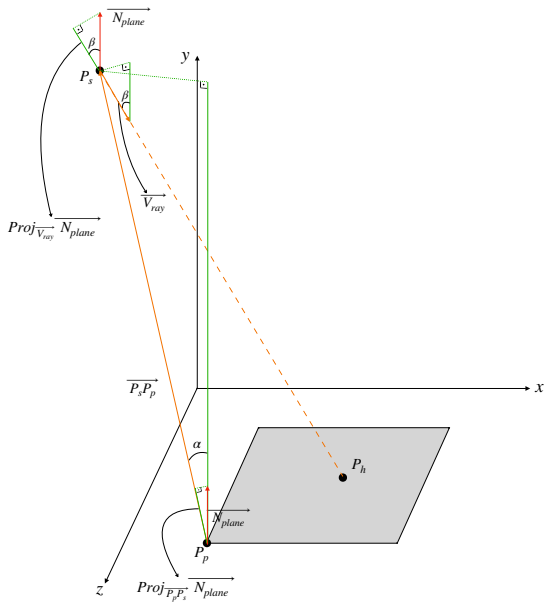

Figure 2.7: Vector operation related to intersection point calculation on a plane containing an element.

In addition to finding probable intersection points, there is a need for an algorithm for determining whether the probable intersection point is within the element and whether an intersection exists or not. To do this using meshed geometries, there are a couple of algorithms and methods, which can be classified as ray-triangle intersection, ray-polygon intersection, and bounding box control. Likewise, solving three-dimensional equations of the bodies is another option for ray-surface intersection calculation if the geometry is defined appropriately. However, as the complexity of the geometry increase, this method becomes difficult to implement and costly in terms of computational power and run-time.

Fundamental works related to the ray-triangle intersection algorithms focus on the barycentric coordinates within a triangle. Barycentric coordinates can be defined as a correlation using the edge vectors of a triangle or other convex polygons to describe every single point on the area defined by the polygon. Snyder, J. M., and Barr, A. H. [45] describe an algorithm to compute ray-triangle intersections using barycentric coordinates. The aim of their work, published in 1987, is described as ray tracing complex models containing mathematically defined surfaces to extend the list of *"ray-traceable"* surfaces. The algorithm calculates the normal vector of the plane, containing the triangle, finds an intersection point on that plane, and performs an enclosure test using the barycentric coordinates. In 1990, Baudel D. [46] describes an algorithm, quite similar to the work of Snyder, J. M., and Barr, A. H. [45], by introducing additional parameters to simplify the calculation steps and obtain faster runs. In 1997, Möller T. and Trumbore B. [47] proposed one that also utilizes barycentric coordinates, and as an initial step, it manipulates the equation system of the intersection to obtain a translation of the element to the origin and transform it into a unit triangle in yz-plane with ray direction in the x-axis.

Ray-polygon intersection algorithms, as described by Akenine-Möller et al. [48], indulge in finding whether the probable intersection point is contained in the polygon, reducing the solution to two dimensions, in a more detailed fashion, i.e., self-intersecting and/or concave polygons with a rather high number of edges. Schneider P. and Eberly D. [49] describe a ray-convex polygon intersection algorithm and two other, asymptotically faster algorithms one of which is a derivative of the first. Additionally, for complex polygons intersections reduced to the two-dimensional domain,

Akenine-Möller et al. [48] and O'Rourke, J. [50] outline an algorithm called the *"ray crossings test"*. In this algorithm, a ray is cast from the point in question to the infinity in a direction on the plane of the polygon, and line segment intersections between the ray and the edges are calculated and the number of true returns is counted. The decision on whether the point is in the polygon or not is made based on the number of true returns, i.e., odd numbers mean that the point is in the polygon, and even numbers mean otherwise.

For the element translation from the output of the ray-tracing code to the input to the computational domain for further simulations, the quadrilateral element is considered a reasonable choice for the element shape for the geometry studied in this work. Thus, the higher quality approximation can be generated in the simulation software by refining the former approximation in the extruded direction effortlessly and without the hassle of skewed elements. However, the decision indicated requires a approximation independence study on the curved surfaces. The surface approximation independence study regarding ray-tracing could conceivably be made in two dimensions.

In this case, the methodology defined by Schneider P., and Eberly D. [49] is preferred for determining whether an intersection occurs between the element and the ray cast, due to its simplicity and consistency of it together with the vector operations written in the ray-tracing code. A sample of the vector operations regarding this intersection algorithm demonstrated for an edge is presented by Equations 2.18, 2.19, and 2.20, and Figure 2.8. The ray cast from point P_s with the directional vector of $\overrightarrow{V_{ray}}$ is assumed to be intersecting the x-z plane at point P_h. For the element in consideration, surface normal, $\overrightarrow{N_{surf}}$, edge vectors, $\overrightarrow{V_{e1}}$ to $\overrightarrow{V_{e4}}$, and vertex-to-intersection vectors, $\overrightarrow{V_{h1}}$ to $\overrightarrow{V_{h4}}$, are calculated. Then, for each edge, by taking cross products of the surface normal of the element with each of the edge vectors, vectors, $\overrightarrow{V_{cp1}}$ to $\overrightarrow{V_{cp4}}$, perpendicular to both is obtained. Furthermore, representative projections of the vertex-to-intersection vectors to the vectors expressed with $\overrightarrow{V_{cp}}$ are performed by dot product operations. The sign of the result of the dot product operation indicates the position of the intersection relative to the edge vector. Therefore, if signs of these results comply, it can be said that an intersection exists.

$$\overrightarrow{V_{h1}} = \overrightarrow{P_h} - \overrightarrow{P_{e1}} \tag{2.18}$$

$$\overrightarrow{V_{cp1}} = \overrightarrow{N_{surf}} \times \overrightarrow{V_{e1}} \tag{2.19}$$

$$S_{dp1} = \overrightarrow{V_{h1}} \cdot \overrightarrow{V_{cp1}} \tag{2.20}$$

On the left side of Figure 2.8, sample vector operations for a ray intersecting an element are given. The resulting projection is in the same direction as the vector obtained by the cross-product of the surface normal and the edge vector. On the right side of Figure 2.8, similar operations for a ray missing and element are given. The projection is in the opposite direction with the $\overrightarrow{V_{cp}}$ for that edge.

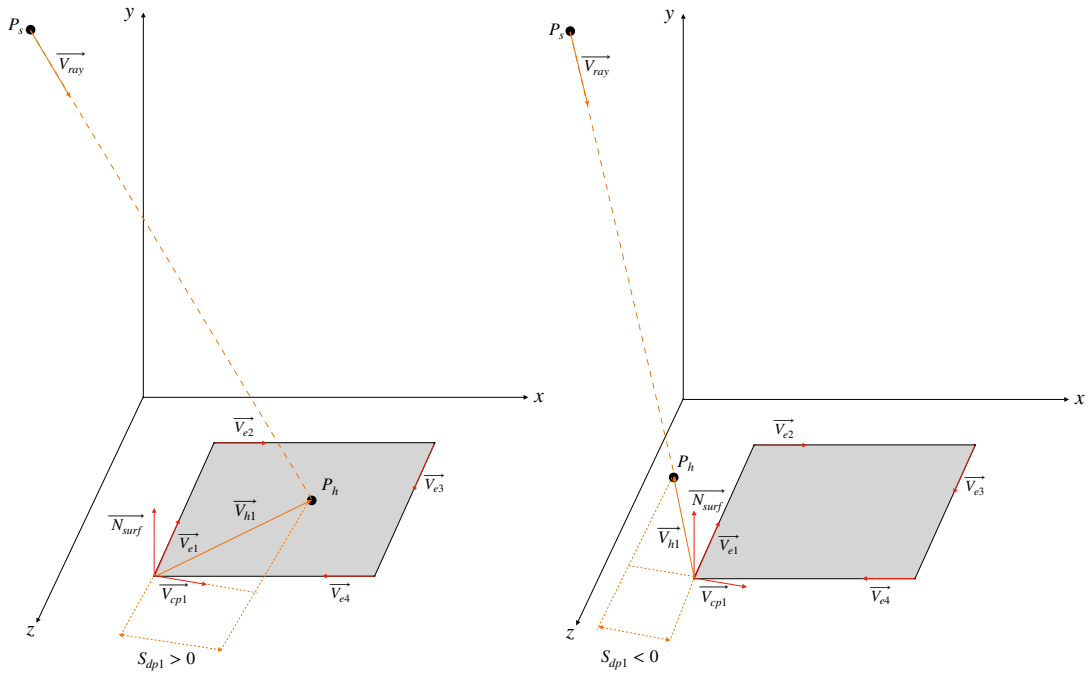

Figure 2.8: Sample vector operations for determining whether the ray intersects with the quadrilateral element *(left)* or not *(right)*.

In addition to these two main steps, a final step that can separate the multiple intersections and determine the actual intersection is required. To perform this operation, an additional simple code is written for finding the distances in the correct direction and ranking them to reach the verdict for the closest intersection.

2.4 Algorithm of the Developed Ray Tracing Code

The purpose of this algorithm, presented in Figure 2.9, is to implement operations laid down in Sections 2.1, 2.2, and 2.3, to trace rays emitted from the source plane, and to observe and account for the interactions in a proper order, which is calculating the eventual trajectory in an accurate and fast manner.

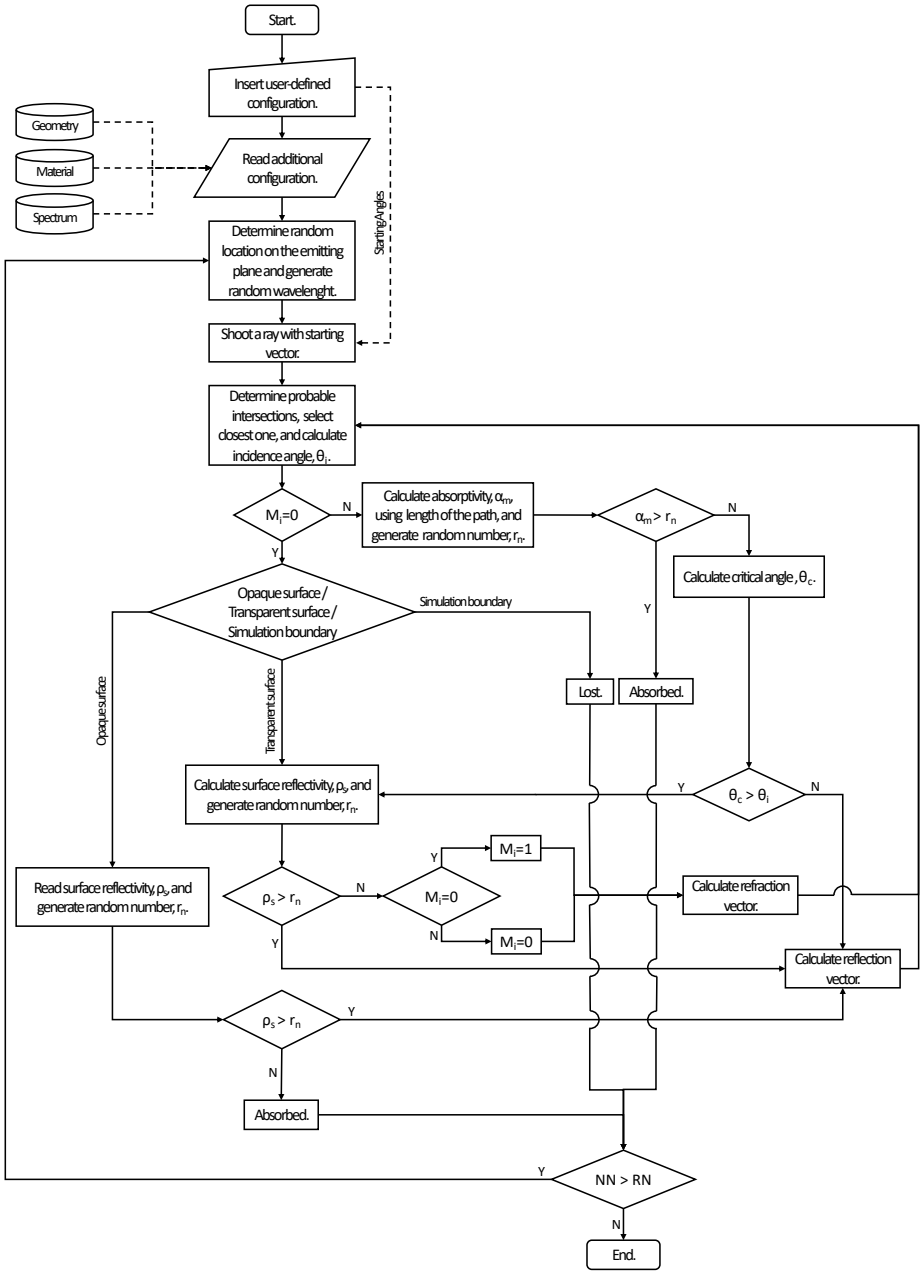

Figure 2.9: Algorithm used for the ray tracing simulation.

At the second and third steps of the simulation, user-defined and additional configurations are read. The user-defined configuration consists of the number of rays that are emitted from the source plane, *NN*, their starting angles, α and β, and the source plane's size and location. Additional configuration includes pre-defined properties of the geometry, the materials, and the spectrum in consideration. After reading the configurations, rays are emitted from the random location on the source plane with starting angles defined in the configuration and a random wavelength between 400nm to 4000nm. After that, the simulation follows the checks and the loops given in Figure 2.9.

Through these operations, to decrease memory usage, large datasets, such as the intersection points and other ray-related information, are saved to data files. These files could also be used for post-processing and verification purposes. Furthermore, the algorithm is implemented in *Julia* [51], a fast programming language with embedded functions. It can handle large data sets and works harmoniously with *GMSH* [52], a 3D finite element mesh generator with a built-in CAD engine. Apart from generating mesh and storing geometry files, *GMSH* is also used as a graphical user interface (GUI) for visualization of the simulation. A screenshot from the *GMSH* environment is given in Figure 2.10.

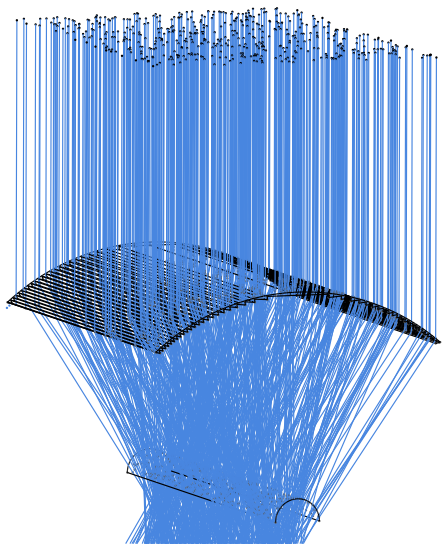

Figure 2.10: Screenshot, taken at the *GMSH* environment, of the simulation results for a preliminary run.

2.5 Algorithms for the Creation of the Lens Geometries

Fresnel lenses work with the same principle as conventional lenses work. Through refractions at different angles of the interfaces between the mediums, they focus or collimate light depending on the application. Figure 2.11 illustrates the geometrical representation of the imaging principle and the creation procedure of a focusing Fresnel lens. By extracting thicker, mostly unnecessary volume, but keeping the angles at the interfaces between the mediums of a conventional convex lens, thin lenses, such as a Fresnel lens or a cylindrical Fresnel lens, can be obtained.

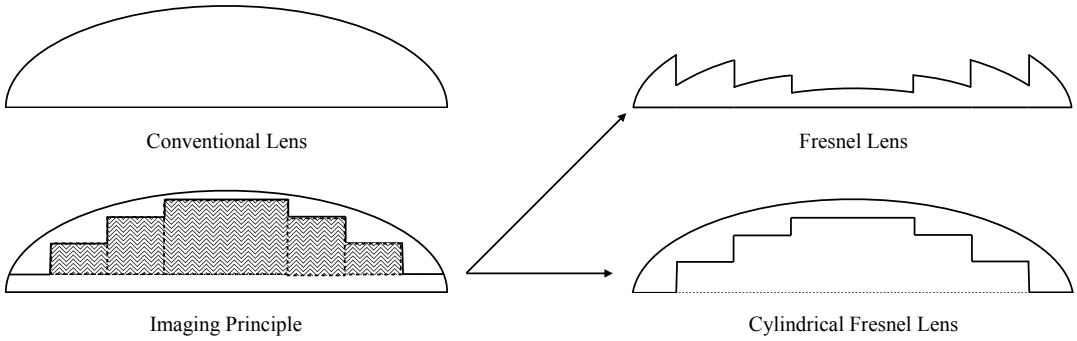

Figure 2.11: Imaging principle and the creation procedure of Fresnel lenses.

Further manipulation regarding the position of the line of focus can be achieved by adjusting the angles of the prisms, in other words, serrations. Moreover, for the application of solar concentration, energy losses should be reduced. Therefore, the targeted position of the line of focus should be met by adjusting the angles of the serrations, since the thickness of a lens contributes to the transmissivity of the lens.

On the assumption that these serrations' primitive form is triangular prisms, Figure 2.12, prepared by Ma et al. [33], illustrates the traces of the rays transmitting through a triangular prism. Knowing that the upper surface of the lens is a pre-determined shape, only the lower surfaces are available for manipulation.

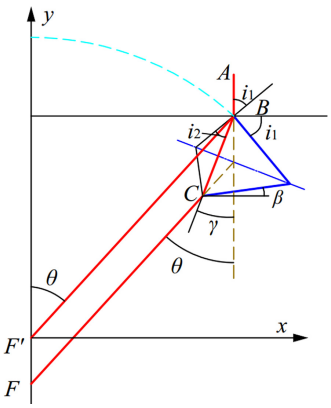

Figure 2.12: Traces of the rays transmitting through the lens. [33]

By applying Snell's law of refraction to a triangular prism, Ma et al. [35] derive a differential equation for theoretical ideal curves of the Fresnel lenses. Furthermore, an analysis for variations of transmittance with total refracted angle, meaning the difference between the incidence angle and the emergent angle, and refractive index of the lens material has been made. In another study that also examines the lens creation procedure, Zheng et al. [53] apply Snell's law of refraction to a serration with a circular upper surface and calculate the edge coordinates of the Fresnel lens which has its line of focus positioned around the diameter away from the most upper point of the lens.

In this work, a Fresnel lens, that has its line of focus positioned at the center of the lens, is preferred by design. Moreover, exploiting the procedure defined by Zheng et al. [53] is possible by changing variables such as the thicker height, the thinner height, or preemptively the design distance of the line of focus. However, from an overall perspective, these are not scientifically based manipulations. Therefore, in like manner to ray tracing, an algorithm-based approach is deemed appropriate.

The algorithm uses the incremental search method to find the thinnest lens that can focus on an object is developed and Figure 2.14 depicts its steps. This algorithm uses a different intersection methodology than the ray-tracing algorithm. As a result of this, this algorithm is not affected by the approximation quality, thus, it does not require a approximation independence study. Serrations in the lens are created one by one, starting from the most inner serration. They are also created with the largest allowable width and the smallest overall height for the least optical loss due to absorption.

For the non-planar surfaces of the lens, the shape is approximated using lines in two-dimension and rectangles in three-dimension. The illustration for shape approximation for the cylindrical surfaces is presented in Figure 2.13.

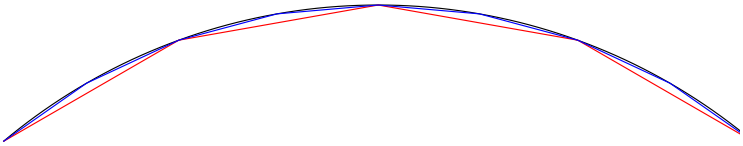

Figure 2.13: 2D representation of the surface approximations during the creation procedure of Fresnel lenses.

Aftermost, a geometry file that is *GMSH* and *Julia* compatible is created with incrementally found serrations. Furthermore, other parts within the simulation environment and the material-related information are added to the geometry file.

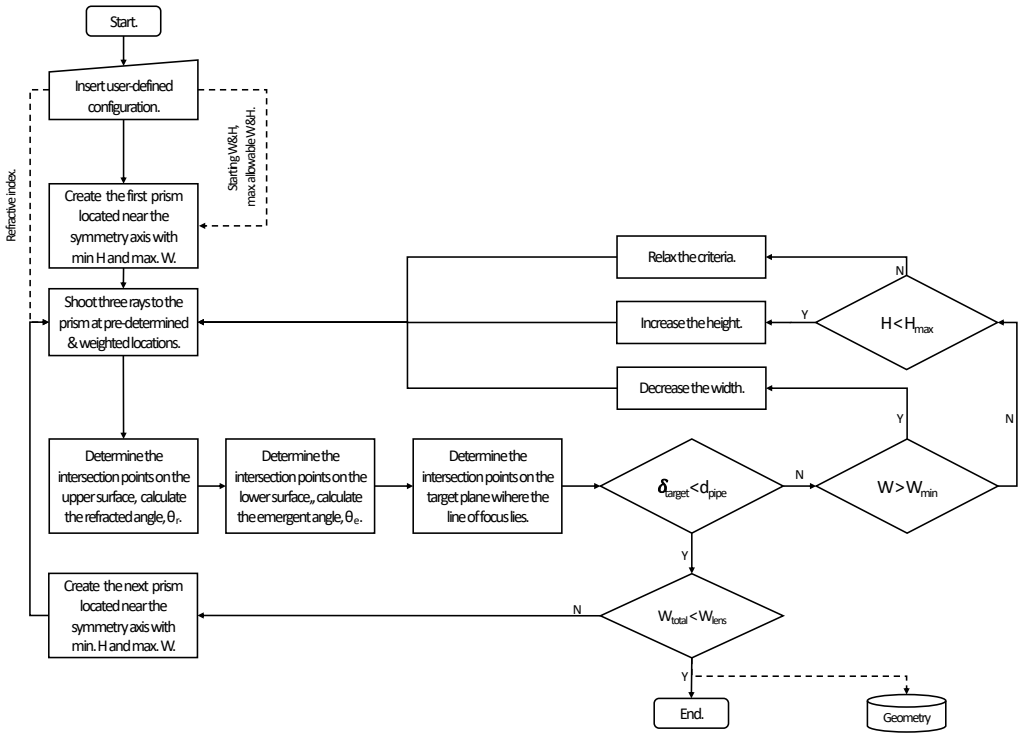

Figure 2.14: Algorithm related to the creation of the lens geometries.

2.6 Verification of the Ray-tracing Code

To verify the calculations and the providing accountability concerning the ray-tracing code, performing four other ray-tracing simulations utilizing the developed code alongside a commertial software using two biconvex lenses and two planar-convex lenses is proposed. The reason behind using two different types of lenses is to provide one simulation free of chromatic aberration and one with decreased spherical aberration and also without chromatic aberration. The biconvex lens is considered to be a thick lens, which can be calculated using the Lensmaker's equation, given by Equation 2.21 given in Hecht E. [54]. Also, equations for determining the focal length of the planar-convex lenses are presented as Equation 2.22, derived from Equation 2.21 as R_1 is replaced with an infinitely large number, resulting in those terms including it to approach zero. In these equations, effective focal length, f, is calculated using the refractive index of the lens n_l, radii of the spherical surfaces, R_1 and R_2, and the thickness of the lens, d_l.

$$\frac{1}{f_{lens}} = (n_{lens} - 1)\left[\frac{1}{R_1} - \frac{1}{R_2} + \frac{(n_{lens} - 1)\, d_{lens}}{n_{lens} R_1 R_2}\right] \tag{2.21}$$

$$\frac{1}{f_{lens}} = (n_{lens} - 1)\left[-\frac{1}{R_2}\right] \tag{2.22}$$

Although these equations are for the ideal lenses that are not affected by the defects such as aberrations, they are useful for acquiring preliminary information about these lenses. The aberrations are categorized as monochromatic aberrations, such as spherical aberrations, comma, astigmatism, field of curvature, and distortion, and chromatic aberrations as explained in Hecht E. [54]. While the chromatic aberrations are due to wavelength dependency of the refractive index of the lens material, the monochromatic aberrations are deviations of light from its path due to non-idealized conditions related to the lens shape.

In this work, primarily the effects of the chromatic aberrations and the spherical aberration will be investigated. Foremost, the aberration due to the difference in focal lengths between the rays closer to and the rays further from the principal axis is called spherical aberration. To elaborate, the rays closer to the principle axis meet at

a long distance after refraction while rays far from the principal axis meet at a shorter distance. Secondly, in definition, chromatic aberrations arise from the fact that the refractive index is a function of color, as stated in Hecht E. [54], therefore rays with different wavelengths would refract at different angles. Lastly among all mentioned aberrations, the effects of comatic aberration on the concentrator will be discussed. The representations of these three effects are illustrated in Figure 2.15, obtained from Hepp J. [55].

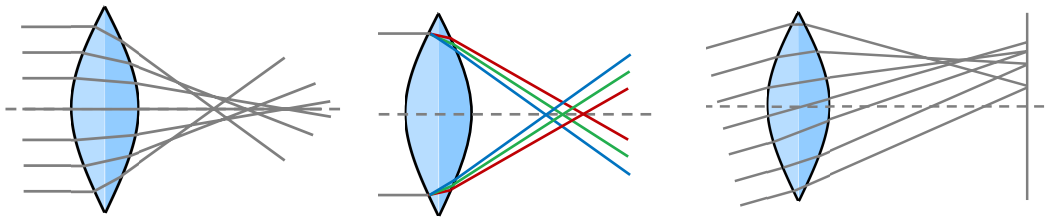

(a) (b) (c)

Figure 2.15: Some of the aberration types [55]. *(a) Spherical aberration, (b) Chromatic aberration, (c) Comatic aberration.*

In the verification study, however, only the spherical aberration will be taken into account and used for determining the focal spot sizes at different locations. These spot sizes, in comparison with simulations conducted in commercial software, will be used for determining the accuracy of the written ray-tracing code.

2.7 Thermal Model

The performance of the collector is determined by the heat added to the heat transfer fluid within the collector. In order to accurately model the receiver's thermal behavior, losses from the system must be taken into account and incorporated into an energy balance equation. The heat transfer network model of the receiver is illustrated in Figure 2.16, adapted from Kalogirou S. A.[56].

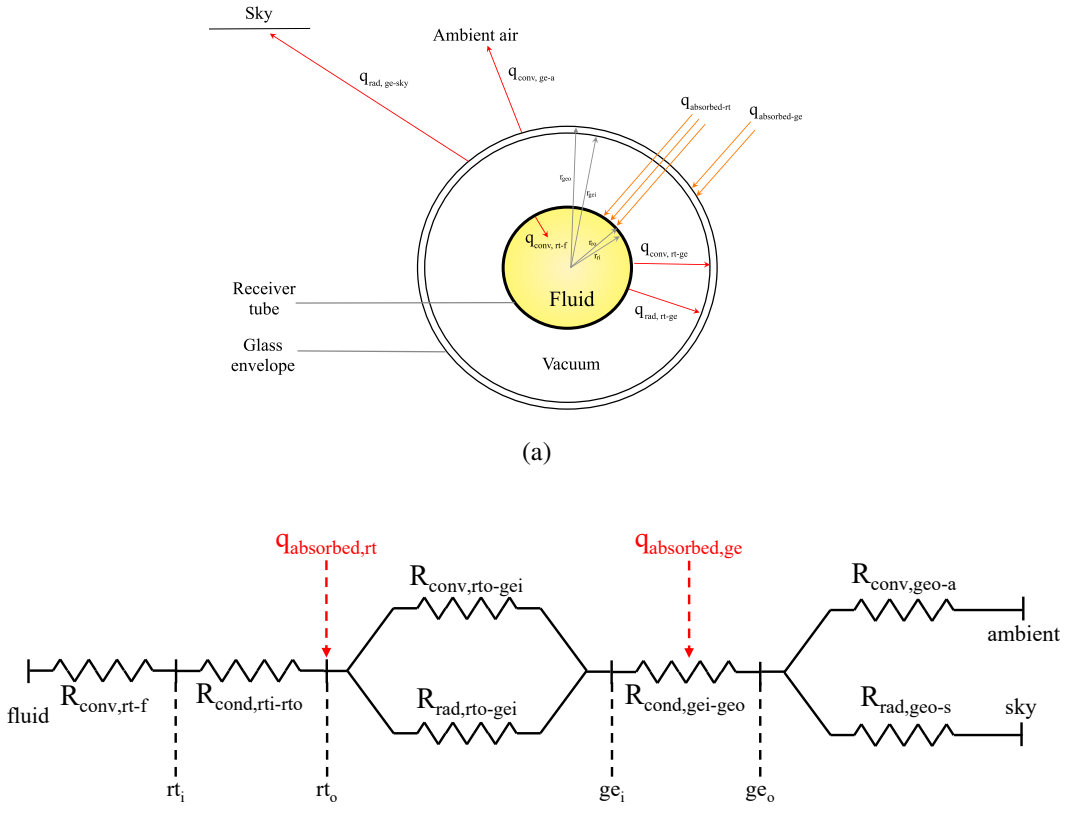

Figure 2.16: (a) The receiver flux representations and (b) the heat transfer network model of the receiver, adapted from Kalogirou S. A. [56]. *From left to right, the domains are the fluid domain, the receiver tube, the annulus, the glass envelope, the ambient air, and the sky.*

And the energy balance of this receiver for the steady-state conditions, i.e. no accumulation, is written as Equations between 2.23 to 2.27.

$$q_{cond,rt_i-rt_o} = q_{conv,f-rt_i} \tag{2.23}$$

$$q_{absorbed,rt} = q_{cond,rt_i-rt_o} + q_{conv,rt_o-ge_i} + q_{rad,rt_o-ge_i} \tag{2.24}$$

$$q_{conv,rt_o-ge_i} + q_{rad,rt_o-gei} = q_{cond,ge_i-ge_o} \tag{2.25}$$

$$q_{cond,ge_i-ge_o} + q_{absorbed,ge} = q_{conv,ge_o-a} + q_{rad,ge_o-s} \tag{2.26}$$

$$q_{loss} = q_{conv,ge_o-a} + q_{rad,ge_o-sky} \tag{2.27}$$

The receiver is evacuated which results in a negligible convective transfer inside the annulus, between the receiver tube and glass envelope. Following the energy balance and the analysis in Kalogirou S. [56] with a couple of simplifications, the terms in the equations and the assumptions for finding their values are as shown between Equations 2.28 and 2.46.

The convective heat transfer between the working fluid and the receiver tube is calculated by Equation 2.28,

$$\begin{aligned} q_{conv,rt-f} &= h_f A_{rt-f} \Delta T_{rt-f} L \\ &= h_f \pi D_{rt_i} (T_{rt_i} - T_f) L \end{aligned} \tag{2.28}$$

where the convective heat transfer coefficient for the flow inside the receiver tube is given by Equation 2.29,

$$h_f = Nu_{D_{rt_i}} \frac{k_f}{D_{rt_i}} \tag{2.29}$$

and the Nusselt number for the flow inside the tube is taken as 4.36 for laminar flow assuming constant heat flux, and calculated using Petukhov-Popov correlation [57], valid between $4000 < Re < 5\ 10^6$ with an accuracy of ± 5 %, given by Equation 2.28, coupled with the Bhatti-Shah correlation [57] for the friction factor with an accuracy of ± 2 %, given by Equation 2.30, if the flow is turbulent.

$$
\begin{aligned}
Nu_{D_{rt_i}} &= \frac{(f/2)Re_{D_{rt_i}}Pr_f}{C + 12.7(f/2)^{1/2}(Pr_f^{2/3} - 1)} \\
C &= 1.07 + \frac{900}{Re_{D_{rt_i}}} - \frac{0.63}{1 + 10Pr_f}
\end{aligned}
\tag{2.30}
$$

$$
\begin{aligned}
f =& A + B \;\; Re_{D_{rt_i}}^{-1/m} \\
& \mathrm{A} = 0.0054, \mathrm{B} = 2.3\ 10^{-8}, \mathrm{m} = -2/3 \quad \text{for } 2100 < \mathrm{Re} < 4000 \\
& \mathrm{A} = 0.00128, \mathrm{B} = 0.1143, \mathrm{m} = 3.2154 \quad \text{for } 4000 < \mathrm{Re} < 10^7
\end{aligned}
\tag{2.31}
$$

If Reynold's number indicates that the flow regime is in transition, then by using both Nusselt numbers for laminar and turbulent flows in the Taborek's correlation [57], which is valid between $2000 < Re < 8000$, given by Equation 2.32,

$$
\begin{aligned}
Nu_{D_{rt_i}} &= \phi\ Nu_{laminar,D_{rt_i}} + (1 - \phi)Nu_{turbulent,D_{rt_i}} \\
\phi &= 1.33 - \frac{Re_{D_{rt_i}}}{6000}
\end{aligned}
\tag{2.32}
$$

where Reynold's number is calculated using Equation 2.33.

$$
Re_{D_{rt_i}} = \frac{4\dot{m}_f}{\pi D_{rt_i}\mu_f} \tag{2.33}
$$

And the thermophysical properties of the heat transfer fluid, Syltherm 800, are found by the interpolation function in MATLAB using the manufacturer data [58]. The conductive heat transfer within the receiver tube is calculated by Fourier's law of conduction in cylindrical walls from Çengel Y. [59], and given by Equation 2.34,

$$
q_{cond,rt_i - rt_o} = \frac{2\pi k_{rt}(T_{rt_i} - T_{rt_o})}{\ln\left(\frac{D_{rt_o}}{D_{rt_i}}\right)}L \tag{2.34}
$$

where the thermal conductivity of the receiver tube made from SS 316L, $\mathrm{k_{rt}}$, is calculated using the correlation given in Kalogirou S. [56], which is given by Equation 2.35.

$$
k_{rt} = 0.013\frac{T_{rt_i} + T_{rt_o}}{2} + 15.2 \tag{2.35}
$$

The radiative heat transfer between the receiver tube and the glass envelope is estimated using Equation 2.36 [59], where ϵ_{rt_o} and ϵ_{ge_i} are the emissivities of the receiver tube coating and the glass envelope, respectively.

$$q_{rad,rt_o-ge_i} = \frac{\sigma\pi D_{rt_o}(T_{rt_o}^4 - T_{ge_i}^4)}{\left(\frac{1}{\epsilon_{rt_o}} + \left(\frac{(1-\epsilon_{ge_i})D_{rt_o}}{\epsilon_{ge_i}D_{ge_i}}\right)\right)}L \tag{2.36}$$

The conductive heat transfer within the glass envelope is calculated similarly to the receiver tube, using Equation 2.37,

$$q_{cond,ge_i-ge_o} = \frac{2\pi k_{ge}(T_{ge_i} - T_{ge_o})}{\ln\left(\frac{D_{ge_o}}{D_{ge_i}}\right)}L \tag{2.37}$$

where the thermal conductivity of the glass envelope, $\mathrm{k_{ge}}$, is $1.15\,\mathrm{Wm^{-1}K^{-1}}$ [60]. The convective heat transfer from the glass envelope to the ambient air is calculated using Newton's law of cooling, given by Equation 2.38,

$$q_{conv,ge_o-a} = h_{ge_o-a}\pi D_{ge_o}(T_{ge_o} - T_a)L \tag{2.38}$$

where the convective heat transfer coefficient is given by Equation 2.39.

$$h_{ge_o-a} = \frac{k_{air}}{D_{ge_o}}Nu_{D_{ge_o}} \tag{2.39}$$

The thermal conductivity of the air is calculated by the interpolation function in MATLAB using thermophysical property data from Incropera [61]. Assuming that there is no wind around the receiver due to its location in the collector, the Nusselt number is calculated using Equation 2.40 [59].

$$\overline{Nu}_{D_{ge_o}} = \left[0.60 + \frac{0.387Ra_{D_{ge_o}}^{1/6}}{\left(1 + (0.559/Pr_{ge_o-a})^{\frac{9}{16}}\right)^{\frac{8}{27}}}\right]^2 \tag{2.40}$$

where,

$$Ra_{D_{ge_o}} = \frac{g\beta\left(T_{ge_o} - T_a\right)D_{ge_o}^3}{\nu_{ge_o-a}^2}Pr_{ge_o-a} \tag{2.41}$$

and,

$$\beta = \frac{1}{T_{ge_o-a}}, \qquad Pr_{ge_o-a} = \frac{\nu_{ge_o-a}}{\alpha_{ge_o-a}}, \qquad T_{ge_o-a} = \frac{T_{ge_o} + T_a}{2} \tag{2.42}$$

And, if there is wind around the receiver, the Nusselt number for cross flow over a cylindrical surface is calculated by Equation 2.43, correlation suggested by Zukauskas, given in Incropera [61], valid for $0.7 \lesssim \mathrm{Pr} \lesssim 500$, and $1 \lesssim \mathrm{Re_D} \lesssim 10^6$.

$$\overline{Nu}_D = C Re_D^m Pr_{air}^n \left(\frac{Pr_{air}}{Pr_s} \right)^{1/4} \tag{2.43}$$

where, n is 0.37 for $\mathrm{Pr} \lesssim 10$, and n is 0.36 for the rest of the range, Reynold's number is calculated by Equation 2.44, and other constants are given in Table 2.1.

Table 2.1: Constants of Equation 2.43.

$\mathrm{Re_D}$	C	m
1 - 40	0.75	0.4
40 - 10^3	0.51	0.5
10^3 - 2 10^5	0.26	0.6
2 10^5 - 10^6	0.076	0.7

$$Re_D = \frac{V_{wind} D_{ge_o}}{\nu_{air}} \tag{2.44}$$

Finally, the radiative heat transfer coefficient is given by Equation 2.45 [59],

$$q_{rad,ge_o-s} = \sigma \epsilon_{ge_o} \pi D_{ge_o} (T_{ge_o}^4 - T_s^4) L \tag{2.45}$$

where $\mathrm{T_s} = \mathrm{T_a} - 8\ \mathrm{K}$. The emittance of the glass envelope, ϵ_{ge}, is taken as 0.86 [56], and the emittance of the receiver tube is calculated using Equation 2.46 [62].

$$\epsilon_{rt_o} = 3.27\ 10^{-4} T_{rt_o} - 6.5971\ 10^{-2} \tag{2.46}$$

CHAPTER 3

RAY-TRACING SIMULATIONS & INVESTIGATION OF THE THERMAL PERFORMANCE OF FRESNEL LENS SOLAR COLLECTOR

3.1 Verification of the Ray-tracing Model

In the verification simulations, the wavelength of the rays is selected as 800 nm, and the polycarbonate's respective refractive index is found as 1.58, from the data published by Zhang et al. [41] [42]. Both of these are given as material and ray-related properties to both simulation environments. By selecting a single wavelength, the effects of chromatic aberration are eliminated from the verification study. Similarly, the effects of comatic aberration are also eliminated from the verification study by selecting the angle between the ray and the normal vector of the aperture as zero. Additional simulations for determining the correctness of the wavelength-dependent calculation are considered a repetitive and unnecessary step since the additional step is only a data interpolation regarding the refractive index. Also, investigating the comatic aberration in the verification study is considered to be a repetitive and unnecessary step because those angles and the refractions are encountered.

In the ray-tracing code for the verification study, the internal loss due to the absorption within the medium and the Fresnel reflections are neglected to obtain ray-related data, as much as possible, hence the spot diameter at the control surfaces is selected as the verification parameter.

To verify the correctness of the refraction calculations in the ray-tracing simulations, two biconvex lenses and two plano-convex lenses are selected. The properties of these lenses are given as input to a new geometry creation code, and they are drawn in the *GMSH* environment through programming in *Julia*. Additional control surfaces are

added to these lenses illustrated in Figure 2.15 and the environments for the verification simulations, ray-tracing code, and *Zemax OpticStudio* [63], and the sample results are given in Figure 3.1.

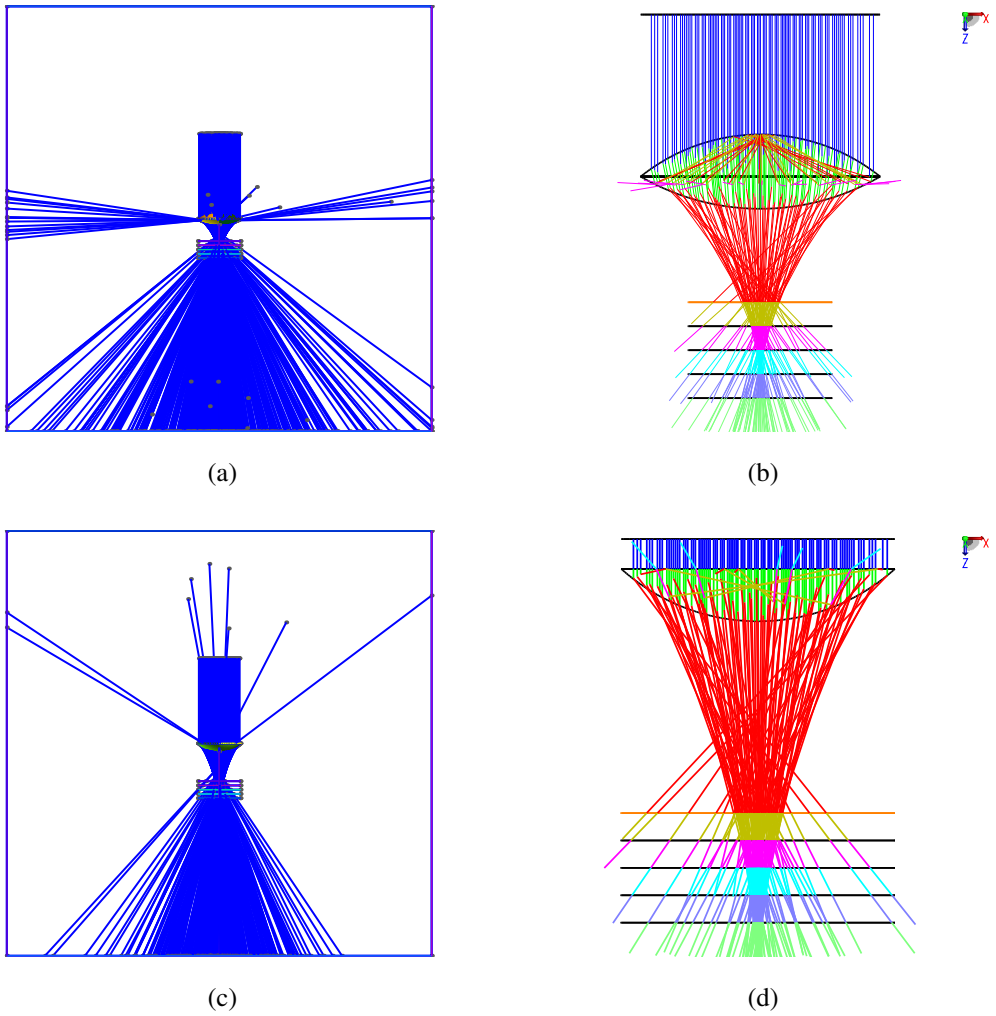

Figure 3.1: Lens types used in the verification study of the ray-tracing simulations. *(a) Biconvex lens (Code), (b) Biconvex lens (Zemax), (c) Planar-convex lens (Code), (d) Planar-convex lens (Zemax).*

In notation with Equation 2.21, two biconvex lenses, R1 = 800 mm and 1000 mm, R2 = 1000 mm and 800 mm, respectively, and similarly, in notation with Equation 2.22, two planar-convex lenses, R2 = 750 mm and 1500 mm, respectively, are generated. For each simulation, five different distances are selected for the control surfaces. The results of this study are presented between Figures 3.2 and 3.5.

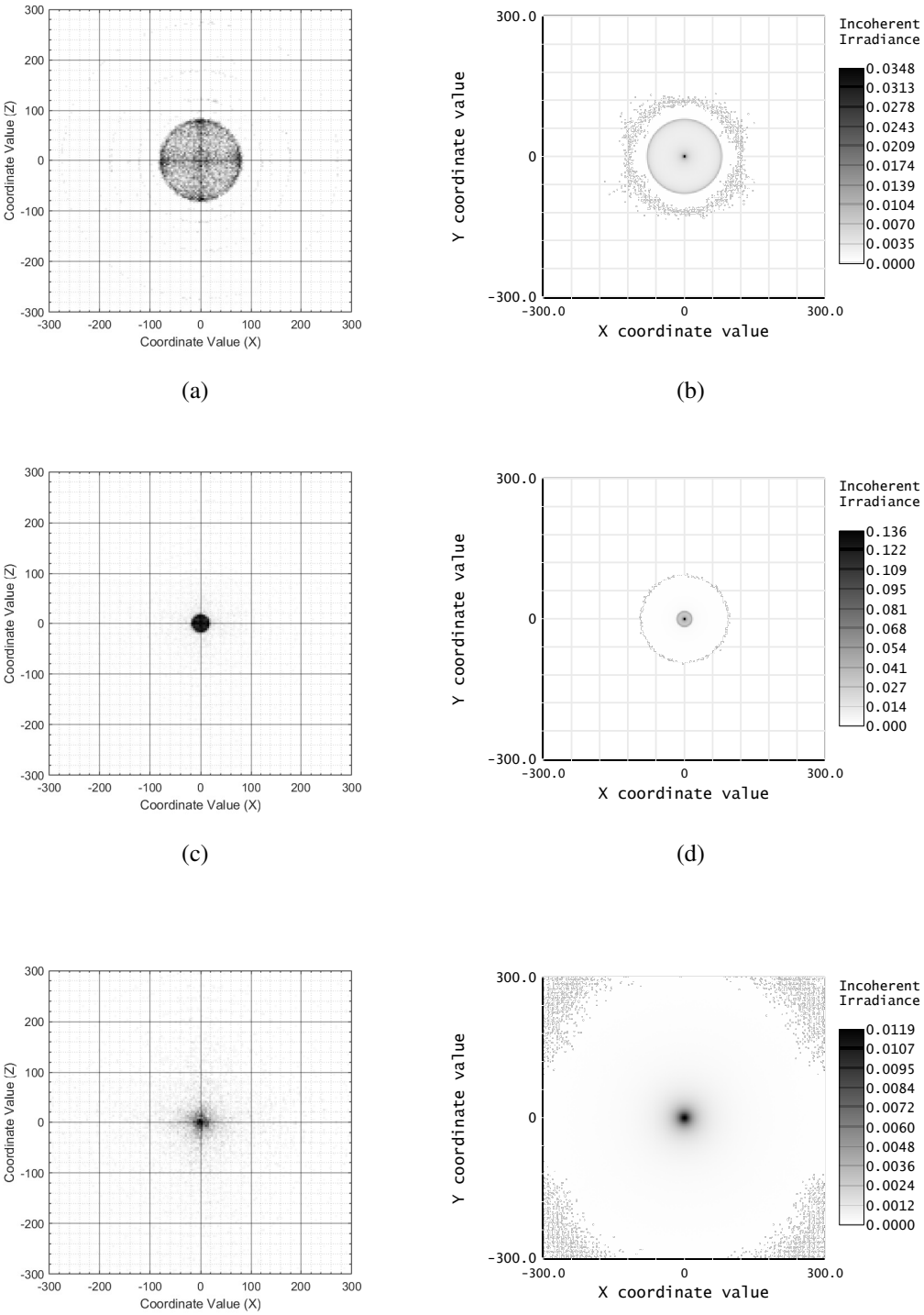

Figure 3.2: Ray number and incoherent irradiance distributions for the biconvex lens, R1 = 800mm, and R2 = 1000mm. *(a,c,e) Ray-tracing code, (b,d,f) Zemax.*

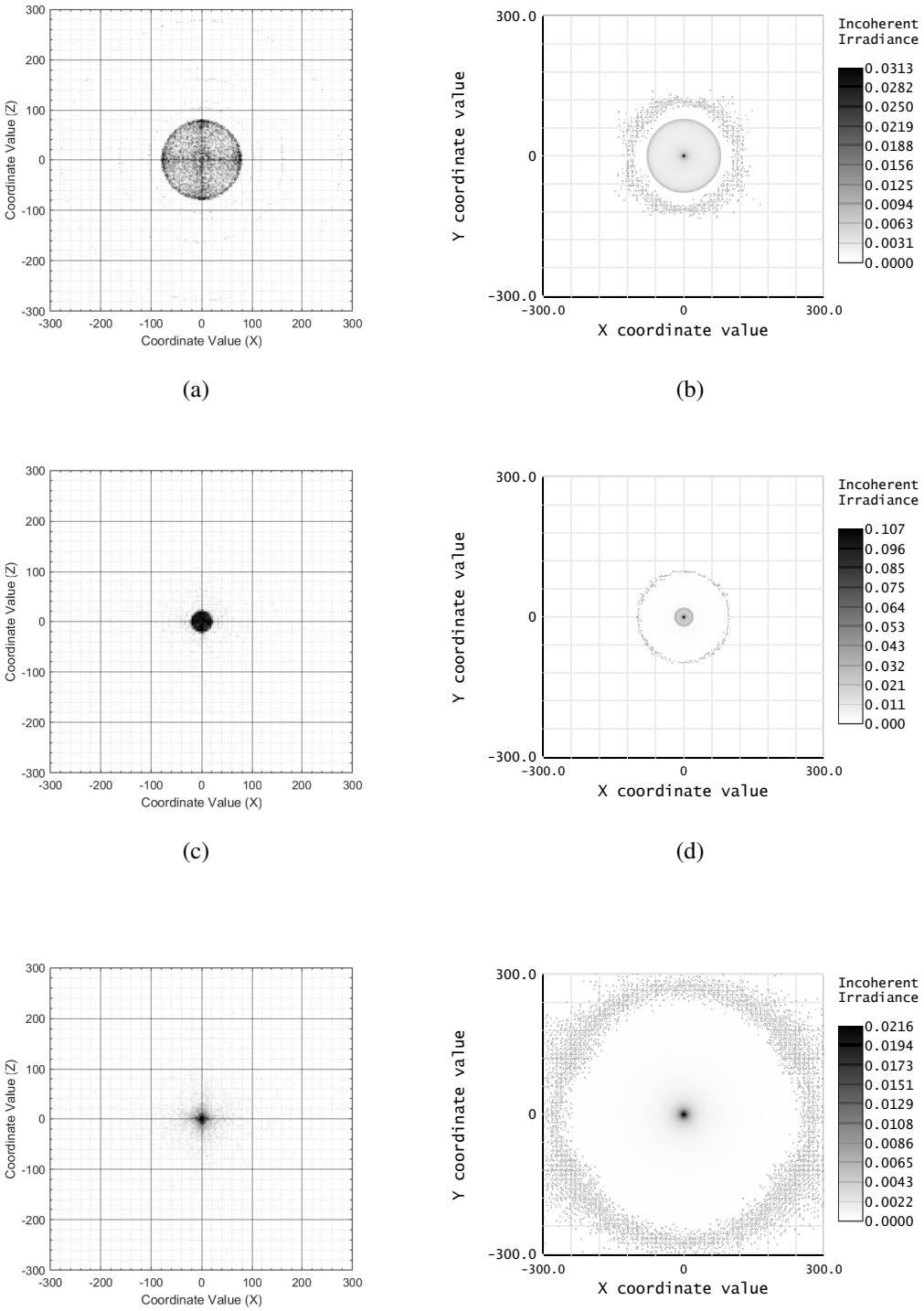

Figure 3.3: Ray number and incoherent irradiance distributions for the biconvex lens, R1 = 1000mm, and R2 = 800mm. *(a,c,e) Ray-tracing code, (b,d,f) Zemax.*

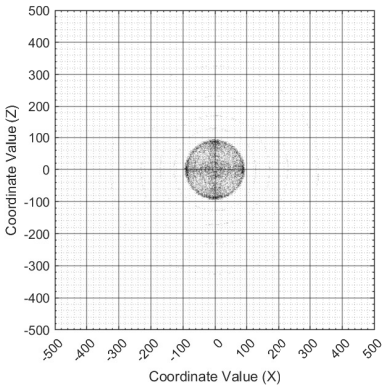

(a)

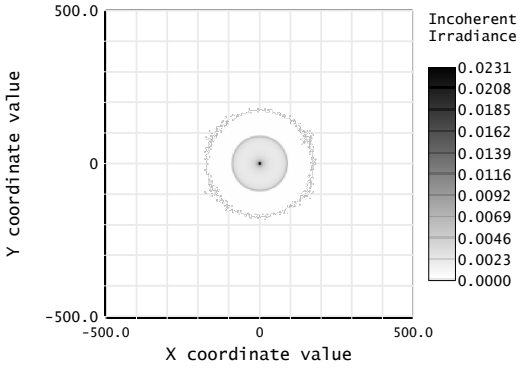

(b)

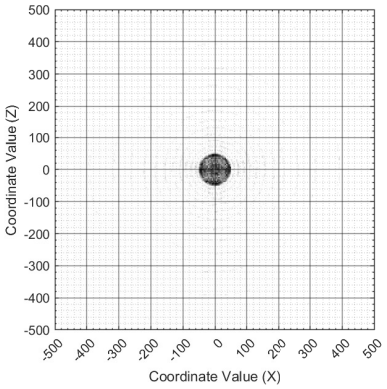

(c)

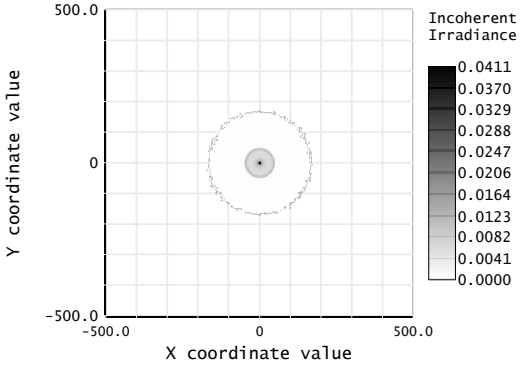

(d)

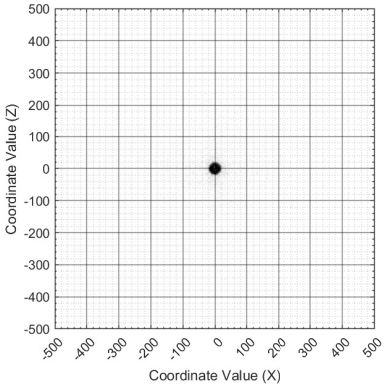

(e)

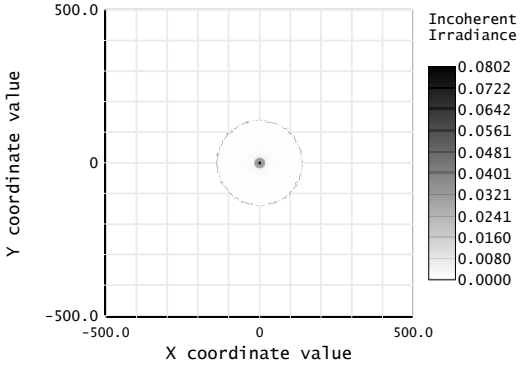

(f)

Figure 3.4: Ray number and incoherent irradiance distributions for the planar-convex lens, R2 = 750mm. *(a,c,e) Ray-tracing code, (b,d,f) Zemax.*

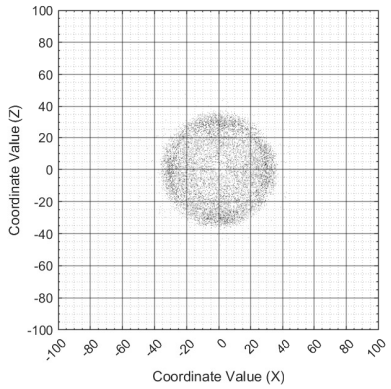

(a)

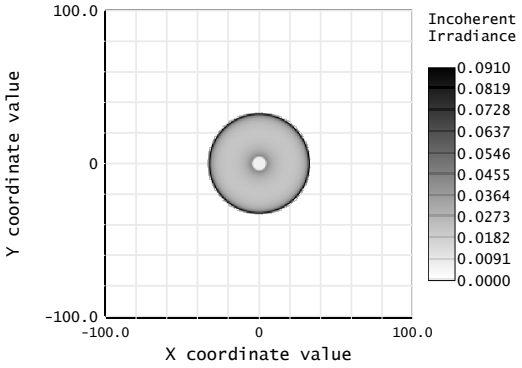

(b)

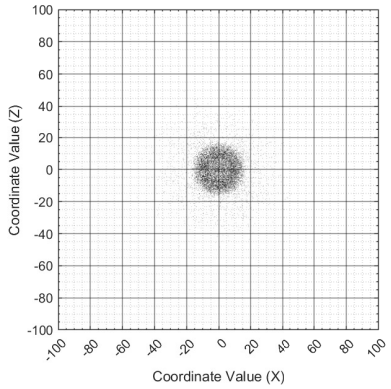

(c)

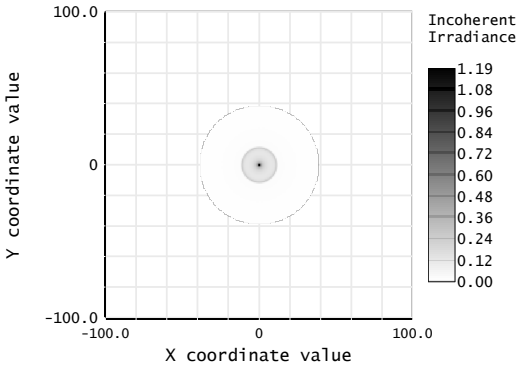

(d)

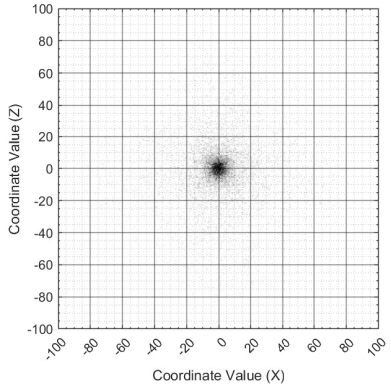

(e)

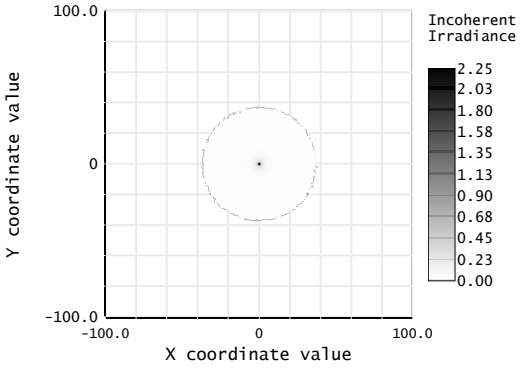

(f)

Figure 3.5: Ray number and incoherent irradiance distributions for the planar-convex lens, R2 = 1500mm. *(a,c,e) Ray-tracing code, (b,d,f) Zemax.*

3.2 Parametric Study on Optimal Geometry Parameters

To determine the optimal geometry, which should have high transmittance and focus the incident rays to the receiver, to be used in the simulations, an initial study on a set of parameters is conducted. These parameters, illustrated in Figure 3.6, include minimum and maximum height, and the latter limiting value for the width, which delays the narrowing, of the prism. The results of the initial study using the set parameters are given in Figure 3.7.

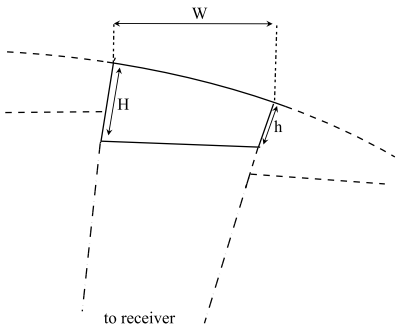

Figure 3.6: Parameters used in the parametric study for optimal geometry creation.

The radius of the lens is selected as 1000 mm, and the results for the initial study, whose sample size for each simulation is 10^4, given in Figure 3.7, indicate that increasing the minimum and the maximum height of the prism has a reducing effect on the efficiency, and the latter limiting value for the width of the prism has no significant effect on the efficiency. The efficiency in terms of energy of the solar collector is not the only parameter that needs to be examined during the lens creation procedure, because the unfavorable combinations of the heights of the prism may result in inadmissible lens geometries in terms of both the prism shape and the aperture width, observed in the sudden drop at the right side of Figure 3.7.

Complying with the results of this study, the minimum and the maximum height and the latter limiting value for the width of the prism are selected as 2 mm, 7 mm, and 10 mm, respectively, using a lens with a radius of 1000 mm. This combination of parameters resulted in 39.5% optical efficiency with a geometric concentration ratio of 14.43 using a receiver diameter of 70 mm. Moreover, in this preliminary study with a sample size of 10^4, the factors that cause loss mentioned in Chapter 2, have been included.

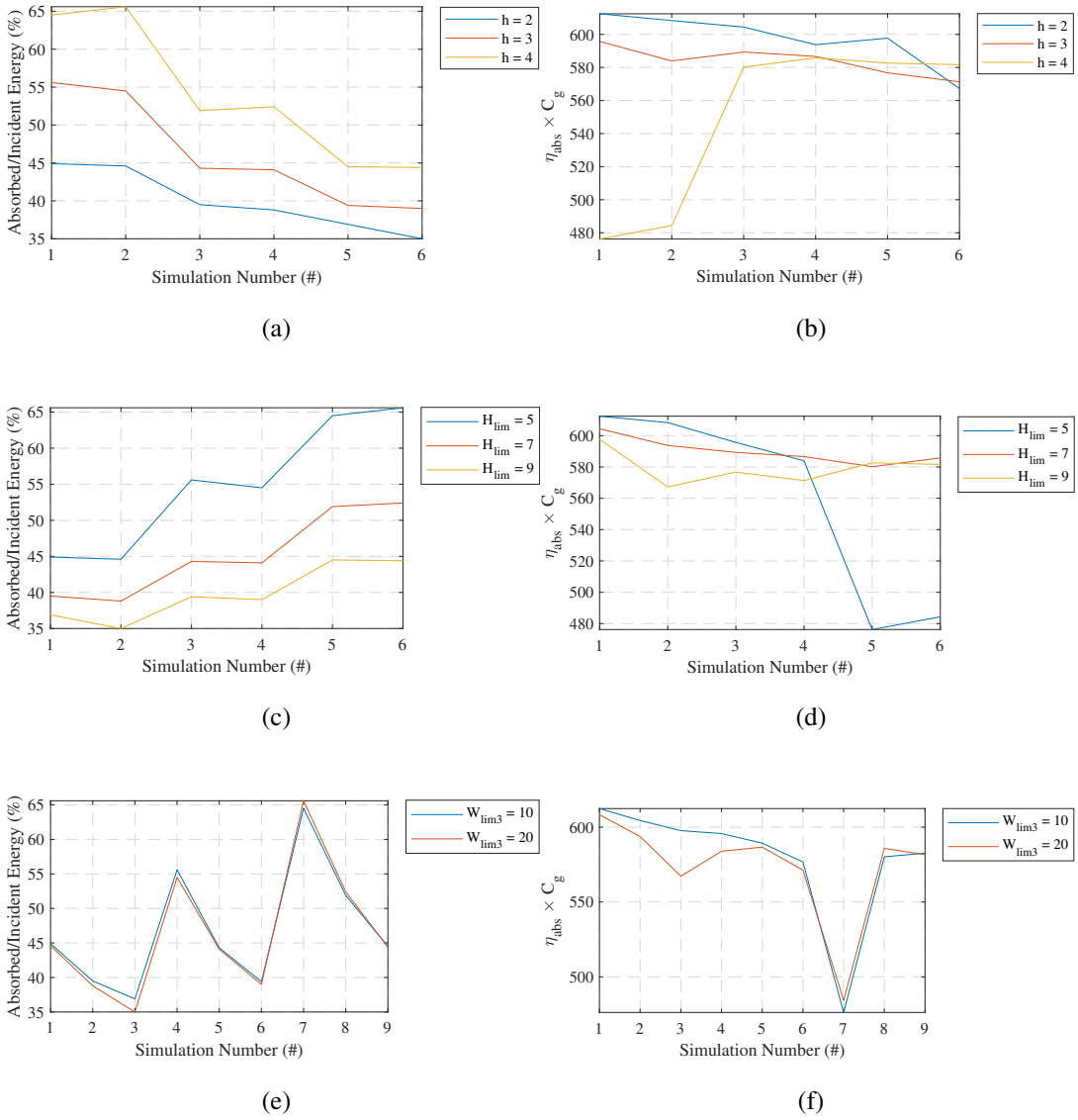

Figure 3.7: The solar-to-receiver efficiency, *left*, and the product of the solar-to-receiver efficiency and the geometrical concentration ratio, *right*. *(a,b) Minimum starting height, (c,d) maximum height, and (e,f) the latter limiting width value.*

An additional parametric search is conducted for the secondary concentrator, in this case, a cylindrical reflector, to catch the light escaping the receiver. Its radius and location of its origin with respect to the receiver, which are illustrated in Figure 3.8, are examined and the results are given in Table 3.1.

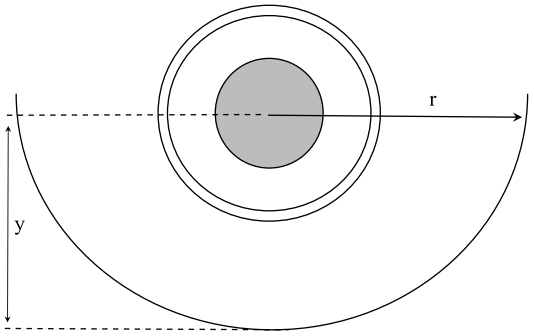

Figure 3.8: Illustration of the parameters studied for the secondary concentrator.

The results indicate that as the radius of the reflector surface increases, the light that it collects increases, and as the center of this half-cylindrical reflective surface increases, meaning that the surface gets closer to the receiver, the efficiency of the solar collector increases. Considering the results given in Table 3.1, the radius of the secondary is selected as 155mm and its center is 40 mm above the receiver's center.

The efficiency terms presented in these results are η_{opt}, which is the percentage of absorbed energy to the incident energy, and η_{int}, which is the percentage of the number of the rays absorbed to the ray sample size.

Table 3.1: Results of the parametric study on the secondary concentrator surface's radius and placement.

r_{ref} (mm)	y_{shift} (mm)	η_{opt} (%)	η_{int}* (%)	Other Surf. Abs. (%)	Internal Abs. (%)	Lost (%)
135	0	40.5	34.2	1.3	34.1	30.3
145	0	39.9	33.8	1.6	34.4	30.3
155	0	38.9	32.9	1.5	35.1	30.5
135	10	42.1	35.4	1.3	35	28.3
145	10	41.3	34.5	1.5	35.5	28.5
155	10	42.6	36.1	1.6	34.1	28.1
135	20	44.4	37.4	1.2	34.5	26.9
145	20	44.0	36.9	1.4	34.9	26.9
155	20	44.3	36.8	1.5	35.2	26.5
135	40	49.0	40.8	1.4	34.8	23.0
145	40	49.5	41.4	1.5	34.4	22.8
155	40	49.5	40.9	1.5	35.1	22.4

* The intersection efficiency of the lens is for the band between 400 nm to 4 μm.

3.3 Surface Approximation and Sample Size Independence Study

The environment for the simulation is made up of several components: a lens, a receiver, a mirror, a source plane, a control surface, and a bounding box. These components are illustrated in Figure 3.9. The previous analysis determines the lens's dimensions, and the position and dimensions of the source plane change according to the lens and the starting angles of the rays. The receiver is positioned at the center of the outer surface of the lens, and the mirror is placed according to Table 3.1. The bounding box is a three-dimensional space large enough to contain the subject of interest and not affect the results. The control surface is a two-dimensional plane that lies between the bounds of the bounding box, and intersections on it do not count as an event intersection.

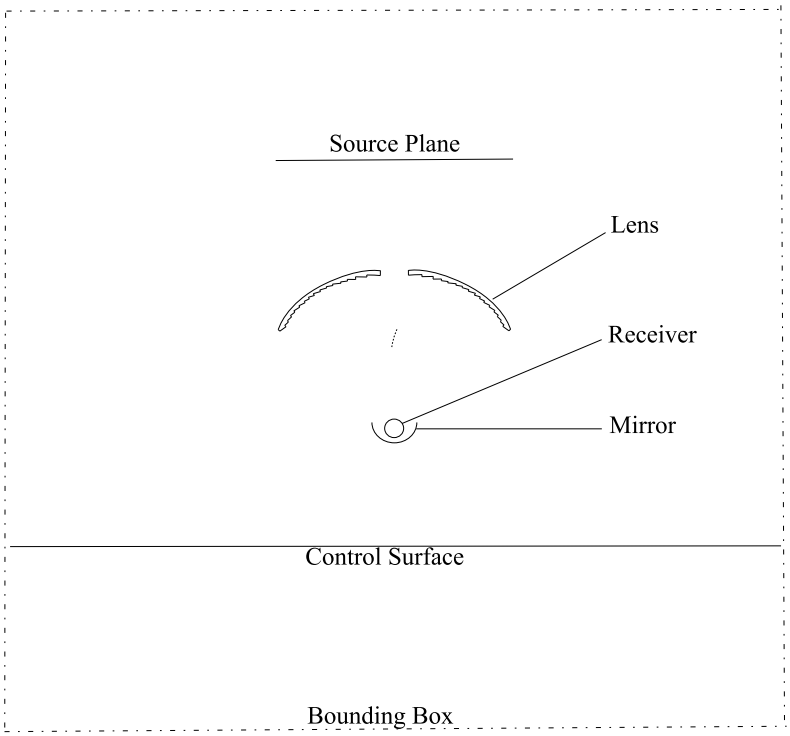

Figure 3.9: Simulation environment of the Fresnel lens solar collector.

3.3.1 Surface Approximation Independence Study

To account for the effect of the segment size of the approximation in the ray-tracing simulations, a study is conducted on the number of divisions on the circular surfaces, that are divided into quadrilateral segments. In this study, for not accounting for the variation due to light spectrum, the wavelength of the rays is selected as 800 nm, which results in an increase in the optical efficiency by roughly 15%. The division numbers are selected as 50, 100, 200, 400, and 800, and for the result parameter, optical efficiency is examined. In Figure 3.10, the results of the simulation which presents the mean and standard deviation of the efficiency and the respective simulation speeds are given. The sample size of these simulations is 10^4, and the total number of 17 simulations are conducted for each parameter.

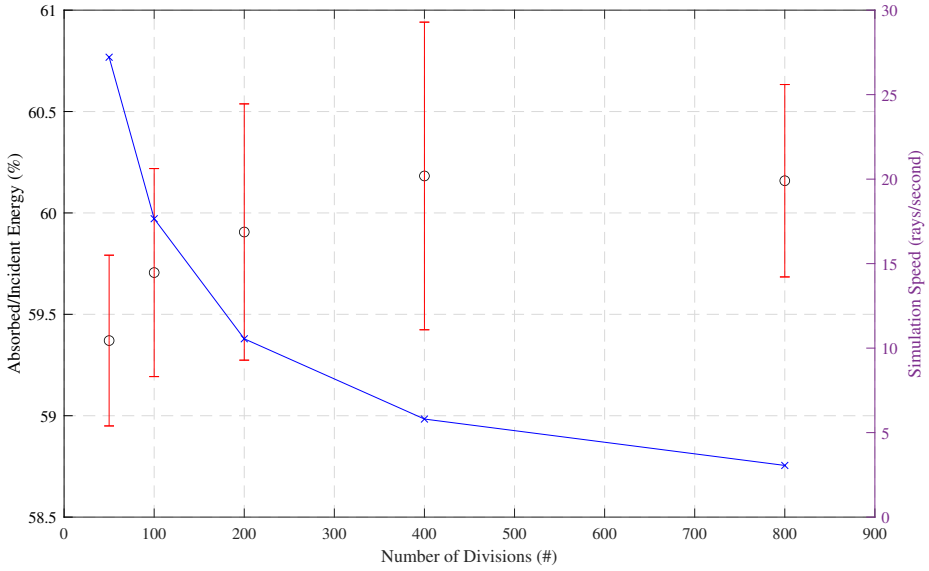

Figure 3.10: Results of the surface approximation independence study.

Due to the small sample size and the total number of simulations, the standard deviation calculated for each step is larger than expected. Increasing the sample size to the order of 10^6 and increasing the simulation number should mitigate this issue. Considering the computational time for the simulations, approximating the circular surfaces with 200 divisions, in which the simulation speed eventuates to roughly 10 rays per second is decided to be an adequate selection.

3.3.2 Sample Size Independence Study

To find the sample size of rays that should be emitted to the collector, different sample sizes and their resulting optical and intersection efficiencies are compared. A simulation with the ray sample size of 10^7 is performed and the smaller studies are calculated by undersampling the original data. The repetition numbers are selected as 100 for the undersampled smaller ray sample sizes. These results are given in Table 3.2.

Table 3.2: Results of the sample size independence study, conducted with varying ray sample sizes and repetitions on a lens with 1 m^2 aperture area at the condition of perpendicular ray-lens alignment.

N_{ray}	$\overline{\eta_{opt}}$ (%)	$\overline{\eta_{int}}^{*}$ (%)	$N_{repetition}{}^{**}$	$\sigma_{\eta_{opt}}$	$\sigma_{\eta_{int}}$
10^4	49.56	41.31	100	0.60	0.44
10^5	49.58	41.34	100	0.18	0.16
10^6	49.57	41.34	100	0.05	0.05
10^7	49.57	41.34	1	-	-

* The intersection efficiency of the lens is for the band between 400 nm to 4 μm.
** Smaller sample sizes are acquired by splitting the study with a sample size of 10^7 in an arbitrary manner.

The standard deviations of the efficiencies, which are given in Table 3.2, show that the standard deviation is expectedly decreasing as the ray sample size is increasing. Considering the results, a sample size of 10^6 per square meter aperture area is a suitable choice. Additionally, the last two columns for the sample size of 10^4 show that the deviation illustrated in Figure 3.10 is likely to be associated with the sample size.

Finally, another effect of the sample size is on the spectrum of the emitted rays. As the sample size increases, it is expected that the wavelengths assigned to the rays would fill the spectrum according to the rule of the *cumulative distribution function*. For examining the effect of the sample size on the emitted rays' spectrum, assigned wavelengths and their *cumulative distribution function* for two sets, whose sample sizes are 10^6 and 10^7 are plotted over Figure 2.2, and given in Figure 3.11.

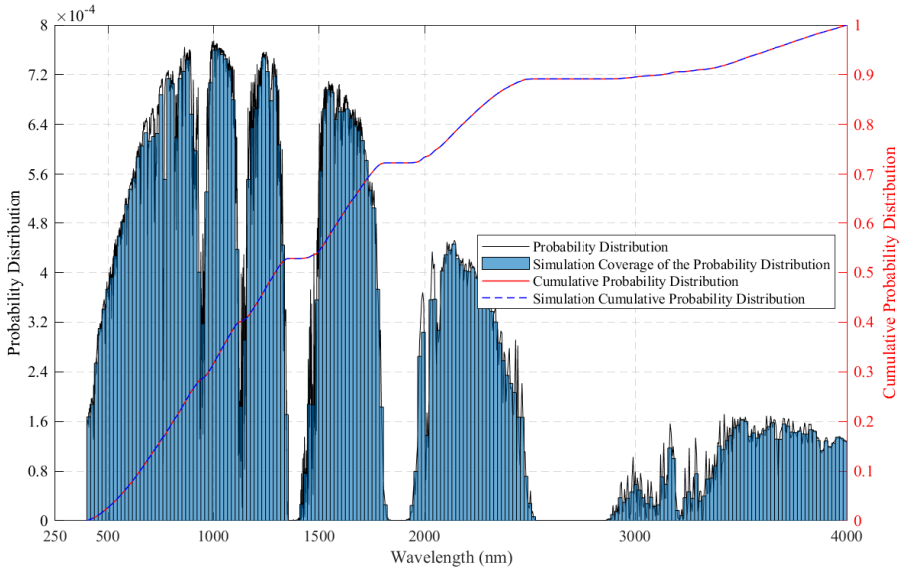

(a)

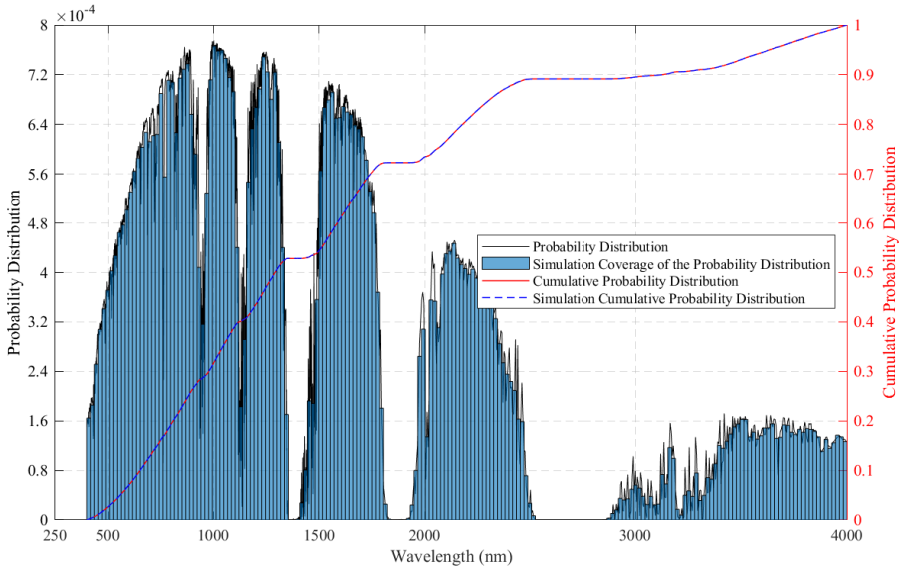

(b)

Figure 3.11: Simulation coverage of the AM1.5 spectrum for the simulation with the ray sample sizes of *(a)* 10^7, *and (b)* 10^6.

Figure 3.11 and Table 3.2 indicate that the ray wavelength distribution under the rule of *cumulative distribution function* matches AM1.5 spectrum. Therefore, it can be said that the ray sample size of 10^6 per square meter is appropriate.

3.4 Model Parameters

The parameters required for further simulations to determine the collector's optical performance are presented in Table 3.3. The parameters for the receiver are acquired from SNL's technical report [64]. The minimum and the maximum thicknesses and the parameters for the reflector are acquired using the parametric study. The aperture width of the lens and the geometrical concentration ratio are obtained from the developed geometry creation code. Moreover, to lessen the effect of the incidence angle around the transversal axis, the array length is chosen as 4 meters.

Table 3.3: Parameters used in the ray-tracing simulations.

Part Name	**Parameter Name**	**Parameter Value/Type**
Solar Collector	Array Length	4 m
	Aperture Area	4.04 m^2
	Geometrical Concentration Ratio	14.43
Lens	Outer Radius	1000 mm
	Minimum Thickness	2 mm
	Maximum Thickness	7 mm
	Total Aperture Width	1010 mm
	Single Lens Volume	2.23 10^{-3} m^3
	Total Lens Volume	8.91 10^{-3} m^3
	Material	Polycarbonate
Receiver [64]	Envelope Outer Diameter	115 mm
	Envelope Thickness	3 mm
	Absorber Outer Diameter	70 mm
	Absorber Thickness	2 mm
	Envelope Material	Low-Iron Borosilicate
	Absorber Material	Stainless Steel 316L
	Absorber Coating	Cermet
	Absorptance*	0.95
Reflector	Radius	155 mm
	Location of Center	(0, 40 mm, 0 : 4 m)
	Reflectance	0.94

Absorptance of the Cermet coating is corrected for the ray-tracing simulation using Equation 3.1, from Duffie J. and Beckman W. [65], where θ is the angle of incidence of the coated receiver tube.

$$\begin{aligned}\frac{\alpha_\theta}{\alpha_n} =& 1 - 1.5879\ \ 10^{-3}\theta + 2.7314\ \ 10^{-4}\theta^2 - 2.3026\ \ 10^{-5}\theta^3 \\ &+ 9.0244\ \ 10^{-7}\theta^4 - 1.8000\ \ 10^{-8}\theta^5 + 1.7734\ \ 10^{-10}\theta^6 \\ &- 6.9937\ \ 10^{-13}\theta^7\end{aligned} \tag{3.1}$$

3.5 Optical Performance of the Fresnel Lens Solar Collector

For evaluating the optical performance of the Fresnel lens solar collector, multiple simulations have been performed using the developed ray tracing code. For these simulations, the parameter set, which is given in Table 3.3, is used. The isometric view of the simulation geometry, drawn in the *GMSH* environment is given in Figure 3.12.

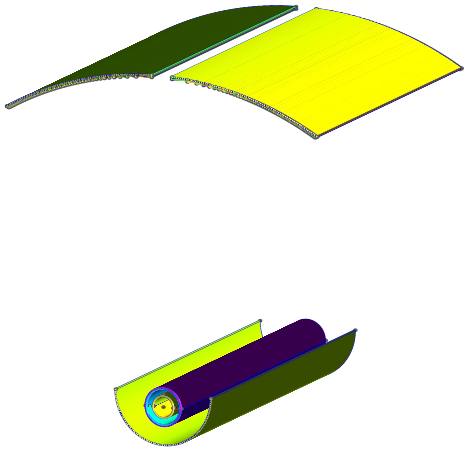

Figure 3.12: Isometric view of the Fresnel lens solar collector simulation geometry in the *GMSH* environment.

Using the simulation results from Section 3.3.2, Figures 3.13 and 3.14 have been created. While Figure 3.13(a) uses the result with a sample size of 10^6, Figure 3.13(b) uses the result with a sample size of 10^7, which induces the apparent difference in clearness. As it can be seen from both figures, Figures 3.13 and 3.14, the main focus on the receiver is located around $\phi_{rec} = \frac{\pi}{2}$, and there are two smaller focuses under the receiver, originating from the secondary concentrator surface. Furthermore, as given in Figure 3.14, the local concentration ratio on the receiver, calculated by Equation 3.1, reaches its maximum at $\phi_{rec} = \frac{\pi}{2}$ with a value of 16.

$$LCR = \frac{q_{local}}{G_{beam}} \tag{3.2}$$

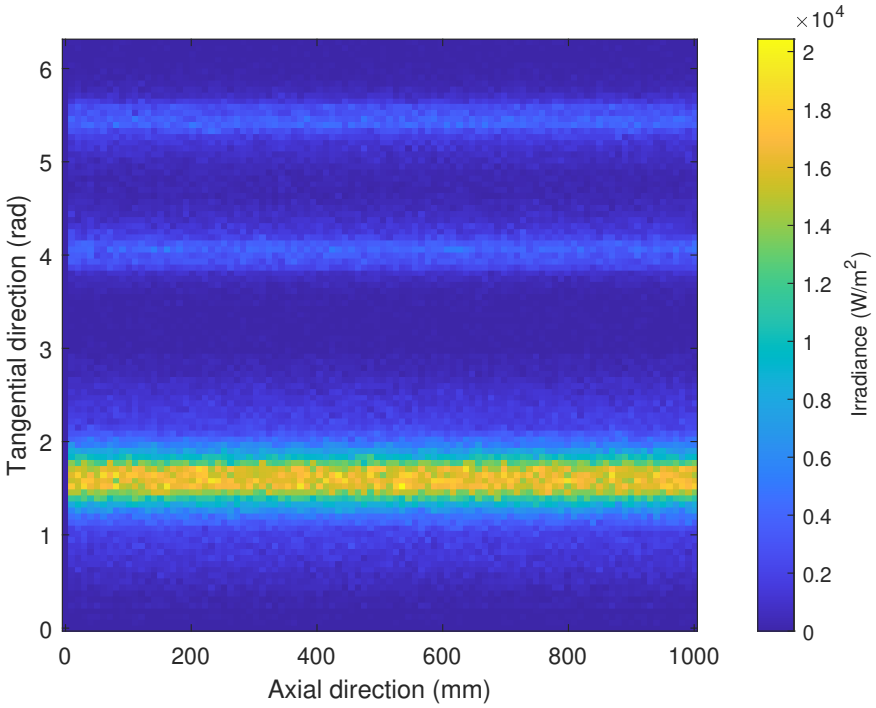

(a)

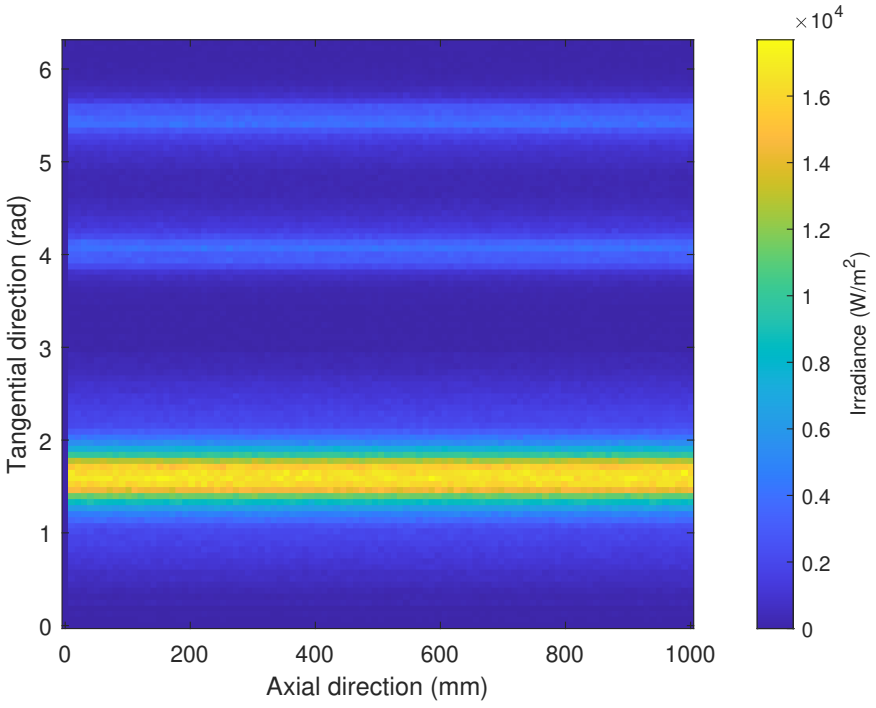

(b)

Figure 3.13: Absorbed irradiances on the receiver surface for the runs with the determined parameters and the ray sample sizes of *(a)* 10^6, and *(b)* 10^7, on a Fresnel lens solar collector with 1 m^2 aperture area at the condition of perpendicular ray-lens alignment.

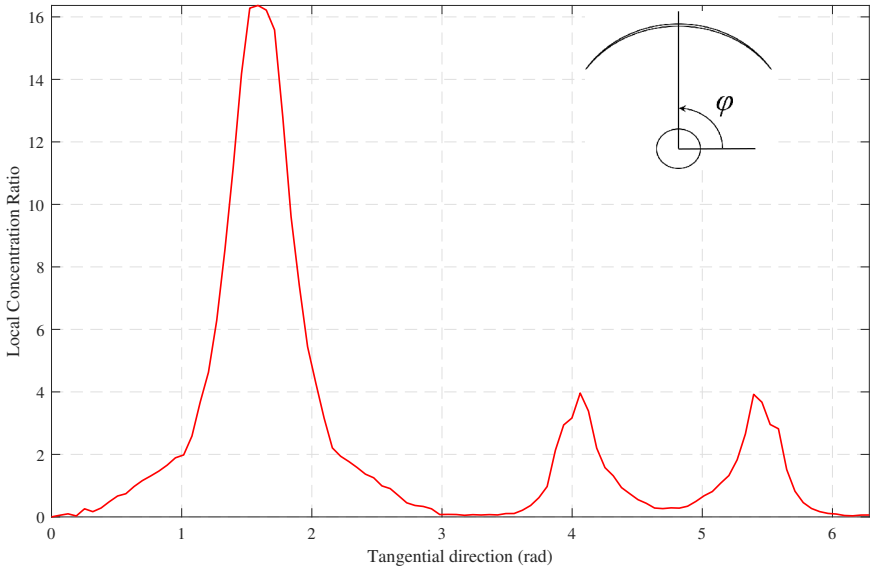

Figure 3.14: Local concentration ratio on the receiver.

For determining the efficiency of the collector when the rays are incoming from Sun at an angle, a factor called incidence angle modifier should be calculated. Moreover, the efficiency of the collector for increasing incidence angles is simulated with a collector length of 4 meters, and the results are given in Table 3.4. As determined in Sections 3.3.1 and 3.3.2, division number of 200 for the cylindrical surfaces, and a sample size of 10^6 per square meter is used. Additionally, internal absorption in column 3 is coherent with the 81.6% real transmittance obtained by Ma et al. [34].

Table 3.4: Energetic and quantitative outcomes of the rays for different angles of incidence, with sample size 4 10^6, which is for a collector length of 4 meters.

$\boldsymbol{\theta}$ (deg)	$\mathbf{E_{abs,\,rec}}$ (%)	$\mathbf{E_{abs,\,tra}}$ (%)	$\mathbf{E_{lost}}$ (%)	$\mathbf{N_{abs,\,rec}}$ (%)	$\mathbf{N_{abs,\,tra}}$ (%)	$\mathbf{N_{lost}}$ (%)
0	49.51	20.00	30.50	41.29	34.82	23.90
10	45.18	19.77	35.05	37.75	34.53	27.72
15	41.37	19.60	39.03	34.63	34.32	31.04
30	25.56	18.97	55.47	21.62	33.64	44.74
45	10.42	20.70	68.88	9.10	34.91	55.98
50	8.45	18.67	72.88	7.23	33.23	59.54
60	4.23	18.80	76.96	3.85	33.29	62.86
65	2.23	18.47	79.30	2.11	32.87	65.03

"E" stands for energy, and "N" stands for number.

In Figure 3.15, sample simulation results for the simulations for incidence angles of 0° and 30° are illustrated using 500 rays. Considering the results in Table 3.4 and Figure 3.15, it can be said that as the incidence angle increases, the Fresnel reflectance due to intersection and internal absorptance increases due to the longer path of the ray, causing a steeper decrease in the efficiency.

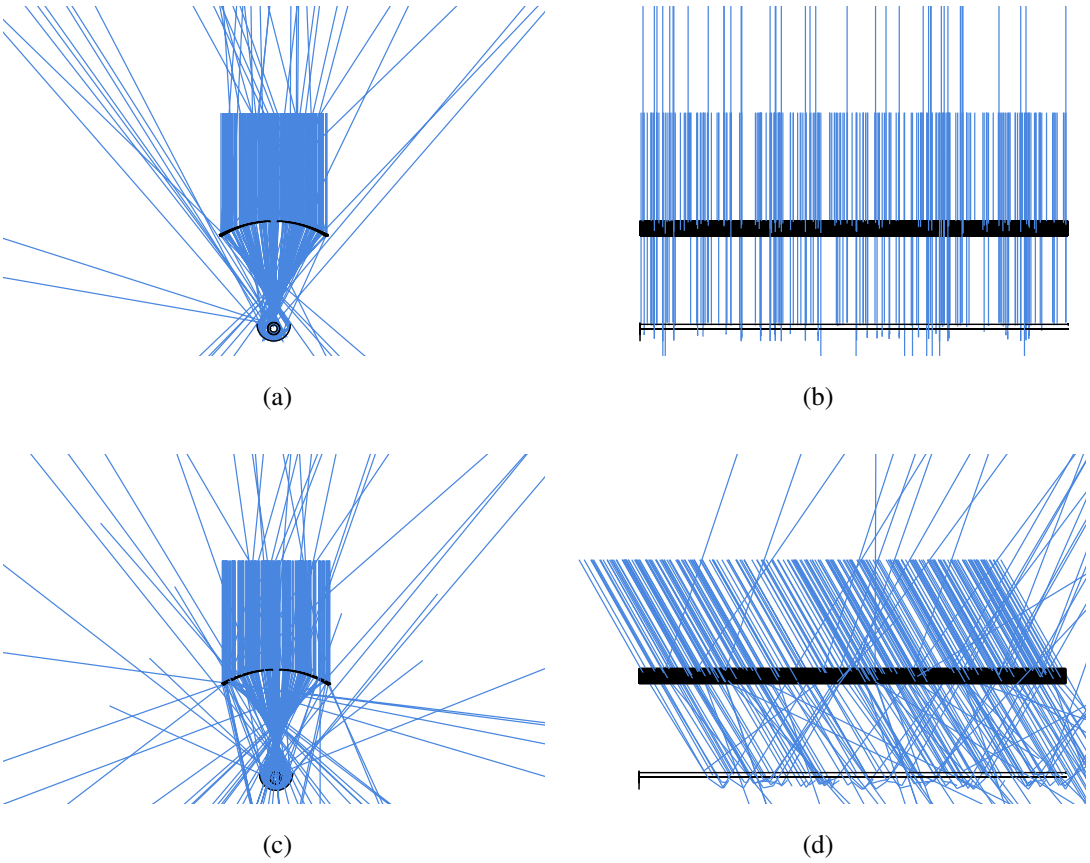

Figure 3.15: Simulation results illustrated using 500 rays in the *GMSH* environment, for *(a,b) 0° angle of incidence*, and *(c,d) 30° angle of incidence*.

Using the second column of Table 3.4, the incidence angle modifier is determined and presented in Figure 3.16. The incidence angle modifier has a sharp decrease between 0° and 15° , and soft landing after 60, unlike incidence angle modifiers for parabolic trough collectors. However, this result is similar to the study by Lin et al. [66] on a linear Fresnel lens solar collector.

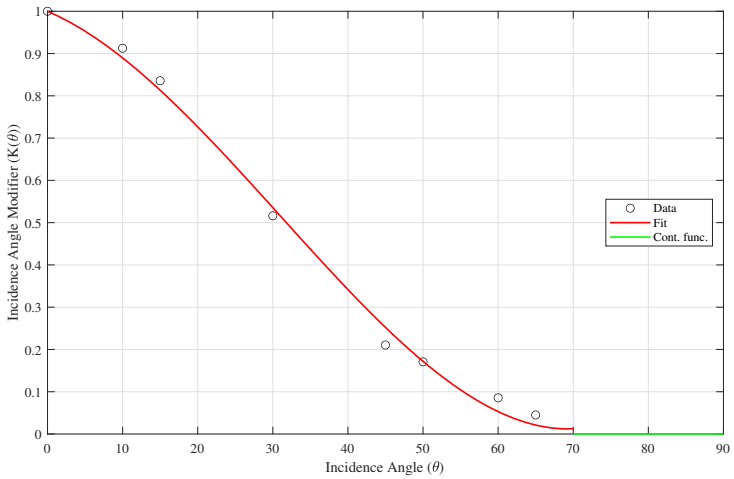

Figure 3.16: Incidence angle modifier for incidence angles around transversal axis.

The fit equation is in the form of Equation 3.3.

$$\begin{aligned} K(\theta) &= 3.889\ \ 10^{-6}\theta^3 - 2.311\ \ 10^{-4}\theta^2 - 7.587\ \ 10^{-3}\theta + cos(\theta\frac{\pi}{180}) && \text{for } 0 < \theta < 70 \\ &= 0 && \text{for } 70 < \theta < 90 \end{aligned} \tag{3.3}$$

And in Figure 3.17, the effect of incidence angle around longitudinal axis on the optical efficiency is presented. A longitudinal incidence angle greater than zero indicates that the collector is not pointed directly at the target, and is caused by installation and tracking errors. Therefore, Figure 3.17 indicates that the acceptance angle of this collector is 6°, and the one dimensional tracking errors, which is given in the literature is lower than ±0.2° and ±0.4° as stated by Sallaberry et al. [67] and [68], indicate that the tracking errors would not likely to have a noticeable impact on the efficiency.

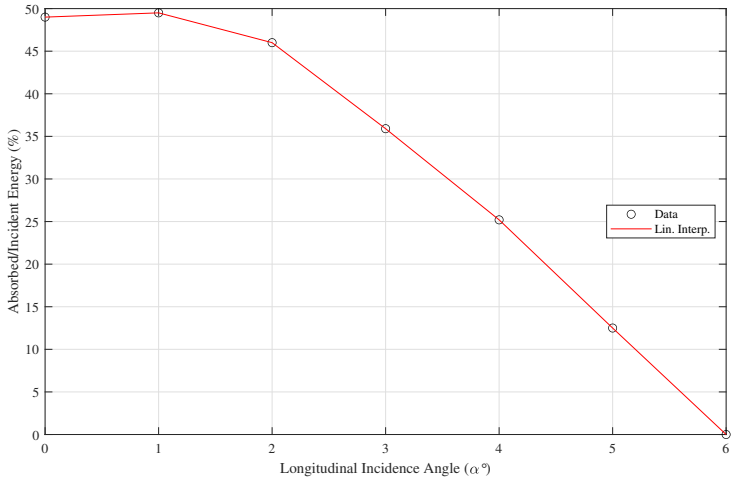

Figure 3.17: Optical efficiency for incidence angles around longitudinal axis.

3.6 Thermal Performance of the Fresnel Lens Solar Collector

The results of the one-dimensional thermal resistance model described in Section 2.7 are given in Tables 3.5 and 3.6. In comparison with the receiver heat loss results from SNL [64]. In Table 3.5, heat losses from the receiver under "no sun" and "no wind" conditions, and in Table 3.6, heat losses from the receiver under no wind conditions have been studied. The "no sun" condition refers to zero insolation on the collector, and the "no wind" condition refers to a set cross wind over the receiver.

Table 3.5: Heat loss results for SEGS L2 collector under no sun and no wind conditions for various air, and fluid temperatures.

T_a (°C)	T_f (°C)	$Q_{loss,conv}$ (1D) (W/m)	$Q_{loss,rad}$ (1D) (W/m)	Q_{loss} (1D) (W/m)	Q_{loss} (SNL [64]) (W/m)
17.00	47.00	-0.16	1.85	1.69	2
19.00	97.00	-0.03	7.81	7.78	8
24.00	147.00	0.11	20.21	20.33	21
30.00	197.00	0.64	41.81	42.45	44
40.00	246.00	1.29	75.97	77.26	82
52.00	296.00	2.40	128.38	130.79	141
69.00	345.00	3.40	202.42	205.83	225
89.00	394.00	4.47	303.79	308.25	344

Table 3.6: Heat loss results for SEGS L2 collector under no sun condition for various wind speeds, air, and fluid temperatures.

T_a (°C)	T_f (°C)	V_{wind} (m/s)	Q_{lc} (1D) (W/m^2)	Q_{lr} (1D) (W/m^2)	Q_{loss} (1D) (W/m^2)	Q_{loss} (SNL [64]) (W/m^2)
26.30	111.78	3.2	-0.76	2.73	1.97	0.3
25.40	100.00	2.9	-1.10	2.60	1.51	0.9
22.50	199.20	0.1	2.09	6.76	8.85	14.4
26.70	298.45	2.0	18.81	9.29	28.09	36.7
19.90	153.35	1.1	1.31	3.29	4.60	5.3
24.20	253.45	1.5	10.55	6.91	17.45	23.4
27.60	347.45	0.6	23.22	20.66	43.88	55.8

Moreover, using the thermal model, heat losses for different DNI values, which are 500, 750, and 1000 W/m^2, and different fluid temperatures at 0° incidence angle, and 25 °C air temperature are calculated. These results are given in Figure 3.18.

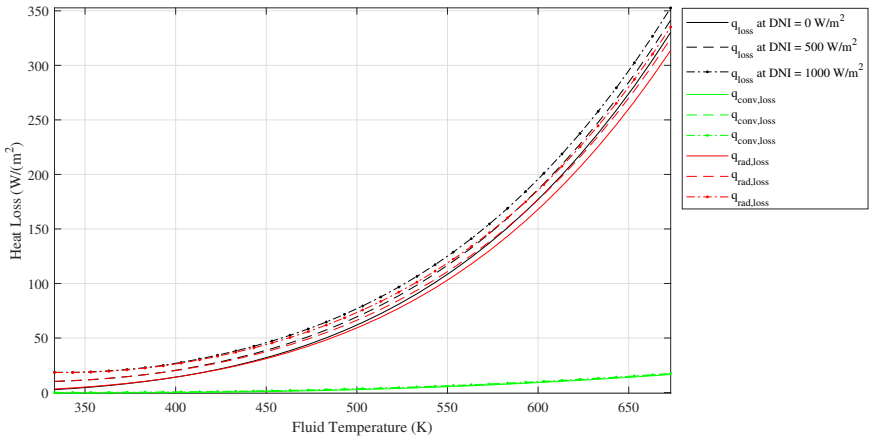

(a) $V_{wind} = 0m/s$

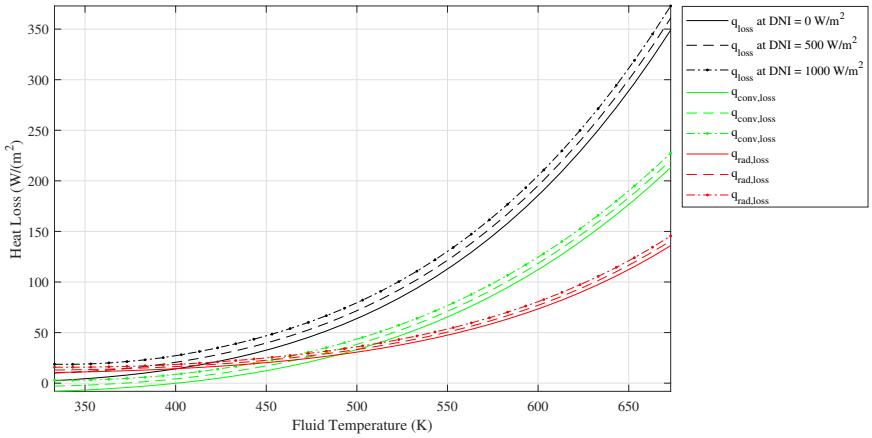

(b) $V_{wind} = 1m/s$

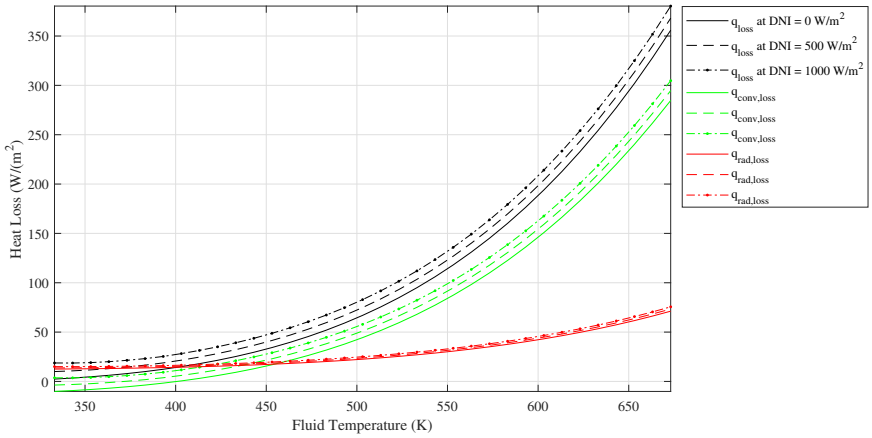

(c) $V_{wind} = 5m/s$

Figure 3.18: Heat loss per square meter aperture for different DNI values, and different working fluid temperatures 0° incidence angle, 25 °C air temperature, flow rate of 1 kg/s, and wind speeds of 0, 1, and 5 m/s.

CHAPTER 4

ASSESSMENT OF THE ANNUAL PERFORMANCE OF THE CYLINDRICAL FRESNEL LENS COLLECTOR

The annual performance of the collector is evaluated by selecting provinces with relatively higher direct normal irradiation values. The selected provinces whose long-term average of DNI's are given in Figure 4.1 [69], are Gaziantep, Aydın, Antalya, and Ankara.

The methodology for the model for this assessment contains Sun equations and TMY data for the aforementioned provinces in Turkey, and it is explained in Section 4.1. Additionally, a complementary MATLAB code, which gathers typical meteorological year data from OneBuilding's [70] repository, is written.

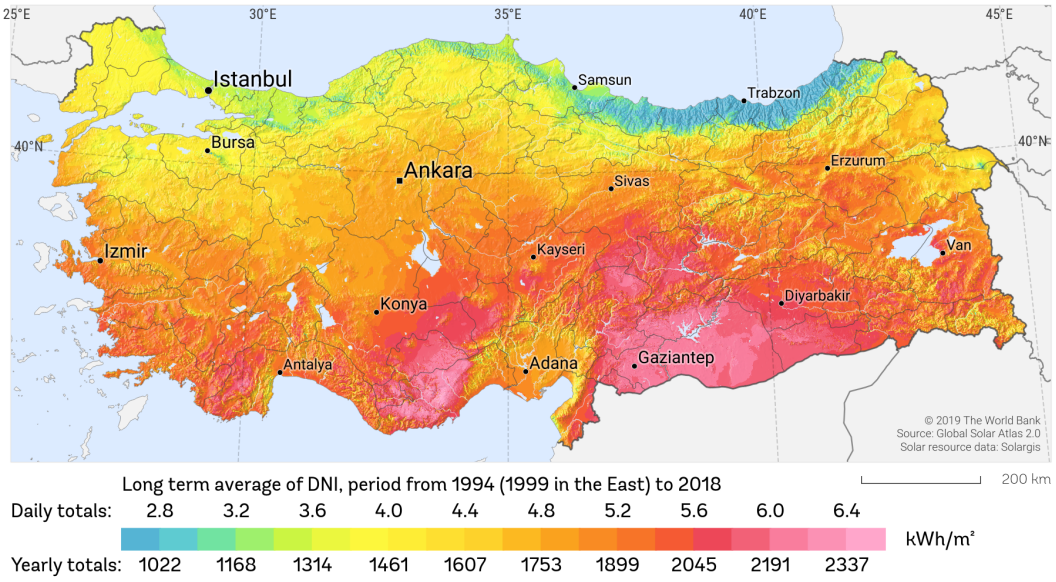

Figure 4.1: Long term average of direct normal irradiation map of Turkey, published by The World Bank [69].

4.1 Methodology

To calculate the optical efficiency, the Sun to receiver efficiency in this case, throughout the day, n, at a latitude of ϕ, and longitude of L_{loc}, the angle that the incoming beam radiation makes with the aperture of the collector should be obtained.

Using the following equations gathered from Duffie J. and Beckman W. [65], the position of the Sun is calculated.

The declination angle is calculated using Equation 4.1.

$$\delta = 23.45 \quad \sin\left(360\frac{284+n}{365}\frac{\pi}{180}\right)\frac{\pi}{180} \tag{4.1}$$

The equation of time, E, is calculated in terms of minutes using Equation 4.2,

$$\begin{aligned} E = 229.2(0.000075 + 0.001868\cos(B) - 0.032077\sin(B) \\ -0.014615\cos(2B) - 0.04089\sin(2B)) \end{aligned} \tag{4.2}$$

where B is found using Equation 4.3.

$$B = (n-1)\frac{360}{365}\frac{\pi}{180} \tag{4.3}$$

The middle of the hour in the solar time is calculated using Equation 4.4.

$$t_{solarmidhour} = t_{standard} + 4\left(L_{st} - L_{loc}\right) + \frac{E}{60} - 0.5\text{[hr]} \tag{4.4}$$

The local standard meridian is found by multiplying the difference between the local standard clock time and Greenwich Mean Time by 15.

$$\omega = 15\left(t_{solarmidhour} - t_{standard}\right)\frac{\pi}{180} \tag{4.5}$$

The solar zenith angle for horizontal surfaces is calculated using 4.6.

$$\cos\theta_z = \cos\phi\cos\delta\cos\omega + \sin\phi\sin\delta \tag{4.6}$$

And the solar azimuth for horizontal surfaces is calculated using 4.7.

$$\gamma_S = \text{sign}(\omega)\left|\cos^{-1}\left(\frac{\cos\theta_z\sin\phi - \sin\delta}{\sin\theta_z\cos\phi}\right)\right| \tag{4.7}$$

After calculating Sun's position, and its relative angles with a horizontal surface, the angle of incidence of the beam radiation on 1D tracking collectors can be calculated. For a collector that is N-S tracking by rotating around the E-W axis, the angle of incidence is calculated using Equation 4.8.

$$\cos\theta_s = \left(1 - \cos^2\delta \sin^2\omega\right)^{1/2} \tag{4.8}$$

The surface tilt angle is calculated using Equation 4.9.

$$\tan\beta_s = \tan\theta_z \left|\cos\gamma_s\right| \tag{4.9}$$

And the surface azimuth angle is calculated using Equation 4.10.

$$\gamma = \begin{cases} 0^\circ & \text{if } |\gamma_s| < 90 \\ 180^\circ & \text{if } |\gamma_s| \geq 90 \end{cases} \tag{4.10}$$

For a collector that is E-W tracking by rotating around the N-S axis, the angle of incidence is calculated using Equation 4.11. angle of incidence

$$\cos\theta_s = \left(\cos^2\theta_z + \cos^2\delta \sin^2\omega\right)^{1/2} \tag{4.11}$$

The surface tilt angle is calculated using Equation 4.12.

$$\tan\beta_s = \tan\theta_z \left|\cos\left(\gamma - \gamma_s\right)\right| \tag{4.12}$$

And the surface azimuth angle is calculated using Equation 4.13.

$$\gamma = \begin{cases} 90^\circ & \text{if } \gamma_s > 0 \\ -90^\circ & \text{if } \gamma_s \leq 0 \end{cases} \tag{4.13}$$

Using the angle of incidence on the collector for the middle of the hour in solar time and the obtained TMY data, the incidence angle modifier, the optical efficiency, which accounts for the losses except for the heat losses, and the absorbed solar radiation can be calculated using Equations 3.2, 4.14, and 4.15, respectively.

$$\eta_{opt}(\theta) = K(\theta) \;\; \eta_{opt,0} \tag{4.14}$$

$$q_{absorbed,rt} = \eta_{opt}(\theta) \;\; I_b \tag{4.15}$$

4.2 Annual Performance Results

To illustrate the results of the annual performance assessment, four provinces in Turkey have been selected. While the DNI for Gaziantep is the largest among the selected provinces, for Ankara, it is the smallest, most likely due to the weather conditions. In Figure 4.2, annual average hourly irradiation values are given. For this calculation, the incidence angle modifier obtained for the collector with a 4-meter length is used.

Considering the results given in Figure 4.2 and Table 4.1, which present the average daily total irradiation values, the E-W tracking collector has a higher daily average insolation than the N-S tracking one. As indicated by the last two columns of Table 4.1, similar annual average optical efficiencies for all providences due to similar latitudes.

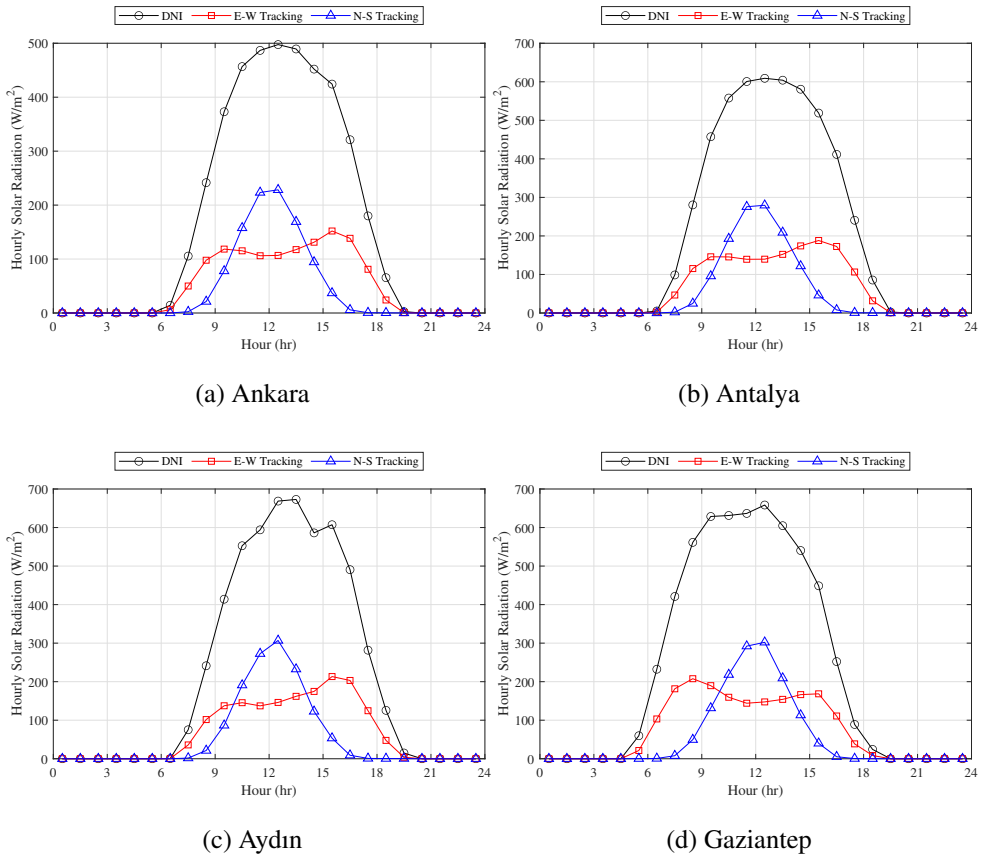

(a) Ankara (b) Antalya

(c) Aydın (d) Gaziantep

Figure 4.2: Annual average of hourly direct normal irradiation, and solar irradiation absorbed by the receiver for the E-W, and N-S tracking collectors.

Table 4.1: Annual average daily total direct normal irradiation, solar irradiation absorbed by the receiver, and annual optical efficiencies for the E-W, and N-S tracking collectors.

Providence	**DNI** (kWh/m^2)	$\mathbf{I_{EW}}$ (kWh/m^2)	$\mathbf{I_{NS}}$ (kWh/m^2)	$\overline{\eta_{optical,EW}}$ (%)	$\overline{\eta_{optical,NS}}$ (%)
Ankara	4.11	1.25	1.02	30.30	24.78
Antalya	5.05	1.56	1.26	30.88	24.88
Aydın	5.33	1.63	1.30	30.67	24.42
Gaziantep	5.79	1.80	1.37	31.12	23.69

In comparison to the other collector systems, the annual average optical efficiency of the Fresnel lens solar collector is lower considering the optical simulation study conducted by Kincaid et al. [71], which concludes that the annual optical efficiency for the selected parabolic trough collector is 60%, for the selected central receiver technology it is 52%, and for the selected linear Fresnel collector it is 40%, using China Lake, California as the location. Additionally, the average collection efficiency reported by Ma et al. [33], which is the most comparable efficiency in the literature to the presented optical efficiency in this study, is between 44% and 53% for days with DNI values averaging between 600 and 700 W/m^2.

In Table 4.2, seasonal daily average total DNI and solar irradiation absorbed by the receiver, and seasonal optical efficiencies are given. These results indicate that while the collectors with N-S tracking have similar optical efficiency throughout the year, the collectors with E-W tracking have varying optical efficiencies. Furthermore, in autumn and winter, days closer to the winter solstice, collectors with E-W tracking receive the rays at higher incidence angles, resulting in higher orientation losses and lower optical efficiencies. However, in spring and summer, days closer to the summer solstice, collectors with E-W tracking receive the rays at smaller incidence angles. The optical efficiencies of the collectors during summer are as high as around 40%. In comparison with the 0° angle of incidence, orientation losses account for 15-20% of the overall losses.

Table 4.2: Seasonal average daily total direct normal irradiation, solar irradiation absorbed by the receiver, and annual optical efficiencies for the E-W, and N-S tracking collectors.

Providence	**Season**	**DNI** (kWh/m^2)	$\mathbf{I_{EW}}$ (kWh/m^2)	$\mathbf{I_{NS}}$ (kWh/m^2)	$\overline{\eta_{optical,EW}}$ (%)	$\overline{\eta_{optical,NS}}$ (%)
Ankara	Winter	2.16	0.23	0.63	10.62	29.16
	Spring	3.86	1.33	0.90	34.49	23.30
	Summer	6.27	2.56	1.44	40.76	22.98
	Autumn	4.11	0.84	1.10	20.42	26.69
Antalya	Winter	3.46	0.39	1.01	11.32	29.09
	Spring	5.02	1.82	1.16	36.32	23.11
	Summer	7.05	2.98	1.64	42.26	23.20
	Autumn	4.65	1.02	1.22	21.85	26.29
Aydın	Winter	3.34	0.39	0.94	11.83	28.04
	Spring	5.57	1.99	1.29	35.68	23.11
	Summer	7.31	3.04	1.66	41.64	22.68
	Autumn	5.03	1.07	1.31	21.30	26.04
Gaziantep	Winter	3.62	0.40	1.06	10.92	29.21
	Spring	5.77	2.11	1.25	36.59	21.65
	Summer	8.10	3.44	1.75	42.51	21.63
	Autumn	5.61	1.22	1.42	21.70	25.29

In the winter, the solar energy resources of the provinces in Turkey are lower than in other seasons. This is because Turkey is located in the northern hemisphere, and the sun is lower in the sky in the winter. Moreover, the optical efficiency, or the amount of light that is collected, is affected by the angle of the sun's rays due to the fact that the sun's rays hit the earth at different angles throughout the year. The optical efficiency of a collector with E-W tracking decreases from 40% in summer to 10% in winter, while the optical efficiency of a collector with N-S tracking decreases from 29% in summer to 21% in winter, which is lower than the E-W tracking collector, but it is in a narrower band. Withal, as expected, lower optical efficiency due to latitude was obtained for Ankara compared to other provinces, and the low DNI values compared to other provinces abbreviate the heat collected with low optical efficiency. For further examining the results, two days with relaitively clear skies close to the solstices have been selected and the results obtained from the annual model on those days are presented in Figure 4.3

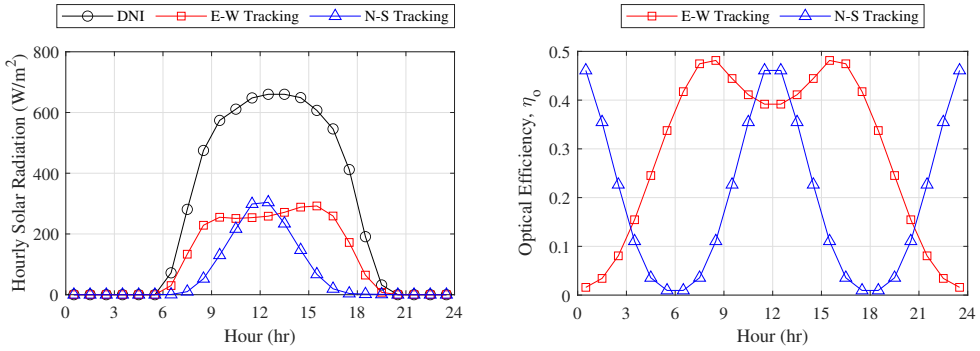

(a) Ankara, June 24th

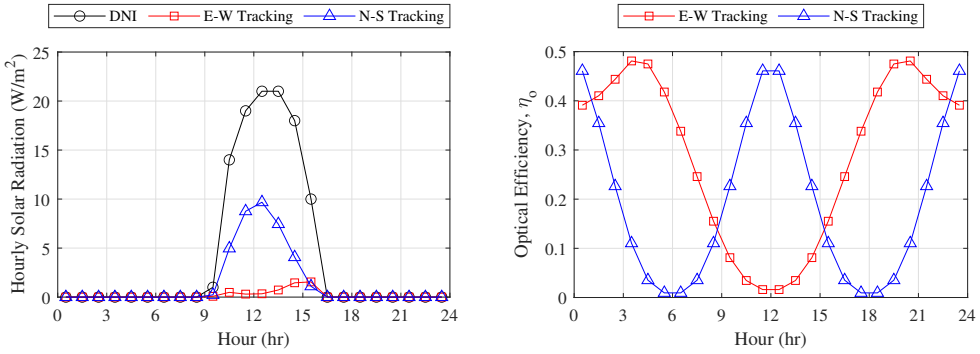

(b) Ankara, December 26th

Figure 4.3: Sample results for the annual model for Ankara at two relatively clear days, close to solstices.

As illustrated in Figure 4.3, the DNI values on December 26th, which is close to the winter solstice, is significantly lower compared to the DNI values on June 24th, which is close to the summer solstice. Furthermore, the optical efficiency of the E-W tracking collector varies depending on the season and time of day, which is, in summer, the efficiency is highest in the hour closer to the middle of the day, while in winter the efficiency is lowest in the middle of the day. Besides, the N-S tracking collector is less affected by the seasonality of the incidence angles of the sun's rays and draws a similar profile throughout the year.

If examined, the peak of the heat collection value of the EW tracking collector is not in the middle of the day. It is belived to originate from the fact that the collected heat is a product obtained by multiplying the DNI value with the optical efficiency. The N-S tracking collector, which is used to collect heat from the sun, reaches its heat collection peak at the middle of the day. This is as expected, since the sun is at its highest point in the sky during this time.

4.3 Working Temperature Range of the Fresnel Lens Solar Collector

The thermal and annual models have been coupled to determine the outlet temperatures throughout the day. To do this, a simple search algorithm based on bisection method, which uses Equations 4.16, 4.17, and 4.18, is utilized.

The Equation 4.16, which calls the thermal model, allows for the determination of the convective heat transfer to the working fluid, given the absorbed energy, the mean fluid temperature, the ambient air temperature, and the flow rate of the working fluid.

$$q_{conv,f-rt_i} = f_{thermalmodel}(q_{rad_{rt}}, q_{rad_{ge}}, L, T_a, T_f, \dot{m}_{oil}, V_{wind}) \tag{4.16}$$

Using Equation 4.17, the temperature range of the oil for the step is calculated.

$$\Delta T = T_{outlet} - T_{inlet} = \frac{q_{conv,f-rt_i}}{\dot{m}_{oil}\ C_{p_{oil}}(T_f)} \tag{4.17}$$

And using the search algorithm on Equation 4.18, mean fluid temperature for the step is obtained. This search algorithm is illustrated in Figure 4.4.

$$f_{objective} = T_f - \frac{\Delta T}{2} - T_{inlet} \tag{4.18}$$

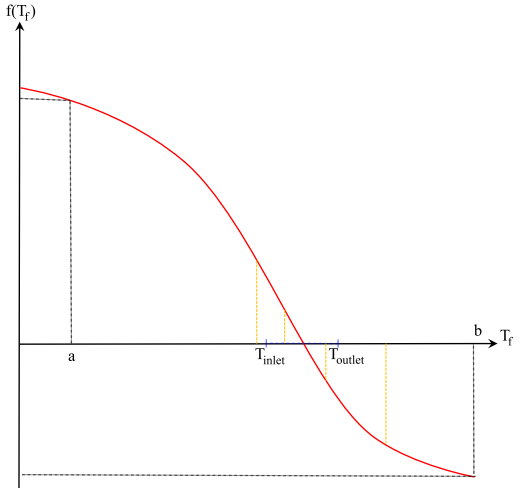

Figure 4.4: Illustration of root-finding method for determining the bulk fluid temperature for a step.

Utilizing this search algoritm with the absorbed energy data obtained from the annual model for Ankara on June 24th, a sunny day close to the summer solstice, the results given in Figure 4.5 are obtained. In these simulations, collector lengths, L, are 4 and 8 meters, which refers to two 4 meters array, the ambient temperature is 25 °C, the working fluids flow rate is 55 liters per minute, wind speed and $q_{rad_{ge}}$ are zero. Addionally, the bounding temperatures for the bisection search algorithm are the ambient temperature as the lower bound and 400 °C as the upper bound. Besides, there is another parameter seperate from the previous models, hourly loop count, which indicates the oil tank volume proportional to the flow rate. In these simulations, the preferred hourly loop count is 10 and 5 correspond to 330 and 660 liters tank volume, respectively.

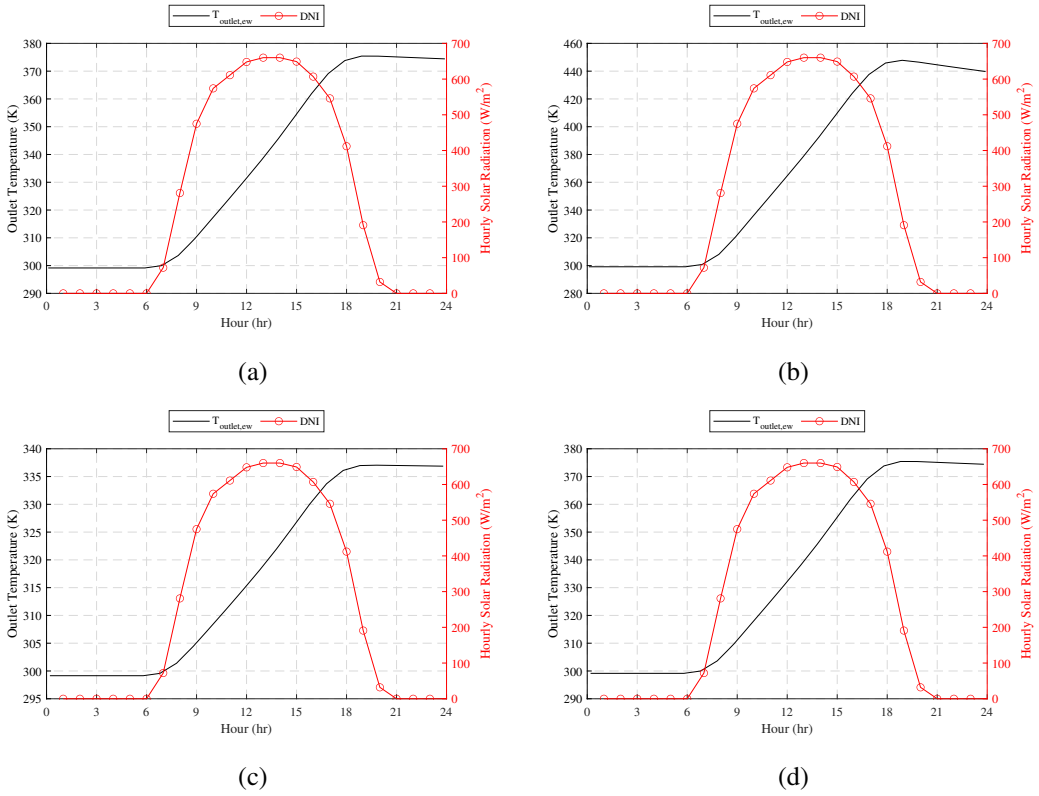

Figure 4.5: Sample outlet temperature calculation results for the coupled thermal and annual models for Ankara on June 24th, close to summer solstice. *(a) 4-meters long collector array, 330-liters tank volume, (b) 8-meters long collector array 330-liters tank volume, (c) 4-meters long collector array, 660-liters tank volume, (d) 8-meters long collector array 660-liters tank volume.*

The outlet temperatures of the working fluid gradually increase from sunrise to sunset and then starts decreasing after sunset. This means that the inlet temperature of the working fluid is constant during a loop, and the effects of thermal stratification are not considered. In Figure 4.5, the first two graphs are for 4 and 8 meters long collector arrays, in which the working fluid loops the field ten times per hour, and the collectors reach temperatures around 100 °C and 180 °C respectively. The latter two graphs are for 4 and 8 meters long collector arrays, in which the working fluid loops the field five times per hour, and with this difference the assumed tank volume would be doubled, and the collectors reach temperatures around 65 °C and 100 °C respectively. The absorbed and the collected heat during the day for these cases are given in Table 4.3.

$$Q_{collected} = \sum_{t=1}^{24N_{loop}} m_{oil}\, C_{p_{oil}} \left(\frac{T_{outlet}(t) - T_{inlet}(t)}{2} \right) \left(T_{outlet}(t) - T_{inlet}(t) \right) \quad (4.19)$$

Table 4.3: The absorbed and the collected energies for the sample results for Ankara on June 24th.

		Case 1	**Case 2**	**Case 3**	**Case 4**
$Q_{collected}$	*(MJ)*	37.45	69.84	37.51	74.90
$Q_{absorbed}$	*(MJ)*	39.83	79.66	39.83	79.66

The results of the study suggest that the heat loss predicted by the model is not enough. The ideal temperature profile would be a wide bell-curve, whose center is shifted to afternoon, however, the results show a steady increase from sunrise to sunset and a slight decrease after sunset. This result is expected because the model only focuses on the receiver, and not on the rest of the system. This means that there would be no heat losses from the working fluid to the environment, and additionally, no thermal load added to the system.

The results from the coupled model suggest that the scaled Fresnel lens solar collector system would be able to handle the thermal load of a low-medium temperature SHIP application. A more comprehensive system model should be constructed and further analysis should be made in order to improve the understanding of the system.

CHAPTER 5

CONCLUSIONS

5.1 Conclusions

The cylindrical Fresnel lens solar collector studied in this thesis is a promising technology for solar energy applications. The iterative testing algorithm proposed for designing the lens is effective, and the open-source ray-tracing code developed for examining the performance of the collector is accurate. The thermal model constructed for finding the heat loss under different conditions is reliable but underestimates the heat loss from the collector system since it focuses on the receiver. The annual model constructed using actual TMY data for Turkey gives realistic results for the year-long analysis.

Under zero incidence angle conditions, the optical efficiency of the collector system is obtained as 49.57%, and an incidence angle modifier equation for optical efficiency for non-zero incidence angles is proposed. The local concentration ratio is drawn for zero-degree incidence angle in Figure 3.14, and a geometric concentration ratio of 14.43 is obtained for the lens. The seasonality of the optical efficiency, according to the annual performance model results, shows that a collector with E-W tracking has an optical efficiency of about 40% in summer and 10% in winter, while an N-S tracking collector has an optical efficiency of about 29% in summer and 21% in winter. Comparatively to other collector systems, the average annual optical efficiency of the Fresnel lens solar collector is inferior to that of the optical simulation study conducted by Kincaid et al. [71], which finds that the annual optical efficiencies are 60% for the parabolic trough collector, 52% for the central receiver technology, and 40% for the linear Fresnel collector. In the literature, the average collection efficiency

provided by Ma et al. [33], which is one of the most comparable efficiency to the optical efficiency presented in this study, is in the range of 44% to 53% for days with average DNI values ranging from 600 to 700 W/m^2 . It is suggested that to improve the annual collector performance, and the collector should be placed at an angle to reduce the orientation loss due to the incidence angle throughout the year.

The combined model combines the thermal model on the receiver with the annual performance model and provides operating temperatures for different oil tank volumes and collector array lengths for a given loop. For example, an 8-meter-long collector array with a tank volume of 330 liters reached operating temperatures around 180 °C in Ankara on June 24. It is noted that the thermal model underestimates the collector system's heat loss as it emphasizes the heat loss from the receiver. Further analysis is required to integrate the additional heat losses occurring in different components of the system.

The average resin price for polycarbonate at the time is 1.28 €/kg [72], which corresponds to a material cost of 6.84 €/m^2 aperture area. Xiao et al. [73] specify a cost for a cylindrical Fresnel lens solar concentrator as around 600 Chinese Yen, equivalent to \$87.5 with 10 years of a lifetime for a Fresnel lens with a 1.3 m^2 aperture area. The assessment of Ma et al. [34] with a wider perspective, projects a cost of 260\$/m^2 for the whole collector system. In comparison to the parabolic trough collector cost analysis given in Table 1.1, with the assumption of reducing costs by using stable receiver tubes, and constructing a simpler structure due to light-weight, there seems to be a potential, however, the decrease in the aperture area increases the receiver cost up to 110 \$/m^2 [74], and the initial cost assumption to 200\$/m^2 for this collector system. For that reason, ways to increase the aperture area and alternative receiver systems should be investigated. Nevertheless, the Fresnel lens solar collector system could be scaled to be used to supply the heat demand corresponding to low-temperature and medium-temperature heat processes, especially for small installation areas.

5.2 Future Work

The future work of this thesis can be separated into three parts, the open-source ray-tracing code, the system model, and the experimental study.

The open-source ray-tracing code could be improved by,

- speeding up the code by adding a shape library,
- speeding up the code by utilizing high-performance GPU programming that Julia offers,
- adding a user interface with calls to Julia, and
- embedding GMSH into the code, and using pycall to bring Paraview for visuals.

A system model that includes other components of the collector system should be constructed.

The experimental study planned after this study includes a roof-top experimental setup illustrated in Figure 5.1.

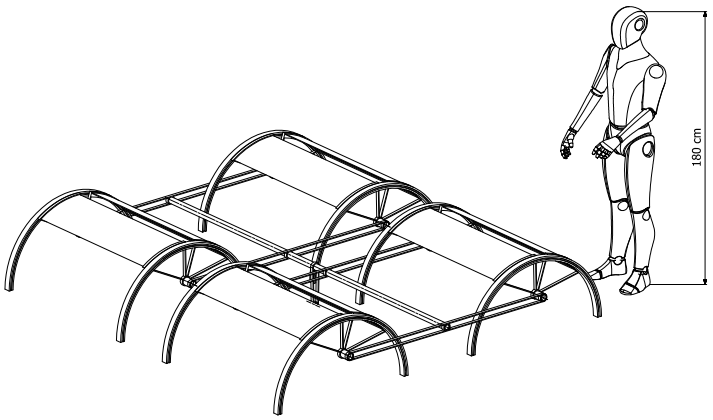

Figure 5.1: Schematic of the experimental setup for future work.

REFERENCES

[1] A. Alarcón Villamil, J. E. Hortúa, and A. López, "Comparison of thermal solar collector technologies and their applications," *TECCIENCIA*, vol. 8, no. 15, p. 26–35, Dec. 2013. [Online]. Available: https://revistas.ecci.edu.co/index.php/TECCIENCIA/article/view/91

[2] "Paris agreement." [Online]. Available: https://ec.europa.eu/clima/eu-action/international-action-climate-change-climate-negotiations/paris-agreement_en

[3] "The Paris Agreement." [Online]. Available: https://www.un.org/en/climatechange/paris-agreement

[4] "How do photovoltaics work?" [Online]. Available: https://science.nasa.gov/science-news/science-at-nasa/2002/solarcells#:~:text=Photovoltaics%20is%20the%20direct%20conversion,of%20light%20and%20release%20electrons.

[5] C. Kost, S. Shammugam, V. Fluri, D. Peper, A. D. Memar, and T. Schlegl, "Levelized Cost of Electricity- Renewable Energy Technologies - June 2021." [Online]. Available: https://www.ise.fraunhofer.de/content/dam/ise/en/documents/publications/studies/EN2021_Fraunhofer-ISE_LCOE_Renewable_Energy_Technologies.pdf

[6] A. Gurung and Q. Qiao, "Solar charging batteries: Advances, challenges, and opportunities," *Joule*, vol. 2, no. 7, pp. 1217–1230, 2018. [Online]. Available: https://www.sciencedirect.com/science/article/pii/S2542435118301430

[7] IEA, "Renewables 2021 – analysis," Dec 2021. [Online]. Available: https://www.iea.org/reports/renewables-2021

[8] "Repowereu: Affordable, secure and sustainable energy for europe," Jul 2022. [Online]. Avail-

able: https://ec.europa.eu/info/strategy/priorities-2019-2024/european-green-deal/repowereu-affordable-secure-and-sustainable-energy-europe_en

[9] "Solar heat for industry, april 2017," Jul 2020. [Online]. Available: https://www.solar-payback.com/download/solar-heat-for-industry-april-2017/

[10] IEA, "Share of solar thermal heat consumption in total final energy consumption, in selected countries and regions, 2019 – Data & Statistics." [Online]. Available: https://www.iea.org/data-and-statistics/charts/share-of-solar-thermal-heat-consumption-in-total-final-energy-consumption-in-selected-countries-and-regions-2019

[11] ——, "Renewables 2020 – analysis," Nov 2020. [Online]. Available: https://www.iea.org/reports/renewables-2020

[12] C. Difiglio, B. Güray, E. Merdan, and D. Esmaeili Aliabadi, *TURKEY ENERGY OUTLOOK 2020*, 11 2020.

[13] IEA, "Share of renewable sources in global heat consumption, 2019 – Data & Statistics." [Online]. Available: https://www.iea.org/data-and-statistics/charts/share-of-renewable-sources-in-global-heat-consumption-2019

[14] E. Zarza, "ODAK$_{TR}$ Seminar Series - An Introduction to Concentrating Solar Thermal (CST) Technologies and Applications," 2019. [Online]. Available: https://www.dropbox.com/s/scq1e179r00xyel/Introduction%20to%20CST%20Systems_E%20Zarza.pdf?dl=0

[15] "SET Plan Information System." [Online]. Available: https://setis.ec.europa.eu/index_en

[16] "Renewable power generation costs in 2020." [Online]. Available: https://www.irena.org/-/media/Files/IRENA/Agency/Publication/2021/Jun/IRENA_Power_Generation_Costs_2020_Highlights.pdf?la=en&hash=BB5229A4CD1C39EEFAEF958AF53534DC605E0CCA

[17] P. Kurup and C. S. Turchi, "Parabolic trough collector cost update for the system advisor model (sam) - nrel." [Online]. Available: https://www.nrel.gov/docs/fy16osti/65228.pdf

[18] J. A. Duffie and W. A. Beckman, *Concentrating Collectors*. John Wiley & Sons, Ltd, 2013, ch. 7, pp. 322–372. [Online]. Available: https://onlinelibrary.wiley.com/doi/abs/10.1002/9781118671603.ch7

[19] S. A. Kalogirou, "Chapter three - solar energy collectors," in *Solar Energy Engineering*, S. A. Kalogirou, Ed. Boston: Academic Press, 2009, pp. 121–217. [Online]. Available: https://www.sciencedirect.com/science/article/pii/B9780123745019000030

[20] A. Luzzi and K. Lovegrove, "Solar thermal power generation," in *Encyclopedia of Energy*, C. J. Cleveland, Ed. New York: Elsevier, 2004, pp. 669–683. [Online]. Available: https://www.sciencedirect.com/science/article/pii/B012176480X005313

[21] Worland, Justin and Raab, Josh, "This solar power plant can run all night," 2016, [Online; accessed July 31, 2022]. [Online]. Available: https://time.com/4291347/crescent-dunes-solar-power-plant/

[22] "Maricopa solar power dish plant." [Online]. Available: https://www.energy.gov/eere/solar/articles/maricopa-solar-power-dish-plant

[23] P. Breeze, "Chapter 13 - solar power," in *Power Generation Technologies (Second Edition)*, second edition ed., P. Breeze, Ed. Boston: Newnes, 2014, pp. 259–286. [Online]. Available: https://www.sciencedirect.com/science/article/pii/B9780080983301000132

[24] S. Dieckmann, J. Dersch, S. Giuliano, M. Puppe, E. Lüpfert, K. Hennecke, R. Pitz-Paal, M. Taylor, and P. Ralon, "Lcoe reduction potential of parabolic trough and solar tower csp technology until 2025," *AIP Conference Proceedings*, vol. 1850, no. 1, p. 160004, 2017. [Online]. Available: https://aip.scitation.org/doi/abs/10.1063/1.4984538

[25] "Morocco - The Ouarzazate Solar Power Station Project – Phase I." [Online]. Available: https://projectsportal.afdb.org/dataportal/VProject/show/P-MA-FF0-001

[26] "World's Largest Linear Fresnel Solar Power Station Commences Operation."

[Online]. Available: https://www.evwind.es/2012/10/07/worlds-largest-linear-fresnel-solar-power-station-commences-operation/24364

[27] X. Ma, H. Zheng, and Z. Chen, "An investigation on a compound cylindrical solar concentrator (ccsc)," *Applied Thermal Engineering*, vol. 120, pp. 719–727, 2017. [Online]. Available: https://www.sciencedirect.com/science/article/pii/S1359431117323499

[28] G. Wu, H. Zheng, X. Ma, C. Kutlu, and Y. Su, "Experimental investigation of a multi-stage humidification-dehumidification desalination system heated directly by a cylindrical fresnel lens solar concentrator," *Energy Conversion and Management*, vol. 143, pp. 241–251, 2017. [Online]. Available: https://www.sciencedirect.com/science/article/pii/S0196890417303151

[29] W. Xie, Y. Dai, and R. Wang, "Thermal performance analysis of a line-focus fresnel lens solar collector using different cavity receivers," *Solar Energy*, vol. 91, pp. 242–255, 2013. [Online]. Available: https://www.sciencedirect.com/science/article/pii/S0038092X13000571

[30] ——, "Numerical and experimental analysis of a point focus solar collector using high concentration imaging pmma fresnel lens," *Energy Conversion and Management*, vol. 52, no. 6, pp. 2417–2426, 2011, 9th International Conference on Sustainable Energy Technologies (SET 2010). [Online]. Available: https://www.sciencedirect.com/science/article/pii/S0196890411000513

[31] S. Sripadmanabhan Indira, C. A. Vaithilingam, K.-K. Chong, R. Saidur, M. Faizal, S. Abubakar, and S. Paiman, "A review on various configurations of hybrid concentrator photovoltaic and thermoelectric generator system," *Solar Energy*, vol. 201, pp. 122–148, 2020. [Online]. Available: https://www.sciencedirect.com/science/article/pii/S0038092X20302176

[32] W. Xie, Y. Dai, R. Wang, and K. Sumathy, "Concentrated solar energy applications using fresnel lenses: A review," *Renewable and Sustainable Energy Reviews*, vol. 15, no. 6, pp. 2588–2606, 2011. [Online]. Available: https://www.sciencedirect.com/science/article/pii/S1364032111001341

[33] X. Ma, R. Jin, S. Liang, S. Liu, and H. Zheng, "Analysis on an optimal

transmittance of fresnel lens as solar concentrator," *Solar Energy*, vol. 207, pp. 22–31, 2020. [Online]. Available: https://www.sciencedirect.com/science/article/pii/S0038092X2030685X

[34] X. Ma, H. Zheng, and S. Liu, "Optimization on a cylindrical fresnel lens and its validation in a medium-temperature solar steam generation system," *Renewable Energy*, vol. 134, pp. 1332–1343, 2019. [Online]. Available: https://www.sciencedirect.com/science/article/pii/S0960148118310255

[35] X. Ma, R. Jin, S. Liang, and H. Zheng, "Ideal shape of fresnel lens for visible solar light concentration," *Opt. Express*, vol. 28, no. 12, pp. 18 141–18 149, Jun 2020. [Online]. Available: http://opg.optica.org/oe/abstract.cfm?URI=oe-28-12-18141

[36] "Solar Industrial Process Heat - State of the Art - ESTIF." [Online]. Available: http://www.estif.org/fileadmin/estif/content/policies/downloads/D23-solar-industrial-process-heat.pdf

[37] "Cost trends of solar energy for heat in industry." [Online]. Available: https://www.solrico.com/fileadmin/solrico/media/doc/Solar_payback/Flyer_SHIP_Cost_Trends_August_2021.pdf

[38] "Reference Air Mass 1.5 Spectra." [Online]. Available: https://www.nrel.gov/grid/solar-resource/spectra-am1.5.html

[39] M. F. Modest, "Chapter 1 - Fundamentals of Thermal Radiation," Boston, pp. 1–30, 2013. [Online]. Available: https://www.sciencedirect.com/science/article/pii/B9780123869449500017

[40] ——, "Chapter 2 - Radiative Property Predictions From Electromagnetic Wave Theory," pp. 31–60, 2013. [Online]. Available: https://www.sciencedirect.com/science/article/pii/B9780123869449500029

[41] X. Zhang, J. Qiu, X. Li, J. Zhao, and L. Liu, "Complex refractive indices measurements of polymers in visible and near-infrared bands," *Appl. Opt.*, vol. 59, no. 8, pp. 2337–2344, Mar 2020. [Online]. Available: http://opg.optica.org/ao/abstract.cfm?URI=ao-59-8-2337

[42] X. Zhang, J. Qiu, J. Zhao, X. Li, and L. Liu, "Complex refractive indices measurements of polymers in infrared bands," *Journal of Quantitative Spectroscopy and Radiative Transfer*, vol. 252, p. 107063, 2020. [Online]. Available: https://www.sciencedirect.com/science/article/pii/S0022407320301394

[43] M. F. Modest, *Radiative Heat Transfer*, 3rd ed., M. F. Modest, Ed. Elsevier, 2013.

[44] M. Rubin, "Optical properties of soda lime silica glasses," *Solar Energy Materials*, vol. 12, no. 4, pp. 275–288, 1985. [Online]. Available: https://www.sciencedirect.com/science/article/pii/0165163385900528

[45] J. M. Snyder and A. H. Barr, "Ray tracing complex models containing surface tessellations," *SIGGRAPH Comput. Graph.*, vol. 21, no. 4, pp. 119–128, aug 1987. [Online]. Available: https://doi.org/10.1145/37402.37417

[46] D. Badouel, "An efficient ray — polygon intersection," in *Graphics Gems*, A. S. GLASSNER, Ed. San Diego: Morgan Kaufmann, 1990, pp. 390–393. [Online]. Available: https://www.sciencedirect.com/science/article/pii/B9780080507538500826

[47] T. Möller and B. Trumbore, "Fast, minimum storage ray-triangle intersection," *Journal of Graphics Tools*, vol. 2, no. 1, pp. 21–28, 1997. [Online]. Available: https://doi.org/10.1080/10867651.1997.10487468

[48] T. Akenine-Möller, E. Haines, N. Hoffman, A. Pesce, M. Iwanicki, and S. Hillaire, *Real-Time Rendering*, 4th ed. A K Peters/CRC Press, 8 2018, 22.9 Ray/Polygon Intersection (966-967).

[49] P. J. Schneider and D. H. Eberly, "Chapter 13 - computational geometry topics," pp. 673–825, 2003. [Online]. Available: https://www.sciencedirect.com/science/article/pii/B9781558605947500163

[50] J. O'Rourke, *Computational Geometry in C*, 2nd ed. Cambridge University Press, 10 1998.

[51] "Julia 1.7 documentation." [Online]. Available: https://docs.julialang.org/en/v1/

[52] "Gmsh - a three-dimensional finite element mesh generator with built-in pre- and post-processing facilities." [Online]. Available: https://gmsh.info/

[53] H. Zheng, C. Feng, Y. Su, J. Dai, and X. Ma, "Design and experimental analysis of a cylindrical compound fresnel solar concentrator," *Solar Energy*, vol. 107, pp. 26–37, 2014. [Online]. Available: https://www.sciencedirect.com/science/article/pii/S0038092X14002382

[54] E. Hecht, *Optics*. Pearson Education, 2017.

[55] J. Hepp, "Development of visualization and quantification techniques of local material failures in pv," Ph.D. dissertation, 01 2020.

[56] S. A. Kalogirou, "A detailed thermal model of a parabolic trough collector receiver," *Energy*, vol. 48, no. 1, pp. 298–306, Dec. 2012. [Online]. Available: https://doi.org/10.1016/j.energy.2012.06.023

[57] R. K. Shah and D. P. Sekulić, *Surface Basic Heat Transfer and Flow Friction Characteristics*. John Wiley & Sons, Ltd, 2003, ch. 7, pp. 425–562. [Online]. Available: https://onlinelibrary.wiley.com/doi/abs/10.1002/9780470172605.ch7

[58] "Syltherm™ 800 stabilized heat transfer fluid." [Online]. Available: https://www.dow.com/en-us/pdp.syltherm-800-stabilized-heat-transfer-fluid.39260z.html#overview

[59] Çengel Yunus A. and A. A. Ghajar, *Heat and mass transfer: A practical approach*. McGraw-Hill, 2010.

[60] "Borosilicate glass material properties," Jun 2020. [Online]. Available: https://www.imetra.com/borosilicate-glass-material-properties/

[61] F. P. Incropera, *Fundamentals of Heat and Mass Transfer*. Wiley, 2007.

[62] A. M. de Oliveira Siqueira, P. E. N. Gomes, L. Torrezani, E. O. Lucas, and G. M. da Cruz Pereira, "Heat transfer analysis and modeling of a parabolic trough solar collector: An analysis," *Energy Procedia*, vol. 57, pp. 401–410, 2014, 2013 ISES Solar World Congress. [Online]. Available: https://www.sciencedirect.com/science/article/pii/S1876610214015604

[63] “Opticstudio.” [Online]. Available: https://www.zemax.com/pages/opticstudio

[64] V. E. Dudley, G. J. Kolb, A. R. Mahoney, T. R. Mancini, C. W. Matthews, M. Sloan, and D. Kearney, “Test results: Segs ls-2 solar collector.” [Online]. Available: https://www.osti.gov/biblio/70756

[65] J. A. Duffie and W. A. Beckman, *Solar Engineering of Thermal Processes*. John Wiley & Sons Ltd, 2013.

[66] M. Lin, K. Sumathy, Y. Dai, and X. Zhao, “Performance investigation on a linear fresnel lens solar collector using cavity receiver,” *Solar Energy*, vol. 107, pp. 50–62, 2014. [Online]. Available: https://www.sciencedirect.com/science/article/pii/S0038092X14002552

[67] F. Sallaberry, Z. Tian, O. G. Jauregi, S. Furbo, B. Perers, A. Zourellis, and J. H. Rothmann, “Evaluation of the tracking accuracy of parabolic-trough collectors in a solar plant for district heating,” *AIP Conference Proceedings*, vol. 2033, no. 1, p. 030015, 2018. [Online]. Available: https://aip.scitation.org/doi/abs/10.1063/1.5067031

[68] F. Sallaberry, R. Pujol-Nadal, M. Larcher, and M. H. Rittmann-Frank, “Direct tracking error characterization on a single-axis solar tracker,” *Energy Conversion and Management*, vol. 105, pp. 1281–1290, 2015. [Online]. Available: https://www.sciencedirect.com/science/article/pii/S0196890415008353

[69] Solargis. [Online]. Available: https://globalsolaratlas.info/download/turkey

[70] “Repository of free climate data for building performance simulation.” [Online]. Available: https://climate.onebuilding.org/

[71] N. Kincaid, G. Mungas, N. Kramer, M. Wagner, and G. Zhu, “An optical performance comparison of three concentrating solar power collector designs in linear fresnel, parabolic trough, and central receiver,” *Applied Energy*, vol. 231, pp. 1109–1121, 2018. [Online]. Available: https://www.sciencedirect.com/science/article/pii/S0306261918314648

[72] K. New Media Publisher GmbH, “Real time price list.” [Online]. Available: https://plasticker.de/preise/pms_en.php?kat=Mahlgut&aog=A&show=ok&make=ok

[73] J. Xiao, H. Zheng, R. Jin, S. Liang, G. Wang, and X. Ma, "Experimental investigation of a bubbling humidification-dehumidification desalination system directly heated by cylindrical fresnel lens solar concentrator," *Solar Energy*, vol. 220, pp. 873–881, 2021. [Online]. Available: https://www.sciencedirect.com/science/article/pii/S0038092X21002875

[74] "Both sides open vacuum tube parabolic solar receiver tube." [Online]. Available: https://www.alibaba.com/product-detail/Both-sides-open-vacuum-tube-parabolic_60428158073.html